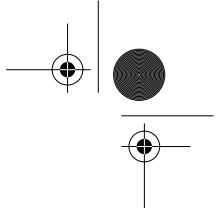


REMOTE SENSING SERIES **36**

PETER A. KELLER

# Imaging Spectroscopy of Lake Water Quality Parameters



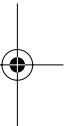
Editorial Board of the Remote Sensing Series:  
Prof. Dr. K. I. Itten, Prof. Dr. D. Nüesch, Dr. U. Frei, Dr. T. W. Kellenberger,  
Dr. E. Meier, and Dr. M. Schaepman.

*Die vorliegende Arbeit wurde von der Mathematisch-naturwissenschaftlichen Fakultät der Universität Zürich im Wintersemester 2000/2001 aufgrund der Gutachten von Prof. Dr. K. I. Itten und Dr. A. Wüest, EAWAG Dübendorf (CH), als Dissertation angenommen.*



Remote Sensing Laboratories  
Department of Geography  
University of Zürich  
Winterthurerstrasse 190  
CH-8057 Zürich  
Switzerland

<http://www.geo.unizh.ch>

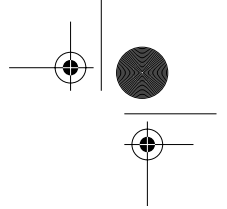


Copyright © 2001 Peter A. Keller, University of Zürich, Switzerland

Printed by the *Druckerei der Zentralstelle der Studentenschaft der Universität Zürich*

ISBN 3-03703-002-X





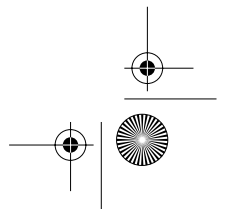
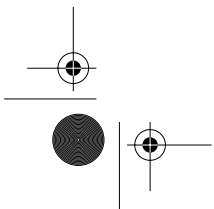
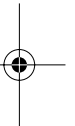
## Acknowledgements

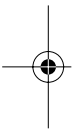
This study was carried out under the Swiss National Science Foundation projects No. 21-40539.94 and No. 20-50727.97.

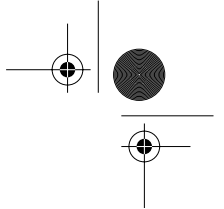
Due to its interdisciplinarity, the work would not have been possible with support of many different persons I would like to thank for their generous help:

My “Doktorvater” Klaus Itten for giving a limnologist the opportunity to write a thesis in his group. The Co-Investigator Johnny Wüest of the EAWAG for the proof-reading, his interest and his feedback on my work. Of course all my colleagues at RSL for answering my questions, helping me organizing campaigns, giving feedback to my work, as well as getting on with me: Anko “Hossa” Börner (now at DLR Berlin), Nina Dickerhof, Sandra Eckert, Hans Gunnervall, Tobias Kellenberger, Mathias Kneubühler, Ivo Leiss (now with Ernst Basler & Partners), Michael Schaepman, Daniel Schläpfer, Gabi Strub, and especially Stephan Bojinski for his tremendous assistance in the proof-reading of this study. Caroline Stengel, Mike Schurter, Silke Meyns and her team, and Daniel Kobler of the EAWAG helping me with the laboratory and field measurements. René Beck of the laboratory of Kanton Zug for his assistance at my various field campaigns at Lake Zug. Ferdinand Schanz of the Limnological Station of the University of Zürich for helping me out with the algae determinations (although these results have not been included into the work) and providing me with illustrations of the algae. Stefan Dunst, Ueli Bosshart, and the rest of the team of the Wasserversorgung Zürich for allowing me to board for measuring and for providing me with all their *in situ* measurements. Peter Gege and his colleagues of the ROSIS group at DLR Oberpfaffenhofen for giving me important inputs and for allowing me to join them on Lake Constance. Rolf Richter of DLR Oberpfaffenhofen for providing me with the ATCOR model and for helping me generously with my atmospheric correction problems. Arnold Dekker (now with CSIRO, Australia) and Hans van der Woerd of the Free University of Amsterdam for allowing me to join the project POWERS during one year which gave me important inputs for my work. Ivo Keller and Jürgen Fischer of the Institute for Space Science at the Free University of Berlin for providing me with the CASI data. Don Pierson and his colleagues at Uppsala University for the realisation of the underwater box. As well as all others colleagues and friends who helped and inspired me but I have not mentioned here.

And finally my wife Isabel and my sons Severin and Manuel for their love.







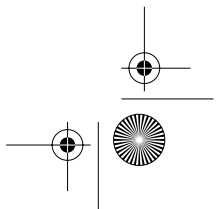
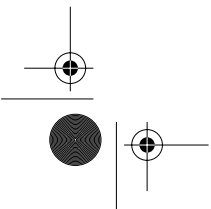
## Summary

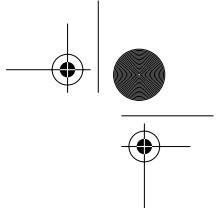
Several scientific programs serve for the monitoring of water quality. Traditionally, water samples are taken and analysed in the laboratory which is time and money consuming. The goal of this study is to show the potential of remote sensing techniques for such investigations. Three main problem areas were investigated in detail: (1) correction for atmosphere effects, (2) correction for air-water interface effects, and (3) inversion of the sub-surface radiation for the determination of the quality parameters such as chlorophyll *a* or suspended matter. The implemented methods were tested on a data set taken with the CASI imaging spectrometer over Lake Zug (Switzerland).

(1) As the atmospheric influence is often quantitatively more important than the water-leaving radiance, it is essential that the atmospheric correction is done with great care. In this study, an algorithm was developed based on the radiative transfer code MODTRAN/ATCOR. Under the assumption that the radiance leaving the water is zero in the near infrared, it was possible to derive the meteorological range which determines the aerosol concentration in the atmospheric radiative transfer model enabling a pixelwise atmospheric correction.

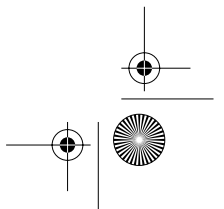
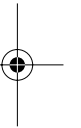
(2) The knowledge of the processes at the air-water interface allows the calculation of the sub-surface reflectance based on the atmospheric corrected data. The description of these processes was possible with transfer equations for downwelling irradiance and upwelling radiance which were confirmed by radiometric measurements in Walensee and Lake Zürich.

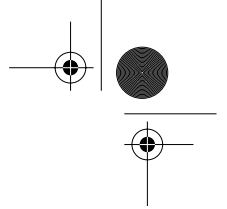
(3) The sub-surface reflectance is the basis for the actual determination of the water quality parameters. In this study, matrix inversion was used. The method is based on the single scattering approximation which relates absorption and scattering coefficients to the sub-surface reflectance. The method allows a simultaneous determination of different constituents such as chlorophyll, particulate matter and gelbstoff. Additionally, the method can be generalized for other lakes, dates and sensors, since the model parameters can be derived independently of image data. Various inherent optical parameters of lake water were analysed in detail. Special focus was put on the scattering coefficient as it varies strongly in inland waters. Calculations based on Mie theory showed, that the complex refractive index and the particle size distribution are the most important factors for scattering of light in a lake. *In situ* radiometric measurements were used for the determination of the total absorption and backscattering coefficient. This analysis showed, that lakes can have highly variable constituents which are strongly influenced by dead organic and inorganic material.





The results of the retrieval of chlorophyll *a* and particulate matter based on image data were ambiguous. With the presented methods, it was difficult to separate the influence of atmospheric, air-water interface and particulate scattering effects as their signature and consequently also their influence on the measured spectrum are very similar. The fact that the dimensionality of the data was only small, was also confirmed by a principal component analysis, which showed that only three principal components are sufficient to account for 93% of the variations. The results of the determination of the signal-to-noise ratio pointed to the same direction. An image-based method showed that the variation of the signal was only three to four times the variation of the noise.





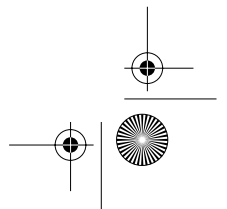
## Zusammenfassung

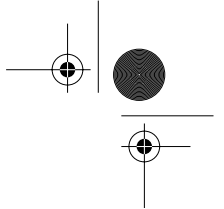
Verschiedene wissenschaftliche Programme dienen der Überwachung der Gewässerqualität. Traditionellerweise werden Wasserproben genommen, welche im Labor analysiert werden. Dies ist häufig teuer und zeitaufwendig. Diese Studie soll nun aufzeigen, inwieweit Fernerkundungsmethoden für solche Erhebungen geeignet sind. Drei Problembereiche wurden genauer untersucht: (1) Korrektur atmosphärischer Effekte, (2) Korrektur von Effekten an der Luft-Wasser-Grenzschicht, und (3) Inversion der Strahlung im Wasserkörper, welche zur Bestimmung der Qualitätsparameter, wie z.B. Chlorophyll *a* und Schwebstoff Konzentration, führt. Die dabei entwickelten Methoden wurden anhand eines Bilddatensatzes getestet, welcher mit dem abbildenden Spektrometer CASI über dem Zugersee (Schweiz) erhoben wurde.

(1) Da die Atmosphäre einen stärkeren Einfluss auf das an einem Sensor gemessene Signal haben kann, als die Strahlung die vom Wasserkörper kommt, muss die Atmosphärenkorrektur sehr sorgfältig durchgeführt werden. In dieser Studie wurde hierzu eine bildbasierte Methode entwickelt, welche sich auf das Strahlungsmodell MODTRAN/ATCOR stützt. Unter der Annahme, dass im Nahinfraroten die Strahlung aus dem Wasserkörper vernachlässigbar ist, war es möglich, die metrologische Sichtweite zu schätzen, welche im verwendeten Modell die Aerosolkonzentration bestimmt. Dies erlaubte eine pixelweise Atmosphärenkorrektur.

(2) Ist die Strahlung über der Luft-Wasser-Grenzschicht bekannt, kann die Strahlung im Wasserkörper durch Transfergleichungen für abwärts- und aufwärtsgerichtete Strahlung bestimmt werden. Die in dieser Studie bestimmte Parametrisierung zeigte dabei eine sehr gute Übereinstimmung mit radiometrischen Messungen im Walensee und Zürichsee.

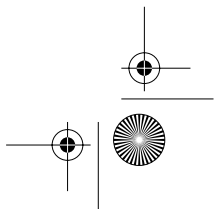
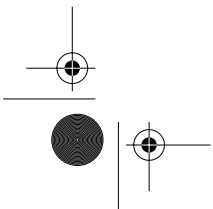
(3) Die Strahlung im Wasserkörper ist die Grundlage für die Bestimmung der Inhaltsstoffe. In dieser Studie wurde die Matrix-Inversionsmethode angewendet. Sie basiert auf der Einfachstreuungsnaheung, welche scheinbare und inhärente Parameter miteinander verknüpft, und eine gleichzeitige Bestimmung verschiedener Inhaltsstoffe wie Chlorophyll, Schwebstoff oder Gelbstoffe erlaubt. Zudem kann die Methode für andere Seen, Zeitpunkte und Sensoren verwendet werden, da die Modellparameter aus inhärenten Parametern hergeleitet werden können. Verschiedene inhärente optische Parameter wurden dabei genauer untersucht. Spezielles Gewicht wurde auf die Untersuchung der Streuung gelegt, da diese in Inlandgewässern stark variieren kann. Modellierungen, basierend auf der Mie-Theorie, zeigten, dass der komplexe Refraktionsindex und die Partikelgrößenverteilung die wichtigsten Parameter sind, welche die Streuung von Licht in Seen bestimmen. Radiometrische *in*





*situ* Messungen im Zugersee, Zürichsee und Walensee wurden für die Bestimmung des totalen Absorptions- und Streukoeffizienten verwendet. Dabei konnte gezeigt werden, dass die Zusammensetzung der Wasserinhaltsstoffe hoch variabel sein kann und stark von nicht-lebendem organischem und anorganischem Material beeinflusst wird.

Die Resultate der Inversion des Bilddatensatzes waren nicht eindeutig. So war es mit den vorgestellten Methoden nicht möglich, Einflüsse von Atmosphäre, Grenzschicht und Partikelstreuung klar voneinander zu trennen, da die Signatur dieser Komponenten und daher auch ihr Einfluss auf das am Sensor gemessene Spektrum sehr ähnlich sind. Dass die Dimensionalität der Daten nur gering war, zeigte sich auch bei der Hauptkomponentenanalyse, mit welcher sich der spektrale Informationsgehalt des Datensatzes bestimmen lässt. So reichten drei Hauptkomponenten aus, um 93% der Variationen zu erklären. Auch das Resultat der Bestimmung des Signal-Rausch-Verhältnisses führte in die gleiche Richtung. So konnte mit einer bildbasierten Methode gezeigt werden, dass die Variation des Signals im verwendeten Datensatz nur drei bis vier Mal grösser als die Variation des Rauschens war.



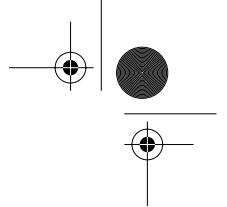
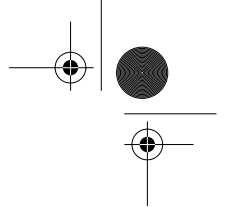


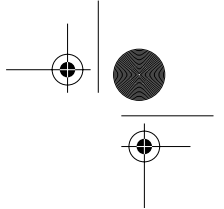
# Table of Contents

<b>Summary</b>	<b>i</b>
<b>Zusammenfassung</b>	<b>iii</b>
<b>Table of Contents</b>	<b>v</b>
<b>1. Introduction</b>	<b>1</b>
1.1 Remote-Sensing of Lakes	1
1.2 Problem Description	6
1.3 Test Sites	7
1.4 Structure of this Study	9
<b>2. Water Optics</b>	<b>11</b>
2.1 Apparent Optical Properties	12
2.2 Inherent Optical Properties	14
2.3 Radiative Transfer in Water	16
2.4 Optically Significant Constituents	21
2.5 Particle Size Distribution	23
2.6 Absorption	26
2.7 Scattering	37
2.8 Bio-Optical Model	39
2.9 Complex Index of Refraction	40
2.10 Mie Scattering	41
2.11 Determination of Water Quality Parameters	49
2.12 Review	55
2.13 Conclusions	58
<b>3. Radiometry in Natural Waters</b>	<b>61</b>
3.1 Spectroradiometer	61
3.2 Absolute Radiometric Calibration	64
3.3 Shipboard Measurements	66
3.4 Determination of Inherent Parameters	67
3.5 LI-COR Measurements in Lake Zug	68
3.6 GER1500 DFOV Measurements in Lake Zürich and Walensee	72
3.7 Conclusions	79
<b>4. Atmosphere and Air-Water Interface</b>	<b>81</b>
4.1 Atmospheric Radiative Transfer Code MODTRAN	82
4.2 Introduction to ATCOR 4	83
4.3 At-Sensor Radiance	87



4.4	Adjacency Effects	89
4.5	Experimental Determination of Adjacency Effects	92
4.6	Air-Water Interface Processes	93
4.7	Air-Water Interface Transfer Equations	95
4.8	Verification of the Transfer Equations	102
4.9	Conclusions	103
<b>5.</b>	<b>Imaging Spectroscopy</b>	<b>105</b>
5.1	Imaging Spectrometry	105
5.2	CASI Campaign in Lake Zug	106
5.3	Information Content	109
5.4	Atmospheric Correction	115
5.5	Air-Water Interface Correction	125
5.6	Evaluation of the Inversion Method	125
5.7	Determination of Water Quality Parameters in Lake Zug	130
5.8	Conclusions	138
<b>6.</b>	<b>Conclusions and Outlook</b>	<b>141</b>
6.1	Methodology	141
6.2	Sensor Requirements	143
6.3	Classical Limnology versus Remote-Sensing	144
<b>Appendix A</b>	<b>Instrument Specifications</b>	<b>147</b>
<b>Appendix B</b>	<b>Computer Hardware and Software</b>	<b>149</b>
<b>References</b>		<b>153</b>

The cover page shows Lake Zug and Mount Rigi at the day of the CASI campaign and the algae *Dinobryon divergens* which is frequent in this lake (image of the algae courtesy of F. Schanz, Limnological Station, University of Zürich).



# Chapter 1

## Introduction

“Blue has no dimensions.”  
Yves Klein, painter

The goal of this study is to demonstrate the potential of imaging spectroscopy for the determination of water quality parameters such as chlorophyll *a* or suspended matter concentrations.

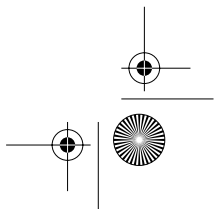
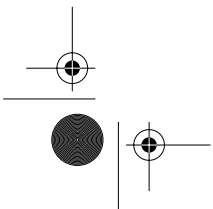
In the introduction, the state of the art of remote sensing of lakes, the problem description, the test sites, and the structure of the study are presented.

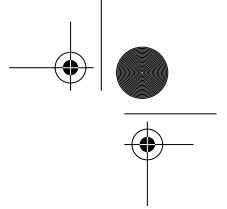
### 1.1 Remote-Sensing of Lakes

---

Lakes serve as natural sewage plants due to the long residence time of water. Consequently, different substances accumulate, especially when human activities increase the input of anthropogenic substances. A well-known example is phosphate, for which the accumulation was forced by the intensification of agricultural activities and by the use of this substance in detergents. Since phosphate is often the limiting nutrient for algae, the phytoplankton concentration increased. Algae sinking to the lake bottom consume oxygen. However, if the oxygen concentration in the sediment is too low, iron is reduced and consequently phosphate in the sediment resuspends, leading to an additional deterioration of water quality. The consequences are algal blooms, odours caused by hydrogen sulphide, decreases in fish population, and reduction of reed areas.

Since lakes are ecosystems building valuable niches for an extensive flora and fauna, and since they are often used as drinking water reservoirs or for free-time activities, there is a general public interest to monitor the water quality. Traditionally, water samples are taken and analysed in the laboratory, which is time and money consuming. Remote-sensing techniques may complement or even replace these measurements as they have the advantage of allowing a quasi-instantaneous view of vast regions, and a repetitive investigation of even remotely located places. There are various limnological parameters that can potentially be determined by remote-sensing techniques:





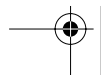
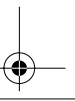
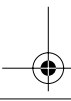
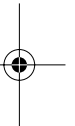
- lake water constituents (e.g., chlorophyll *a*, gelbstoff, particulate matter),
- transparency (Secchi depth<sup>1)</sup>),
- algae fluorescence,
- biological primary production,
- lake characteristics (e.g., water depth, boundaries, surface area and volume),
- surface roughness,
- circulation patterns (e.g., currents, eddies and waves), and
- skin surface temperature.

For the determination of each parameter, different parts of the electromagnetic spectrum are used. Microwave remote-sensing gives information about the roughness of the water surface, and thermal remote-sensing allows the determination of the skin surface temperature (SST). However, these two methods merely enable the investigation of the water surface as the water absorption is high in these parts of the spectrum. In order to investigate lake quality parameters, the visible part has to be used instead.

Remote-sensing methods can be classified by their energy source. *Active* systems provide their own electromagnetic source (e.g., laser fluorescence sensor or radar). They include the ability to obtain measurements regardless of the time of day or season and can be used for examining wavelengths that are not sufficiently provided by the sun or to better control the way the target is illuminated. However, active systems require large amounts of energy to illuminate targets adequately. *Passive* systems use the solar radiation that is reflected or absorbed and then re-emitted. Here the main goal is the determination of water quality parameters such as chlorophyll *a*, gelbstoff and suspended matter. This is the subject of this study.

Light detected at a sensor is influenced by different physical processes (Fig. 1.1): sunlight is transmitted through the atmosphere and enters the waterbody where it is absorbed or scattered. A part of the scattered light find its way back across the air-water interface and through the atmosphere and is detected by a sensor. Thus, in order to determine lake water quality parameters from remotely sensed data, three main problems must be solved: (1) correction for atmosphere effect, (2) correction for the air-water interface effect, and (3) inversion of the sub-surface reflectance.

<sup>1)</sup> The Secchi depth is the maximum depth where a white disk lowered in the water is still visible, and is therefore also a measure for the penetration depth of optical sensors.



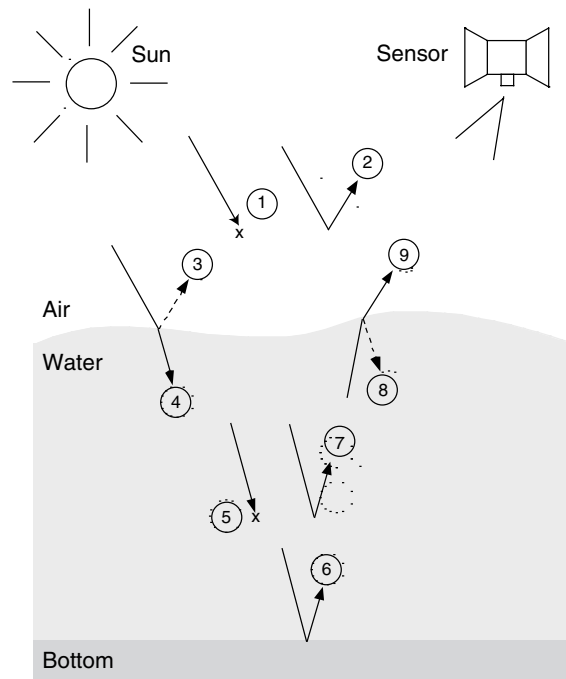
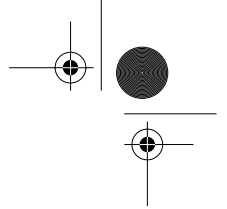


**Figure 1.1** The radiation from the sun to the sensor is influenced by different processes. 1: atmospheric absorption, 2: atmospheric scattering (e.g., path scattered radiation), 3: external surface reflection, 4: transfer through the air-water interface, 5: absorption, 6: interaction with the lake bottom, 7: particle scattering, 8: internal interface reflection, 9: radiation leaving the waterbody.

While remote-sensing of open ocean water is well-established (Mobley, 1994), freshwater environments are more challenging since they differ in several aspects:

- higher concentrations and variations of coloured dissolved organic matter (gelbstoff) masking the phytoplankton absorption,
- higher concentration of inorganic particulate matter,
- different particle size distribution,
- higher variation of phytoplankton species (during a vegetation period and from lake to lake),
- stratification of lake water constituents in the upper layers of the water column,



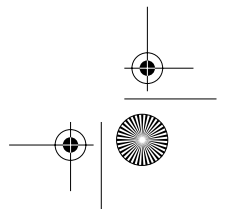
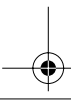
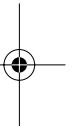
- higher spatial and temporal variations,
- smaller spatial extensions of the water area, and
- stronger influence by human activities.

All these aspects lead to missing correlations between different lake water quality parameters. This implicates that statistical approaches which were successful in ocean waters can generally not be applied on inland waters. These differences are caused by riverine inputs of particulate matter, resuspension processes from the sediment, and lower mixing intensity in the upper part of the water column. However, as the behaviour of ocean coastal waters resembles inland waters, the experience gained there can serve as a basis for remote-sensing of lakes.

A number of different methods for the determination of water quality parameters exist being strongly related to the characteristics of the available sensors. The first water quality parameter maps were derived from the first MULTISPECTRAL SENSOR (MSS) launched on LANDSAT 1 in 1972 (see Middleton and Marcell, 1983). It included four spectral bands with reasonably high spatial resolution (80 m), allowing the investigation of small inland lakes. Since the spectral resolution was rather low (100 nm), statistical models could be used only. Since 1972, a total of four MSS were launched. THEMATIC MAPPER (TM) which was launched on LANDSAT 4 and 5 in 1982 and 1984, respectively, with seven spectral bands, the ENHANCED THEMATIC MAPPER PLUS (ETM+) launched in 1999 with an additional panchromatic band, as well as SPOT HRV launched in 1986, 1990, and 1993 with three spectral bands and a panchromatic band had the same limitations as MSS. However, despite the instrument restrictions, encouraging results were derived that allowed (and still allow) to gain experiences and knowledge on the ecosystem lake.

The COASTAL ZONE COLOR SCANNER (CZCS) on NIMBUS-7 launched in 1978 was the first system in space to specifically address aquatic environments. It contained four 20 nm wide spectral bands at 443 nm, 520 nm, 550 nm, and 670 nm to measure pigment absorption and pigment scattering, one band at 700-800 nm for land and cloud detection, and one band at 10.5-12.5  $\mu\text{m}$  for the determination of the surface temperature. The sensor specifications allowed the generation and validation of not only statistical approaches, but also of physics-based inversion methods. The CZCS was radiometrically more sensitive than previous systems, such as MSS or TM, but with a spatial resolution of about 1 km, which is suitable on a global scale, the application to inland waters was not possible either.

Today's spaceborne sensors, dedicated to the investigation of water environments, nonetheless have spatial resolutions which allow the investigation of large water bodies only (Tab. 1.1). Therefore, most research on limnologi-



## 1.1 Remote-Sensing of Lakes

cal systems is based on airborne systems, because of their flexible use, larger number of bands (i.e., hyperspectral), as well as higher spatial and spectral resolution compared to spaceborne systems (see Chapter 5.1 for a short introduction to the technology behind the data). The latest generation of airborne imaging spectrometers offers new possibilities for the investigation of lakes. Especially the use of physics-based methods for the determination of lake water parameters is possible. Some important sensors are AVIRIS (Porter and Enmark, 1987), CASI (Anger et al., 1990), ROSIS (van der Piepen, 1995), and HYMAP (Cocks et al., 1998).

In the context of inland water remote-sensing, there are various important studies which will be mentioned throughout this text. An overview of the history and the state of the art of inland water remote-sensing is given in the European Commission manual (EC, 1999) where many references can be found. A summary of published work covering the application of remote-sensing data to inland water quality studies from 1984 to 1993 is found in Dekker et al. (1995).

**Table 1.1** Previous, present and future satellite systems: names with operation time in *italic*, ground sampling distance  $\Delta x$  at nadir, repetition rate  $\Delta t$ , and number of channels with their full width at half maximum of the visible and near infrared bands.

Systems <sup>1)</sup>	$\Delta x$	$\Delta t$	# Bands
CZCS (NIMBUS-7) <i>1978-1986</i>	825 m	17 d	6 (20-100 nm)
OCTS (ADEOS) <i>1996-1997</i>	700 m	3 d	8 (20 nm)
MOS (IRS P3, PRIRODA) <i>1996-</i>	520 m/650 m	28 d	12 (10 nm)
SEAWIFS (SEASTAR) <i>1997-</i>	1100 m	16 d	8 (20 nm)
MODIS (TERRA) <i>2000-</i>	500 m/1000 m	1 d	36 ( $\geq 10$ nm)
COIS (NEMO) <i>2001?</i>	30/60 m	7 d	210 (10 nm)
MERIS (ENVISAT-1) <i>2001?</i>	250/1000 m	3 d	15 ( $\geq 2.5$ nm)
GLI (ADEOS-2) <i>2001?</i>	250/1000 m	4 d	34 (10 nm)

<sup>1)</sup> CZCS: Coastal Zone Color Scanner  
 OCTS: Ocean Color and Temperature Scanner  
 MOS: Modular Optoelectronic Scanner  
 SEAWIFS: Sea-viewing Wide Field-of-view Sensor  
 MODIS: Moderate Resolution Imaging Spectrometer  
 COIS: Coastal Ocean Imaging Spectrometer  
 MERIS: Medium Resolution Imaging Scanner  
 GLI: Global Imager

## 1.2 Problem Description

Although many studies have been made in remote-sensing of lakes, the application of analytical models was hardly performed. The purpose of this study is to demonstrate the potential of imaging spectroscopy for the retrieval of lake water quality parameters based on such models. Special emphasis is put on the determination of chlorophyll *a* which is a useful parameter for the determination of water quality and the trophic status due to two reasons (Fig. 1.2). First, it is the driving force of the primary production due to its capability to transform electromagnetic energy into chemical energy (i.e., biomass). Consequently, chlorophyll is directly coupled to the *in situ* produced biomass, and is correlated with the oxygen concentration (determining the redox potential in the lake) and other limnological parameters of interest such as phosphate and nitrogen. Secondly, it changes the spectral signature of radiation directly by this absorption process and indirectly by changing the scattering properties (i.e., building of particulate matter), such that it is potentially detectable by remote-sensing devices.

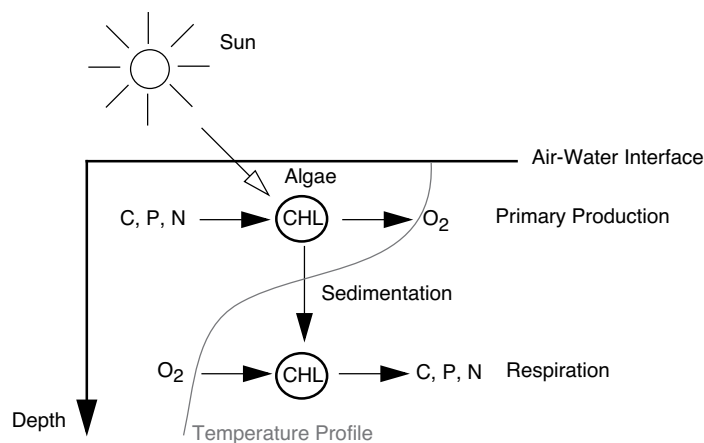
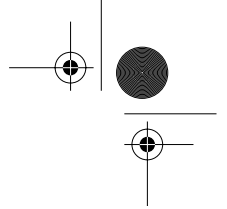


**Figure 1.2** Carbon (C), phosphate (P), and nitrogen (N) are the basis of the primary production of algae which is driven by solar light. Chlorophyll (CHL) transforms the electromagnetic energy in chemical energy. Most of the dead algae sink to lower layers where they are respired by microbiological processes. In highly productive lakes, the primary production leads to a supersaturation of oxygen (O<sub>2</sub>) in the top layer (epilimnion) whereas the respiration causes an oxygen deficit in the bottom layer (hypolimnion). From spring to autumn, these two regions are separated by a strong density stratification caused by a high temperature gradient.

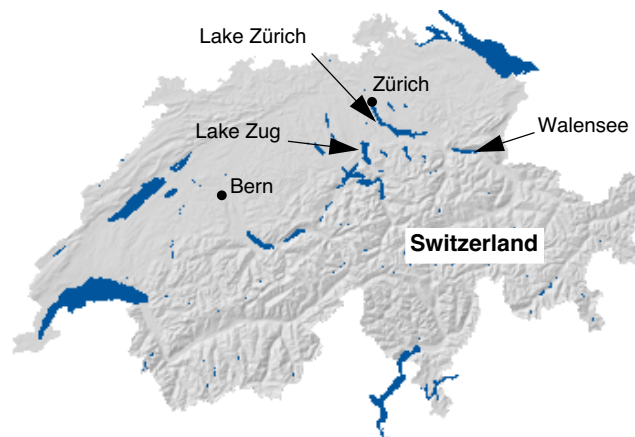


The main focus of this study is put on the demonstration of imaging spectroscopy for the determination of lake water quality parameters such as chlorophyll *a* or suspended matter concentrations. Relevant parameters influencing this determination shall be determined and investigated in more detail. Among other things, following questions are addressed in this study with special focus put on the characteristics of lakes:

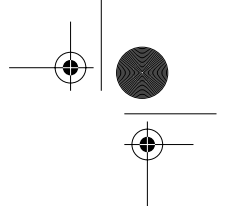
- How does the composition of natural water influence the radiation? How can water quality parameters be determined from spectral data? How can the influence of several parameters on the spectrum be separated?
- How can radiation be measured in natural waters?
- How are atmospheric and interface corrections performed on image data?
- What can be expected from analysing imaging spectrometer data? What is the information content of the data?

### 1.3 Test Sites

The measurements have been performed in three different Swiss lakes: Lake Zug, Lake Zürich, and Walensee (Fig. 1.3). Tab. 1.2 gives a short summary of the most important parameters describing these lakes.



**Figure 1.3** Test sites: Lake Zug, Lake Zürich, and Walensee (map courtesy of I. Leiss).

**Table 1.2** Characteristics of the investigated lakes (BUWAL, 1994).

	Lake Zürich	Walensee	Lake Zug
Area	85 km <sup>2</sup>	24 km <sup>2</sup>	38 km <sup>2</sup>
Maximum depth	136 m	145 m	198 m
Altitude above sea level	406 m	420 m	414 m
Water exchange time	10 weeks	17 months	15 years
Eutrophic state <sup>1)</sup>	mesotroph	oligotroph	mesotroph

<sup>1)</sup> oligotroph: natural lake with low concentration on chlorophyll and nutrients; mesotroph: higher concentration on chlorophyll and nutrients for example due to human activities

### *Lake Zug (Zugersee)*

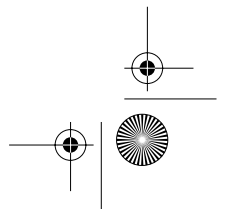
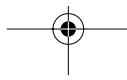
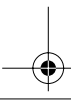
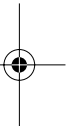
Lake Zug is located in central Switzerland next to the slopes of Mount Rigi (see cover page). The lake is divided into two basins by a peninsula. In spite of this bottleneck, the transport of water and its constituents are only little reduced due to internal waves and wind-driven slow currents. The exchange time between the two basins is in general less than 30 days.

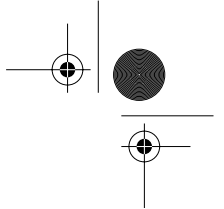
In the 19<sup>th</sup> century, the lake was still poor on nutrients. This changed rapidly during the 20<sup>th</sup> century because of increased phosphate input caused by domestic sewage (detergents) and increased agricultural activities in the catchment basin of Lake Zug. These high concentrations of phosphorous lead to algae blooms and oxygen free zones at the bottom of the water body. The prohibition of phosphate in the detergents by law in 1986 in Switzerland improved the situation only slowly because of the unchanged — or even growing — phosphate input by the agricultural activities and also by the high water exchange time of the whole lake of 15 years. In order to monitor these changes, continuous *in situ* measurements are performed since 1968 (Wüest et al., 1994).

### *Lake Zürich (Zürichsee)*

The basin of Lake Zürich was built by glaciers of the Rhine and Linth region. The lake is divided into two parts by the dam at Rapperswil, the Obersee with 20 km<sup>2</sup> and the Zürichsee (Untersee) with 65 km<sup>2</sup>. Both parts are connected by three narrow passages with a water depth of 2-8 m. The Linthkanal, which connects Walensee with Obersee is the most important inflow.

Untersee has a pronounced temperature stratification, whereas the temperature at the Obersee decreases linearly with depth, caused by the lack





## 1.4 Structure of this Study

9

of wind driven turbulence, and the high water flow. Sediments show oxygen lack already at the end of the 19<sup>th</sup> century. Since purification plants are put into operation and phosphate in the detergents have been prohibited, the water quality has improved significantly.

### *Walensee*

Walensee forms an uniformly, elongated basin which is bordered to the north by the Churfirsten, and to the south by the mountains of the Glarner Alps. The exposition to westerly and easterly winds and the high sediment concentration in the main inflow Linth lead to strong vertical transport processes. The water quality is excellent due to low agricultural activities in the catchment and the probable phosphate elimination by adsorption to suspended sediments.

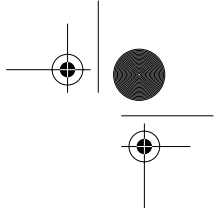
## 1.4 Structure of this Study

The questions posed in Chapter 1.2 determine the structure of this study.

In Chapter 2, a summary of the water optical models is presented. Models are important in different ways. First, they are needed to interpret observation data, secondly, they are required to predict changes of the observed radiation if inherent and apparent parameters change, and thirdly, they can be used for the determination of water quality parameters if compared with radiometric measurements. Optically significant processes were analysed in detail such as gelbstoff and phytoplankton absorption as well as particle scattering which is described with Mie theory. Experiments were performed in Lake Zug, Lake Zürich and Walensee.

Chapter 3 gives insight to the problems associated to radiometric shipboard measurements which allow the optical investigation of water systems without the problems associated to remote-sensing data such as atmospheric correction or temporal and spatial allocation. As imaging spectrometer measurements are rarely available, this is often the only possibility for multi-temporal investigations. Own spectral *in situ* measurements are described in order to determine the dependence of inherent parameters on chlorophyll *a*.

Remote-sensing always leads to the problem that the influence of the atmosphere has to be corrected. This is illustrated in Chapter 4. Due to the small spatial extension of lakes, special focus is put on the adjacency effect which influences the retrieved signal from the lake by a remote-sensing device. Since the air-water radiation transfer partly depends on the same parameters as the atmospheric correction, this aspect is also covered here. The

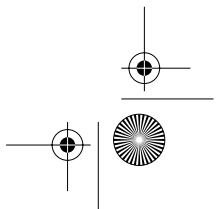
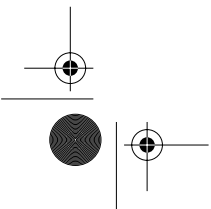


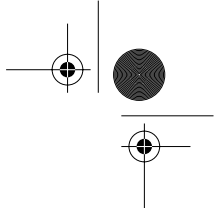
transfer functions will be tested with own measurements in Lake Zürich and Walensee.

In Chapter 5, the above-mentioned methods are applied on image data of the CASI spectrometer flown over Lake Zug. Problems that arise with the analysis of image data are illustrated. In particular, the information content, the image based determination of the meteorological range which is related to the aerosol concentration, and the determination of chlorophyll *a* are presented.

Chapter 6 discusses the results of this study, defines sensor characteristics adequate for lake monitoring, and compares traditional limnological methods with remote-sensing methods.

In Appendix A, the instrument specifications of the spectrometers, and in Appendix B, the computer hardware and software, as well as the modules developed in this study are described.



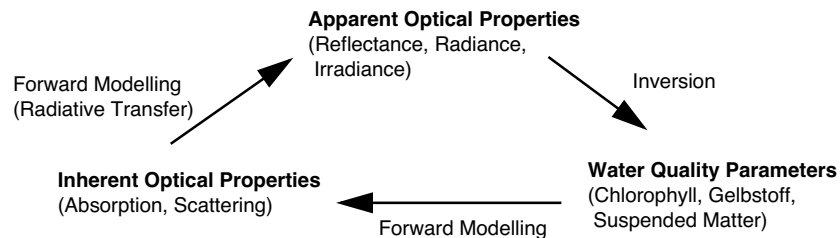


## Chapter 2

# Water Optics

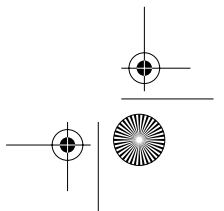
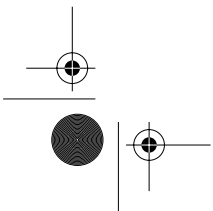
In this chapter, the basics of water optics are presented which are essential for the understanding of physics-based inversion methods.

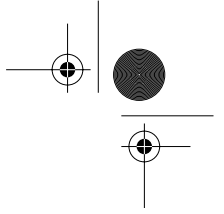
First, inherent and apparent parameters are used to describe the water light field. *Inherent* optical properties summarize the influence of optical properties of a bulk of particles. They depend on the medium only and are independent of the light field within the medium. Absorption and scattering coefficients belong to this group. *Apparent* optical properties depend on both the medium (i.e. inherent parameters) and the geometric directional structure of the ambient light field. The connection between apparent and inherent properties is provided by radiative transfer theory which will build the basis for the determination of lake water quality parameters (Fig. 2.1).



**Figure 2.1** Dependence of water quality parameters, inherent and apparent optical properties.

In the following sections, optically significant processes were analysed in detail such as gelbstoff and phytoplankton absorption as well as particle scattering which is described with Mie theory. Finally, it is shown how the influence of various parameters on the spectral signature can be used for their determination, with main focus on chlorophyll *a*.





## 2.1 Apparent Optical Properties

Apparent optical properties depend on the light field and can therefore only be determined *in situ*.

The radiance  $L$  is defined as the radiant energy  $\Phi$  that can be measured with an instrument per unit solid angle  $\Delta\Omega$ , unit area  $\Delta A$  and spectral interval  $\Delta\lambda$  during a time interval  $\Delta t$ . This leads to:

$$L(\xi, \lambda, z) \equiv \frac{\partial^4 \Phi}{\partial t \partial A \partial \Omega \partial \lambda} \quad [\text{W m}^{-2} \text{ sr}^{-1} \text{ nm}^{-1}], \quad (2.1)$$

where  $\xi$  denotes the photon path direction,  $\lambda$  the wavelength, and  $z$  the water depth.

The irradiance is defined as the radiance integrated over an entire hemisphere<sup>1)</sup>. According to the two possibilities for the measurement, there are two different definitions for the irradiance. Spherical diffusors (Fig. 2.2, left) are equally sensitive to photons from any direction of the hemisphere. They measure the *scalar* irradiance  $E_o$  which is defined for the downward hemisphere  $\Xi_d$  by:

$$E_{o,d}(z, \lambda) \equiv \int_{\xi \in \Xi_d} L(z, \xi, \lambda) d\Omega \quad [\text{W m}^{-2} \text{ nm}^{-1}]. \quad (2.2)$$

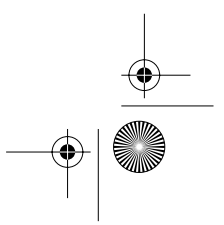
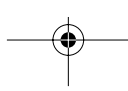
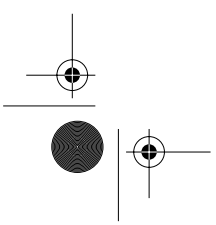
The downward hemisphere denotes the hemisphere which encompasses all incoming light pointing downward. Accordingly,  $E_{o,u}$  can be defined for the opposite direction. In the special case that radiance is distributed uniformly across the hemisphere, the scalar irradiance is equal to  $2\pi L$ .

Diffusors with plane surfaces only measure the component of the light which is perpendicular to this surface (Fig. 2.2, right). Thus, the radiance is weighted with the cosine of the incident photon direction  $\theta$ . These instruments measure the *plane* irradiance  $E$  defined for the downward hemisphere  $\Xi_d$  by:

$$E_d(z, \lambda) \equiv \int_{\xi \in \Xi_d} L(z, \xi, \lambda) |\cos \theta| d\Omega \quad [\text{W m}^{-2} \text{ nm}^{-1}]. \quad (2.3)$$

Again the upward plane irradiance  $E_u(z, \lambda)$  can be defined. Note that in case of uniformly distributed radiance, the plane irradiance is now equal to  $\pi L$ .

<sup>1)</sup> By definition, the irradiance does not mean an integration over an entire hemisphere, but only an integration over a solid angle. However, in water optics, the concept of irradiance usually refers to the integration over the entire hemisphere.



## 2.1 Apparent Optical Properties

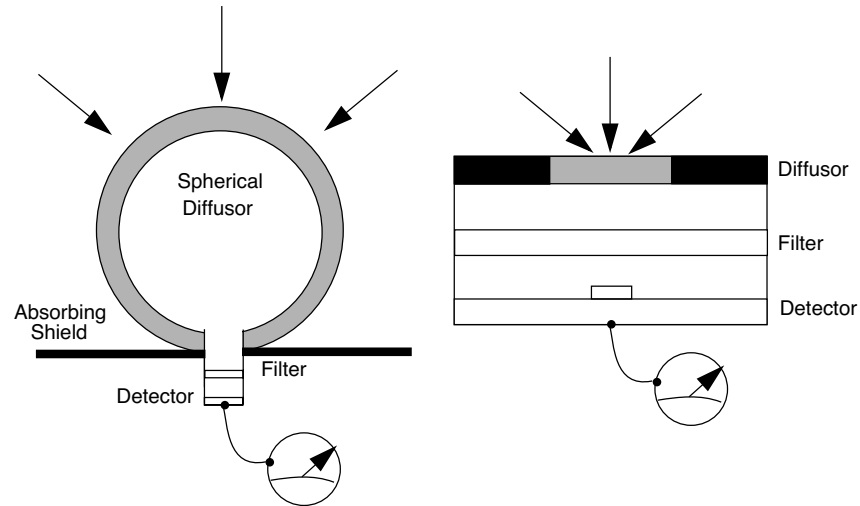


**Figure 2.2** Schematic designs of irradiance collectors. The left one is measuring the scalar irradiance, the right one the plane irradiance (after Mobley, 1994).

The reflectance is defined as the upwelling radiation divided by the downwelling radiation at the same depth. Different definitions are in use. The irradiance reflectance (also called volume reflectance)  $R$  is defined as:

$$R(z, \lambda) \equiv \frac{E_u(z, \lambda)}{E_d(z, \lambda)} \quad [-], \quad (2.4)$$

where all parameters are a function of wavelength  $\lambda$  and depth  $z$ . In water, the transformation between  $E_u$  and  $L_u$  is provided by the factor  $Q$  [sr]:

$$E_u(z, \lambda) \equiv Q(z, \xi, \lambda) \cdot L_u(z, \xi, \lambda) \quad [\text{W m}^{-2} \text{ nm}^{-1}]. \quad (2.5)$$

If the radiance is distributed uniformly over the hemisphere,  $Q$  is equal to  $\pi$ . But usually, this is not the case though. Morel and Gentili (1993) found that  $Q$  generally ranges between 3 and 6, with the low values occurring in clear waters at blue wavelengths, and with the high values occurring for higher chlorophyll concentrations and red wavelengths.

Combining Eq. 2.4 and Eq. 2.5 leads to:

$$\frac{R(z, \lambda)}{Q(z, \xi, \lambda)} = \frac{L_u(z, \xi, \lambda)}{E_d(z, \lambda)} \text{ [sr}^{-1}\text{]}. \quad (2.6)$$

The remote-sensing reflectance  $R_{Rs}$  is defined as:

$$R_{Rs}(\xi, \lambda) \equiv \frac{L_w(\xi, \lambda)}{E_d(a, \lambda)} \text{ [sr}^{-1}\text{]}, \quad (2.7)$$

where  $L_w(\xi, \lambda)$  is the water-leaving radiance<sup>1)</sup> containing the information about the water constituents, and  $E_d(a, \lambda)$  is the total downwelling irradiance just above the air-water interface.

If the optical relevant lake water constituents were uniformly distributed in the water column, the downwelling irradiance decreases exponentially with depth. The decrease is described with the diffuse attenuation coefficient of the downwelling irradiance  $K_d$ :

$$K_d(z, \lambda) \equiv -\frac{1}{E_d(z, \lambda)} \frac{\partial E_d(z, \lambda)}{\partial z} \text{ [m}^{-1}\text{]}. \quad (2.8)$$

If  $K_d$  is assumed to be constant with depth, Eq. 2.8 can be written as

$$E_d(z, \lambda) = E_d(0, \lambda) \exp[-K_d(z, \lambda) \cdot z]. \quad (2.9)$$

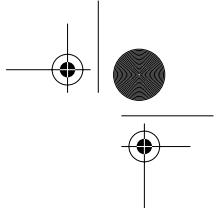
It is often of interest to know the penetration depth for remote-sensing purposes which is defined as the depth of the water layer from which 90% of the diffusely reflected irradiance measured by a sensor originates<sup>2)</sup>. Gordon and McCluney (1975) show that for a homogeneous water body, this is the depth at which the downwelling in-water irradiance drops to  $1/e$  of its surface value. According to Eq. 2.9, this is equal to  $1/K_d$  if the diffuse attenuation coefficient is constant over depth.

## 2.2 Inherent Optical Properties

When light comes into a small volume of water of a certain thickness, a portion of the light beam is transmitted, a second portion is absorbed and transformed into chemical energy or emitted at longer wavelengths, and a third portion is scattered off the beam at a certain angle. The spectral inherent parameters are defined accordingly. The spectral absorption coefficient  $a(\lambda)$

1) The concept "water-leaving radiance" is commonly used in water optics.

2) Excluding reflection at the air-water interface.



## 2.2 Inherent Optical Properties

$[m^{-1}]$  is the fraction of incident power that is absorbed per unit distance. Accordingly, the scattering coefficient  $b(\lambda) [m^{-1}]$  is the fraction of incident power that is scattered. Due to practical reasons, the transmitted radiation is included into the scattered portion with scattering angle equals to 0.

The volume scattering function  $\beta(z, \psi, \lambda)$  describes the angular dependence of the scattering. It is defined as the fraction of incident power scattered off the beam by an angle  $\psi$  into a solid angle  $\Delta\Omega$  around  $\psi$  per unit distance. Integrating  $\beta(z, \psi, \lambda)$  over all directions leads to the scattering coefficient:

$$b(z, \lambda) \equiv \int_{Sphere} \beta(z, \psi, \lambda) d\Omega = 2\pi \int_0^\pi \beta(z, \psi, \lambda) \sin \psi d\psi [m^{-1}]. \quad (2.10)$$

The last equation is valid as scattering is generally azimuthally symmetric to the incident direction. Dividing the integration in forward scattering,  $0 \leq \psi \leq \pi/2$ , and backscattering,  $\pi/2 \leq \psi \leq \pi$ , leads to the spectral forward  $b_f$  and backward  $b_b$  scattering coefficients, respectively:

$$b_f(z, \lambda) \equiv 2\pi \int_0^{\pi/2} \beta(z, \psi, \lambda) \sin \psi d\psi [m^{-1}], \quad (2.11)$$

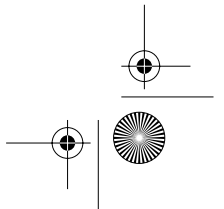
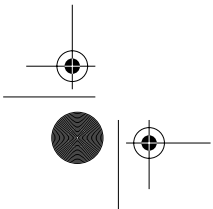
$$b_b(z, \lambda) \equiv 2\pi \int_{\pi/2}^\pi \beta(z, \psi, \lambda) \sin \psi d\psi [m^{-1}]. \quad (2.12)$$

In order to remove the absolute amplitude of the scattering  $b(\lambda)$  from the angular distribution, the spectral volume scattering *phase* function  $\tilde{\beta}$  is defined:

$$\tilde{\beta}(z, \psi, \lambda) \equiv \frac{\beta(z, \psi, \lambda)}{b(z, \lambda)}. \quad (2.13)$$

Since the main scatterers are approximately the same size as the visible wavelengths, the scattering process is best described with Mie theory (Chapter 2.10). A typical property of Mie scattering is that the phase function is strongly peaked in the forward direction.

Combining Eq. 2.10 and Eq. 2.13 gives the normalization condition for the phase function:



$$2\pi \int_0^{\pi} \tilde{\beta}(z, \psi, \lambda) d\psi = 1. \quad (2.14)$$

The total absorption and scattering coefficients consist of the contribution of water and its constituents. According to Beer's law, we can write:

$$a(z, \lambda) = a_w(z, \lambda) + \sum_i C_i(z) a_i^*(z, \lambda) \quad [\text{m}^{-1}], \quad (2.15)$$

$$b(z, \lambda) = b_w(z, \lambda) + \sum_i C_i(z) b_i^*(z, \lambda) \quad [\text{m}^{-1}], \quad (2.16)$$

and

$$b_b(z, \lambda) = b_{b,w}(z, \lambda) + \sum_i C_i(z) b_{b,i}^*(z, \lambda) \quad [\text{m}^{-1}], \quad (2.17)$$

where  $C_i$  is the concentration and  $a_i^*$ ,  $b_i^*$  and  $b_{b,i}^*$  are the *specific* coefficients of constituent  $i$ , and  $a_w$ ,  $b_w$  and  $b_{b,w}$  the coefficients of water, respectively. An analogous equation can be stated for the volume scattering function. Note that Beer's law is only valid for low concentrations.

The beam attenuation coefficient  $c(\lambda)$  includes the effects of both absorption and scattering:

$$c(z, \lambda) \equiv a(z, \lambda) + b(z, \lambda) \quad [\text{m}^{-1}]. \quad (2.18)$$

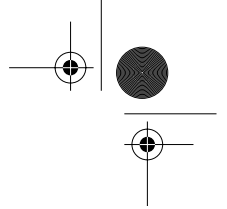
In water optics, often the optical depth  $\xi$  is used instead of the geometric depth  $z$ :

$$d\xi \equiv c(z, \lambda) dz \quad [-], \quad (2.19)$$

### 2.3 Radiative Transfer in Water

The radiative transfer equation (RTE) links apparent and inherent optical properties:

$$\begin{aligned} \frac{\partial L(z, \xi, \lambda)}{\partial z} \cos(\xi) &= -c(z, \lambda) L(z, \xi, \lambda) \\ &+ \int_{\Xi} L(z, \xi', \lambda) \beta(z, \xi' \rightarrow \xi, \lambda) d\Omega + S(z, \xi, \lambda) \end{aligned} \quad (2.20)$$



where  $\xi$  is the viewing zenith angle. The first term describes the beam attenuation (Eq. 2.18), the second term the integration of the scattering from all directions  $\xi'$  in the viewing direction  $\xi$ , and the third term the internal sources  $S$  (fluorescence and illuminance); in most cases, the latter term is neglected.

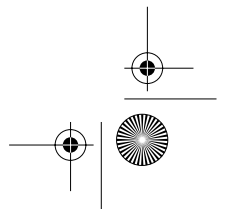
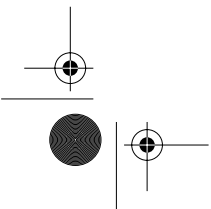
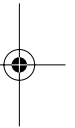
The RTE cannot be solved *analytically* for the radiance  $L$  as a function of wavelength, water depth and viewing direction. But there are several methods to obtain  $L$  for defined *discrete* wavelengths, water depths and viewing directions.

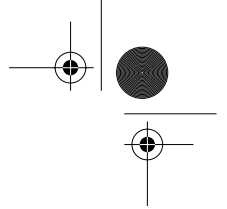
Reference and operational models can be distinguished. *Reference models* describe the reality almost exactly but are generally not invertible. *Operational models*, on the other hand, introduce some approximations which allow an operational inversion. The single scattering approximation is one example of an invertible operational model.

#### Reference Models

Different kinds of reference radiative transfer models are known, each of them showing strengths and weaknesses:

- *Monte Carlo Simulation*. A single photon is followed along its path from above the water surface into the water body. If the photon is absorbed or leaves the water body again, a new photon is simulated. The destiny of each photon is stored. This procedure is repeated until the results are statistically stable ( $10^6$  photons). The reciprocal of the attenuation coefficient (Eq. 2.18) represents the free path length of the photons, and the ratio of absorption to attenuation coefficient defines the probability that the photon is absorbed at the end of the free path length. The direction is determined by the phase function. The Monte Carlo method is mathematically simple and leads to the most accurate results of all models. However, it requires considerable computing time. Kirk (1981) shows how to implement such a procedure.
- *Finite Differences Method*. The RTE and the volume scattering function considering boundary conditions are rewritten with finite differences (Helliwell, 1985). This method is fast and mathematically simple, but the accuracy - which may be lowest for all presented methods - strongly depends on the choice of the calculation scheme and on the size of the spatial grid.
- *Discrete Ordinates Method*. First, the RTE is represented by Fourier cosine series, and the phase function is expressed by Legendre polynomials (Mobley, 1994). The integral term is approximated by a Gaussian quadrature sum, resulting in a system of coupled ordinary differential equa-





tions that can be solved with eigenmatrix methods. The method provides a very efficient way of computing irradiance and radiance distributions in homogeneous waters. However, the method becomes numerically inefficient if the inherent optical properties are depth dependent, or if detailed radiance distributions are required for highly peaked phase functions.

- *Finite Element Method.* Bulgarelli et al. (1999) show a possible implementation of this method. First, they also represent the RTE by Fourier cosine series and the phase function by Legendre polynomials. Then they solve the resulting partial differential equation with the finite element method which uses basis functions for the approximation of the solutions allowing to focus on a region of interest. This method is faster and more accurate than the discrete ordinates method due to the inherent flux conservation.
- *Invariant Embedding Method.* The unit hemisphere is partitioned in quads and the radiative transfer equation and the volume scattering functions are determined for each quad. The equations are Fourier transformed leading to a set of Riccati differential equations. This method is described by Mobley (1994) who has also developed the commercial software HYDROLIGHT<sup>1)</sup>. The method allows the consideration of vertically variable inherent properties which is difficult for the discrete ordinates method, and is much faster than Monte Carlo simulations, especially for problems involving upwelling radiance. However, the disadvantage of this method is that radiances are directional (quad) averaged and not computed in specific directions.

A comparison of the above methods (except the finite difference method) is given in Mobley et al. (1993).

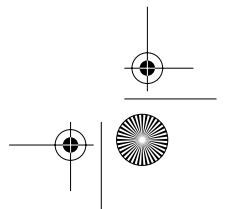
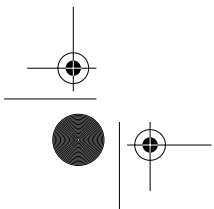
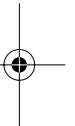
#### *Operational Models*

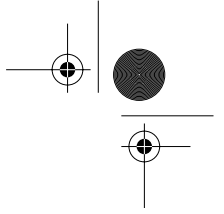
Although, reference models allow the calculation of apparent optical properties with high precision, the importance of simple analytical solutions with less accuracy should not be underestimated for the following reasons:

- the calculations are faster by several orders of magnitudes,
- it is possible to derive solutions for different specific questions, and
- the physics is easier to understand.

One of the most popular models is the single scattering approximation. Corresponding to this model, the irradiance reflectance  $R$  can be related to the

<sup>1)</sup> Version 3.1 has been freely distributed by the author, version 4.0 is now distributed commercially.





## 2.3 Radiative Transfer in Water

19

spectral total absorption coefficient  $a$  and the spectral backscattering coefficient  $b_b$ . Gordon et al. (1988) use the form:

$$\frac{R(z, \lambda)}{Q(z, \xi, \lambda)} = c_1 \omega(z, \lambda) + c_2 \omega^2(z, \lambda) \text{ [sr}^{-1}\text{]}, \quad (2.21)$$

where

$$\omega(z, \lambda) \equiv \frac{b_b(z, \lambda)}{b_b(z, \lambda) + a(z, \lambda)} \text{ [-]} \quad (2.22)$$

is the single scattering coefficient,  $Q$  [sr] the ratio of the upwelling irradiance to the upwelling radiance pointing in the viewing direction  $\xi$  (Eq. 2.5),  $c_1 = 0.0949 \text{ sr}^{-1}$  and  $c_2 = 0.0794 \text{ sr}^{-1}$ . The approximation is based on the fact, that the scattering phase function is strongly peaked in the forward direction; hence, most photons are not backscattered relative to the incident beam and remain in the beam. The approximation is better than 10% for common phase functions for sun zenith angles larger than  $20^\circ$  (Gordon et al., 1988). This is usually sufficient as often the accuracy of the inherent parameters or the measured reflectance is of the same order of magnitude. A limitation of this approximation is that the influence of the vertical distribution, bottom effects, and fluorescence are not included.

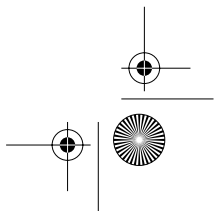
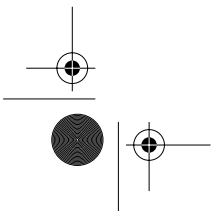
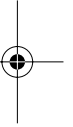
This approximation indicates that the reflectance is almost proportional to the backscattering coefficient. Of course, this has effects on the determination of water quality parameters. For example, the better the correlation of chlorophyll  $a$  to  $b_b$ , the greater the influence on the reflectance and the easier the determination of this parameter.

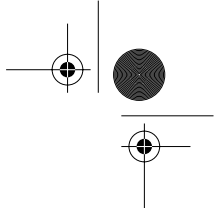
Beside the operational models for  $R$ , there are different models which relate the diffuse attenuation coefficient  $K_d$  to inherent parameters. They are all of the form:

$$K_d(z, \lambda) \propto a(z, \lambda) + b_b(z, \lambda) \text{ [m}^{-1}\text{]}. \quad (2.23)$$

This equation explains that in general,  $K_d$  is strongly correlated to  $CHL$  as the absorption is larger than the backscattering, and as the phytoplankton absorption is the most variable parameter of the total absorption.

Gordon (1989) developed a normalization for  $K_d$ , which removes the effects of the incident sky radiance distribution, so that the normalized  $K_d$  can be regarded as an inherent parameter. First, the fraction  $f$  of the direct sunlight in the incident irradiance that is transmitted across the surface into the waterbody has to be determined:





$$f(\lambda) = \frac{f_4(\lambda)\beta(\lambda)}{f_3(\lambda)(1 - \beta(\lambda)) + f_4(\lambda)\beta(\lambda)} \quad [-], \quad (2.24)$$

where  $f_3$ ,  $f_4$  are the transfer functions for downwelling diffuse and direct irradiances, respectively, and  $\beta$  is the ratio of direct to total downwelling irradiance (see Chapter 4.7 for a more detailed description of these parameters).

Secondly, the distribution function  $D_o$  has to be calculated as follows:

$$D_o(\lambda) = \frac{f(\lambda)}{\cos \theta_{sw}} + 1.197(1 - f(\lambda)) \quad [-], \quad (2.25)$$

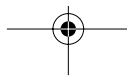
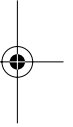
where  $\theta_{sw}$  is the sun zenith angle in water. This value of  $D_o$  is valid for flat or rough surfaces as long as  $\theta_{sw} \leq 50^\circ$ . For larger values, a correction must be applied to account for surface wave effects.

Finally, the normalization is performed with:

$$K_{d,normalized} = \frac{K_{d,measured}}{D_o} \quad [m^{-1}]. \quad (2.26)$$

The distribution function  $D_o$  reduces  $K_d$  to a value that would be measured if the sun were at its zenith, the surface were plane, and the sky were black (i.e., if there were no ambient atmosphere); this is the only situation where  $D_o = 1$ . The same normalization can be applied to depth-averaged values.

There are many different operational semi-analytical models in the literature. A selection is shown in Tab. 2.1.



## 2.4 Optically Significant Constituents

21

**Table 2.1** Semi-analytical models relating inherent and apparent parameters (valid at water depth  $z = 0$  m).

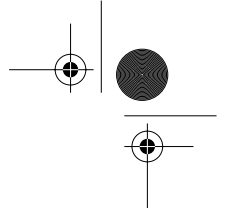
Model	Authors
$R = (0.975 - 0.629 \cos(\theta_{sw})) \frac{b_b}{a}$ <p>with <math>\theta_{sw}</math> = sun zenith angle in water</p>	(2.27) Kirk (1984)
$\omega = -0.0003 + 3.0770R - 4.2158R^2 + 3.5012R^3$	(2.28) Gordon et al. (1975), sky
$\omega = -0.0008 + 2.6987R - 3.2310R^2 + 2.8947R^3$	(2.29) Gordon et al. (1975), sun
$\frac{R}{Q} = 0.110 \frac{b_b}{K_d}$	(2.30) Gordon et al. (1988)
$\frac{K_d}{D_0} = 1.0395 \cdot (a + b_b)$	(2.31) Gordon (1989)
$\frac{b_b}{K_d/D_0} = 2.8264R(1) - 3.8947R^2(1) - 36.232R^3(1)$ <p>with <math>R(1) = R(D_0=1)</math><sup>1)</sup></p>	(2.32) Gordon (1991)

<sup>1)</sup>  $R(1)$  is determined by extrapolating from  $R(D_0)$  made for two or more  $D_0$  values.

## 2.4 Optically Significant Constituents

Natural water contains a continuous size distribution of particles ranging from water molecules of size  $\sim 0.1$  nm to fishes of size  $\sim 10$  cm. Each of these components contributes in some manner to the optical properties of a water body. Traditionally, the matter in water is divided into “dissolved” and “particulate” of organic and inorganic origin, living and non-living, autochthonous or allochthonous. The border between dissolved and particulate matter is usually set at  $0.4 \mu\text{m}$ . This is the shortest wavelength of visible light which allows the examination of material left on a filter pad with an optical microscope. While in water optics, only particulate and dissolved constituents are distinguished, limnologists distinguish between particulate ( $> 0.4 \mu\text{m}$ ), colloidal and dissolved substances, whereas the position of the border between the last two groups is somehow fuzzy.

In this study, dissolved constituents are assumed to be non-scattering. However, this is a simplification as particularly colloids can contribute significantly to the backscattering (Chapter 2.10). The optically most



important portion are humic and fulvic acids which are produced during the decay of plant matter and consequently occur in all water systems (Davies-Colley and Vant, 1987). One main source is decayed terrestrial vegetation. They absorb strongly in the blue region of the spectrum and therefore appear yellowish. Due to their colour, they are named gelbstoff, yellow substances, gilvin or coloured dissolved organic matter (CDOM). Gelbstoff is coupled with the dissolved organic matter concentration, and can influence the UV inhibition of primary production due to its strong absorption in this region of the spectrum (Arrigo and Brown, 1996). From the remote-sensing perspective, this parameter is interesting, as it can influence the determinability of other water quality parameters, and as it was hardly successfully determined by remote-sensing means yet.

Particulate matter has physical or biological origins. It can serve as a vehicle for (toxic) anthropogenic substances, and is one main source of aggradation of lakes as it determines the sedimentation rate. It makes an impact on the primary production because it can lower the euphotic depth<sup>1)</sup> due to its scattering and absorption properties. Additionally, it can have consequences on the fish population and distribution in lakes (Heege and Appenzeller, 1998). Inorganic particles are created by precipitation of calcit during the vegetation period<sup>2)</sup> or by weathering of terrestrial rocks and soils. They enter the water by river inflows or resuspension from bottom sediments. Therefore they are also called suspended matter or just suspended sediments. The optically most interesting organic matter is the algae (see discussion in Chapter 1.2). They occur at different sizes and shapes (Fig. 2.3) and form the basis of the ecosystem lake. Other organic particles are bacteria, and zooplankton<sup>3)</sup>. Particulate matter can break apart in smaller particles or even dissolve, aggregate by adsorption and coagulation to larger particles, settle out of the water column or leave the lake with the outflow (O'Melia and Bowman, 1984).

1) Depth where photosynthesis = respiration.

2) Calcium Bicarbonat  $\text{Ca}(\text{HCO}_3)_2 \leftrightarrow \text{Calcit } \text{CaCO}_3$  (not readily soluble) + Carbonic Acid  $\text{H}_2\text{CO}_3$ .

3) Viruses are generally much smaller (20-25 nm) than the wavelength of visible light and theoretically belong to the dissolved constituents.

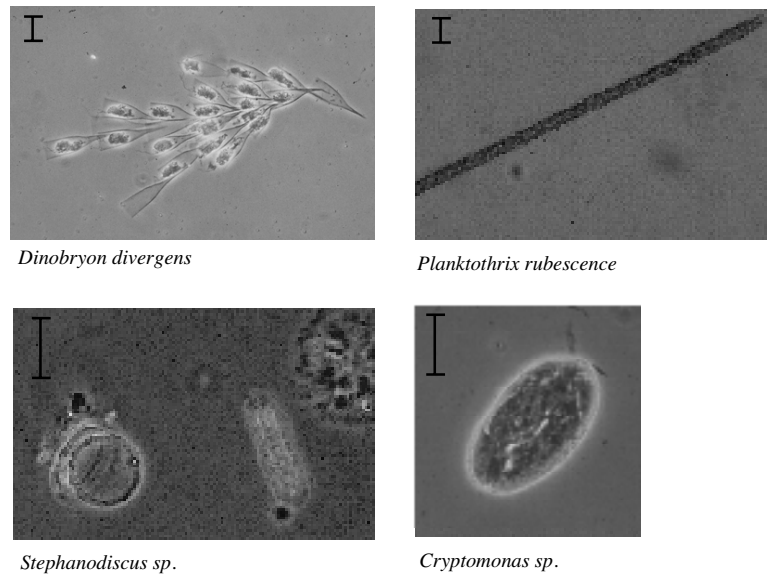


**Figure 2.3** Frequent algae in Swiss lakes. Large populations of *Cryptomonas* and *Stephanodiscus* occur in Lake Zürich in spring time, *Dinobryon* and *Planktothrix* in the summer. The bars indicate a length of 10  $\mu\text{m}$ . (Images courtesy of F. Schanz, Limnological Station, University of Zürich)

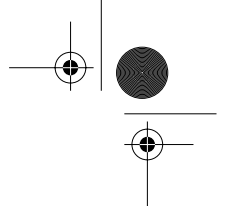
## 2.5 Particle Size Distribution

The *cumulative* size distribution  $N(x)$  [ $\text{m}^{-3}$ ] is the number of particles per unit volume with a characteristic size greater than  $x$  in a sample of particles. The size parameter  $x$  usually represents the diameter of a spherical particle, but can also represent particle volume or surface area.  $N(x)$  can be described with the Junge distribution (Mobley, 1994):

$$N(x) = k \left( \frac{x}{x_0} \right)^{-m} [\text{m}^{-3}], \quad (2.33)$$

where  $k$  sets the scale,  $x_0$  is a reference size, and  $-m$  is the slope of the distribution when  $\log N$  is plotted versus  $\log x$ .

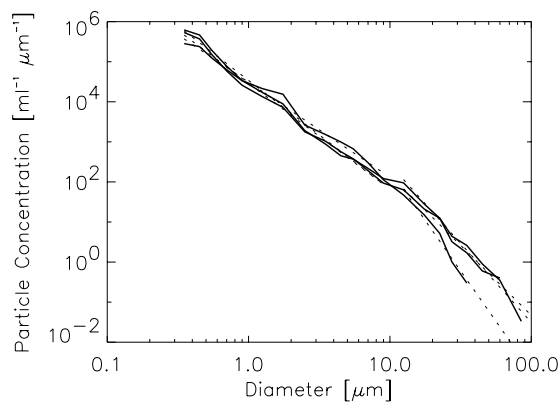
The *number* size distribution  $F(x)$  [ $\text{m}^{-3} \mu\text{m}^{-1}$ ] is defined such that  $F(x)dx$  is the number of particles per unit volume in the size interval from  $x$  to  $x + dx$ .



The number distribution is related to the cumulative distribution by  $F(x) \equiv |dN/dx|$ . For the Junge distribution, this leads to:

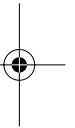
$$F(x) = kmx_o^m x^{-m-1} \equiv Kx^{-s} [\text{m}^{-3} \mu\text{m}^{-1}]. \quad (2.34)$$

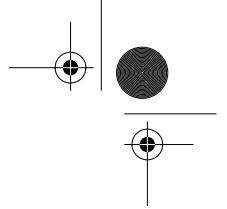
In this study, the number size distribution was measured with a laser single particle counter (L-SPC)<sup>1)</sup> which enables the determination of 23 different size classes between 0.3 and 150  $\mu\text{m}$ . The water samples were first diluted to allow the measurements of the scattering of a single particle with a laser beam. Then this measured signal was compared with the signal produced by spherical size standards with known diameter allowing the determination of the size. Since algae are not spherical in general, the determined diameters do not have to match the actual size. Consequently, the calculations of scattering properties based on Mie theory were only performed for spherical particles (Chapter 2.10).



**Figure 2.4** Typical particle size distribution  $F(D)$  of Lake Zürich water. Below and above 10  $\mu\text{m}$  two segments with different distributions can be distinguished (solid: measured, dotted: fitted).

<sup>1)</sup> The measurements were performed by D. Kobler, EAWAG, Dübendorf. The L-SPC system is a development by the EAWAG. It consists of an dilution system (6 - 60 times) and two linearly connected laser sensors (PARTICLE MEASURING SYSTEMS INC.).





## 2.5 Particle Size Distribution

25

The typical particle size distributions of Lake Zürich and Lake Zug water show below and above a diameter of around  $10 \mu\text{m}$  two segments with different distributions (Fig. 2.4). Consequently, the fit parameter  $K$  and  $s$  defined in Eq. 2.34 were determined separately for both segments (Tab. 2.2)

**Table 2.2** Mean value and standard deviation of the fit parameters to the Junge distribution for the two segments based on measurements in Lake Zug, Lake Zürich and Walensee (number of samples  $n = 63$ ).

Segment	$s$	$K$
$<10 \mu\text{m}$	$2.3 \pm 0.3$	$4.0 \cdot 10^4 \pm 3.7 \cdot 10^4$
$>10 \mu\text{m}$	$4.0 \pm 0.6$	$1.9 \cdot 10^7 \pm 4.6 \cdot 10^7$

Gaedke (1992) shows for Lake Constance that the seasonal variability of the particle size distribution within a lake is correlated with biological activities. In springtime, little round fast growing algae are frequently encountered which are followed by zooplankton and large algae in the summer. However, such a sequence could not be found in Lake Zürich (Fig. 2.5). Accordingly, no dependence between particle classes and chlorophyll  $a$  could be shown. These results indicate that the particle concentration is significantly influenced by inorganic matter. Since the reflectance is approximately proportional to the backscattering (Eq. 2.21) which is itself correlated to the amount of particulate matter, it can be expected that the reflectance is only weakly dependent on  $CHL$ .



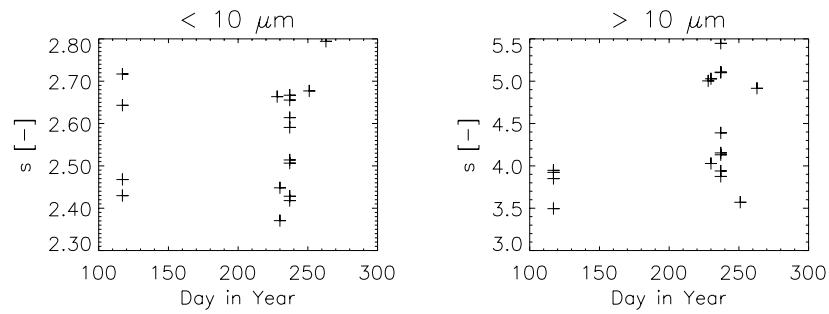
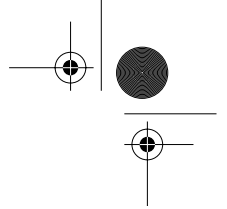


**Figure 2.5** Seasonal variability of the fit parameters  $s$  of the particle size distribution  $F(D)$  for the two segments (Lake Zürich, right below the surface). The parameter  $s$  does not show any seasonal variation and any dependence on biological activities.

## 2.6 Absorption

Absorption consists of various sources: pure water, gelbstoff, and photosynthetically active pigments, and sometimes also detritus and inorganic particles.

### *Water*

Although water absorption is usually assumed to be known exactly, the values found in the literature differ significantly due to different determination methods. In this study, water absorption below 700 nm is taken from Pope and Fry (1997) who also give an overview about differing literature values. Above 700 nm, values from Palmer and Williams (1974) were used.

Fig. 2.6 shows that water absorption has a minimum around 450 nm. This is remarkable, because the sun has its energy maximum at 520 nm. It can be expected that life on earth would have evolved entirely different without this relation. Since the absorption coefficient of water is high above 750 nm, the water-leaving radiance becomes negligible and in general cannot be used for the determination of water constituents. This does not apply for waters with high particulate matter concentrations which lead to observable signals in the near-infrared as well.

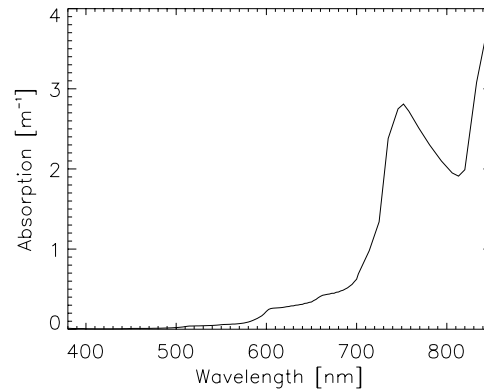


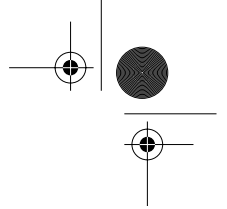
**Figure 2.6** The absorption coefficient of water is high in the near-infrared (> 700 nm), leading to low water leaving radiance (below 700 nm: Pope and Fry, 1997; above 700 nm: Palmer and Williams, 1974).

### *Gelbstoff*

The absorption of gelbstoff  $a_g$  is usually parameterized with an exponential function (Bricaud et al., 1981):

$$a_g(\lambda) = a_g(\lambda_0)e^{-S(\lambda-\lambda_0)} \text{ [m}^{-1}\text{]}. \quad (2.35)$$

Normally, a reference wavelength  $\lambda_0$  of 440 nm or 450 nm is chosen corresponding to the first absorption maximum of chlorophyll  $a$ . The constant  $S$  has been determined in various studies (Tab. 2.3).

**Table 2.3** Summary of several studies determining  $S$ .

Author(s)	$S$ [ $\text{nm}^{-1}$ ]	Comments
Bricaud et al. (1981)	$0.0140 \pm 0.0032$	105 water samples of the Atlantic, Baltic Sea and Mediterranean
Davies-Colley and Vant (1987)	$0.0187 \pm 0.0028$	12 freshwater lakes
Roesler and Perry (1989)	$0.016 \pm 0.002$	evaluation of 16 publications
Gege (1999)	$0.0142 \pm 0.0012$	Lake Constance

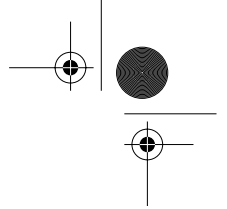
Since the model parameters can be highly variable for different water types, new measurements were performed for Lake Zürich in summer 1998. Water samples were taken from just below the water surface and at 2.5 m water depth and filtered with  $0.4 \mu\text{m}$  filters (MILLIPORE, type HTTP). Afterwards, the transmission of the filtrate was measured with a UVICON 930 double-beam spectroradiometer (KONTRON INSTRUMENTS) using 10 cm path length quartz cells<sup>1)</sup>. Wavelength scans were performed from 300 to 800 nm (except for the first few measurements, where only scans above 350 nm were performed). For the correction of the influence of the glass cuvette and the water absorption, the transmission of nanopure water was also determined and subtracted from the lake water measurements.

Despite this correction, noisy data, an offset (i.e., negative values), and a step at 400 nm and 500 nm at the transition zone between different spectrometer lamps occurred (Fig. 2.7). It was presumed to be a result of unstable current supply or lamp properties, of scattering by suspended matter, or of offsets produced by air bubbles created during the filtration process and cells filling as reported by Gege (1999). Unfortunately, all these processes cause wavelength dependent errors. Since the offsets might be caused by unstable current supply or lamp properties, wavelength dependent corrections for scattering effects could not be applied<sup>2)</sup>.

Our additional correction was based on two assumptions: First, a wavelength in the red region of the spectrum can be specified where the absorption is zero, and secondly, the exponent  $S$  that describes the absorption

1) In case of high particulate matter concentration, the filtrate is filtered a second time with smaller filters ( $0.2 \mu\text{m}$ ) to inhibit influences by scattering. For the same reason, shorter quartz cuvettes were used.

2) Davies-Colley and Vant (1987) propose a correction for scattering effects. The algorithm includes wavelength dependent scattering assuming that gelbstoff absorption is zero at long wavelengths (e.g., 740 nm).



below 400 nm is also valid between 400 nm and 500 nm. This resulted in the following correction algorithm:

- *Smoothing* of the data using a median filter.
- *Offset correction*. The absorption of gelbstoff at 773 nm was set to zero. This particular wavelength had been chosen, since here the water absorption can be assumed to be temperature independent, and the gelbstoff absorption is negligible even for high gelbstoff concentrations (Gege, 1999)<sup>1)</sup>.
- *Determination of the exponent  $S$  for the region below 400 nm*. The fitting parameter  $S$  was usually in the same region as the values found in the literature (Tab. 2.3). The mean value of all measurements was  $S = 0.0171 \pm 0.0050 \text{ nm}^{-1}$  (number of data points  $n = 28$ ). Since a wavelength dependent correction of the absorption was not included, the real coefficient is presumed to be lower than the determined one.
- *Cutting out the region below 500 nm*, and replacing it with extrapolated values using  $S$  attached at 500 nm.

The corrected absorption coefficients look reasonable (Fig. 2.7). At 450 nm, the absolute values range from 0.05 to 0.2  $\text{m}^{-1}$ . These values are rather low compared to high eutrophic lakes where values up to 2.5  $\text{m}^{-1}$  can be measured (e.g., Dutch lakes as reported by Dekker, 1993). Since the changes due to the correction were significant, uncertainties are expected to be in the order of 0.03  $\text{m}^{-1}$ .

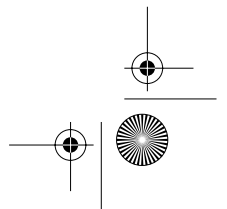
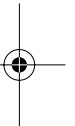
As dissolved organic carbon *DOC* represents the most important proportion of gelbstoff, Davies-Colley and Vant (1987) presume that  $a_g(\lambda_0)$  should be proportional to *DOC*:

$$a_g(\lambda_0) = \text{DOC} \times a_g^*(\lambda_0) \quad [\text{m}^{-1}]. \quad (2.36)$$

In this study, this assumption was tested. The dissolved organic carbon *DOC* was measured photometrically after UV-oxidation<sup>2)</sup>. The best fits were obtained with  $a_g^*(\lambda_0) = 0.048 \pm 0.019 \text{ l mg}^{-1} \text{ m}^{-1}$  ( $n = 28$ ), but the relation was only weak as shown in Fig. 2.8. This can be caused by an erroneous correction or by the low *DOC* gradients that complicates the determination of appropriate regression coefficients. The standard deviation suggested that the gelbstoff absorption could be approximated merely with an error of about 30%. However, if no absorption measurements are available, Eq. 2.36 gives a

<sup>1)</sup> Gege (1999) suggests a temperature correction of the absorption measurements. However, these effects are negligible below 600 nm and therefore not considered in this study.

<sup>2)</sup> The *DOC* measurements were performed by the Wasserversorgung Zürich (U. Bosshart) and EAWAG, Dübendorf (S. Meyns).



practical way of approximating the gelbstoff absorption – bearing in mind that *DOC* is often measured for water management purposes anyway.

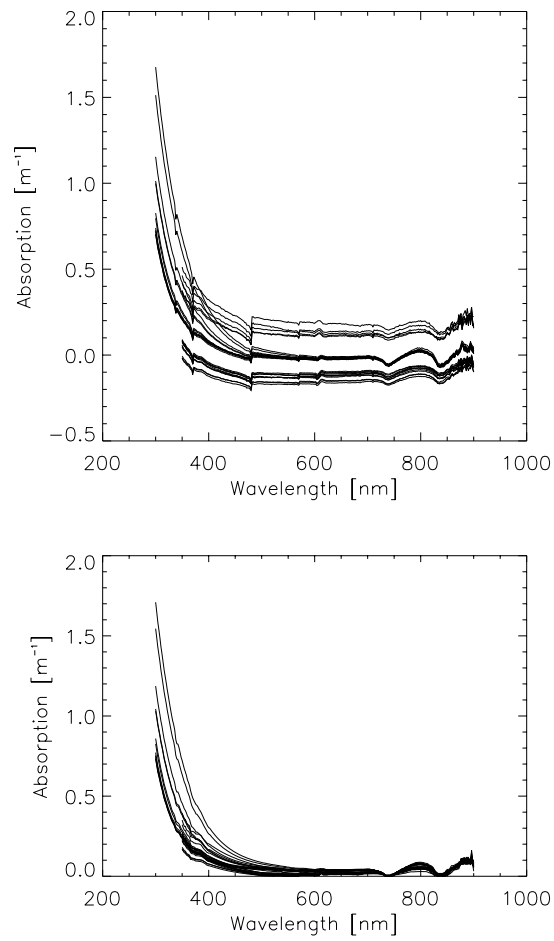


**Figure 2.7** Gelbstoff absorption measurements in Lake Zürich: raw data (top) and corrected values (bottom). The correction procedure is explained in the text.

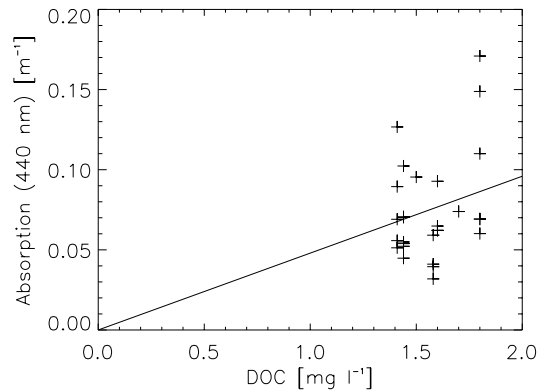


**Figure 2.8** The gelbstoff absorption at 440 nm as a function of *DOC* (Lake Zürich).

#### *Phytoplankton Pigments*

Each algae class has its own characteristic set of pigments with different optical properties (Tab. 2.4). The most relevant pigments for water optics are chlorophylls, phaeophytin, phycobiliproteins (phycocyanin, phycoerythrin), and carotenoids:

- The most important pigment is *chlorophyll a* which has absorption maxima near 440 nm and 670 nm. It can be found in all photosynthetic active organisms<sup>1)</sup> and is therefore a good indicator for the biological activities in a lake. Chlorophyll *b* and *c* also absorb light but only chlorophyll *a* is involved in the primary processes of the photosynthesis leading to the building of energetic molecules.
- The chemical structure<sup>2)</sup> and the absorption property of *phaeophytin* are almost identical to chlorophyll. In general, they are results of the decomposition of chlorophyll and part of the photosynthesis in cells.

<sup>1)</sup> The only exceptions are photosynthetic active bacteria which use bacteriochlorophyll.

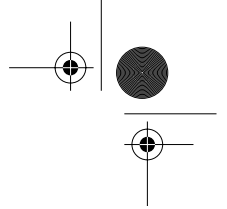
<sup>2)</sup> Chlorophylls are conjugated circular macromolecules. A magnesium atom is responsible for the coordination of the circle. Phaeophytin has the same structure, except that the magnesium atom is missing.

**Table 2.4** Phytoplankton pigments in various algae classes. ++: important pigment, +: pigment occurs, -: pigment is infrequent or occurs only in low concentrations (van den Hoek, 1984).

	Cyanophyceae	Rhodophyceae	Chrysochyceae	Xanthophyceae	Bacillariophyceae	Chloromonadophyceae	Cryptophyceae	Dinophyceae	Chlorophyceae
Chlorophyll <i>a</i>	++	++	++	++	++	++	++	++	++
Chlorophyll <i>b</i>									++
Chlorophyll <i>c</i>			++	++	++	++	++	++	
Phycocyanin	++	++					++		
Phycoerythrin	++	++					++		
$\alpha$ -Carotin		-			-		++		-
$\beta$ -Carotin	++	++	++	++	++	++	-	++	++
Diadinoxanthin			+	++	++	++		+	
Diatoxanthin		+	++	++	-	+	+	+	
Fucoxanthin			++		++			-	
Lutein		++							++

- Red and blue algae, as well as cryptophyceae contain *phycobiliproteins*. Unlike chlorophyll, these pigments absorb between 540-650 nm. This is the reason, why these algae can survive in deep waters, where the blue and red part of the light is absorbed by algae living in the upper zones or by water. The efficiency of the energy transfer is nearly 100%. *Phycoerythrin* and *phycocyanin* belong to this group. Phycobiliproteins have characteristic fluorescence spectra, which can be used for active remote-sensing (Exton et al., 1983).
- *Carotenoids* are contained in all phytoplankton species, where they protect the photosynthetic centre by transferring unusable energy away from chlorophyll. They also sample light energy in the range 400-500 nm, but the efficiency is only 30-40%. *Carotins* and *xanthophylls* belong to this group.

The absorption maxima of a specific pigment can vary *in vivo* up to 5 nm, the absorption strength less than 50% (Gege, 1994). This is caused by two



factors:

- Chlorophylls have different tasks in a cell, and are consequently active in different environments.
- The absorption signature becomes flatter if the pigments are spatially concentrated (Duysens, 1956). This packaging effect is caused by the fact that light is absorbed completely if the pigment concentration exceeds a certain level, whereas the pigment is still transparent at other wavelengths. Thus an increase of the pigment concentration barely affects the spectra at the absorption maxima, but changes the spectra in the other part more distinctly – the signature is flattened.

The absorption spectra of phytoplankton are always strongly related to chlorophyll *a* absorption, since this pigment is needed for the photosynthesis and occurs in all algae. Thus, according to Beer's law (Eq. 2.15), the specific absorption coefficient  $a_p^*(\lambda)$  is usually defined by normalizing the algae absorption spectra  $a_p$  with chlorophyll *a* (*CHL*):

$$a_p^*(\lambda) = \frac{a_p(\lambda)}{CHL} \text{ [m}^{-1}\text{]}. \quad (2.37)$$

The asterisk (\*) indicates the specific absorption coefficient. Due to the packaging effect outlined above, Eq. 2.37 is only valid for low pigment concentrations which usually prevail in Swiss lakes. Additional errors are introduced, if the ratio between *CHL*, phaeophytin and other pigments is not constant.

In this work, all chlorophyll *a* measurements were performed with the HPLC method (Meyns et al., 1994)<sup>1)</sup>. Typical annual variations of *CHL* in Lake Zürich and Walensee are shown in Fig. 2.9.

<sup>1)</sup> The chlorophyll *a* measurements were performed by *Wasserversorgung Zürich* (U. Bosshart) and *EA-WAG*, Dübendorf (S. Meyns).

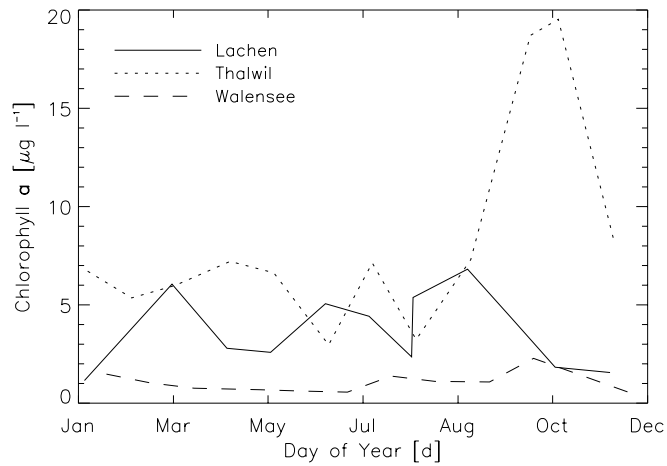


**Figure 2.9** Annual variation of chlorophyll *a* just below the surface in Lake Zürich (Lachen and Thalwil) and in Lake Walensee (data from 1998). Except in October/November at the station Thalwil, only variations in the order of a few micrograms per litre occur.

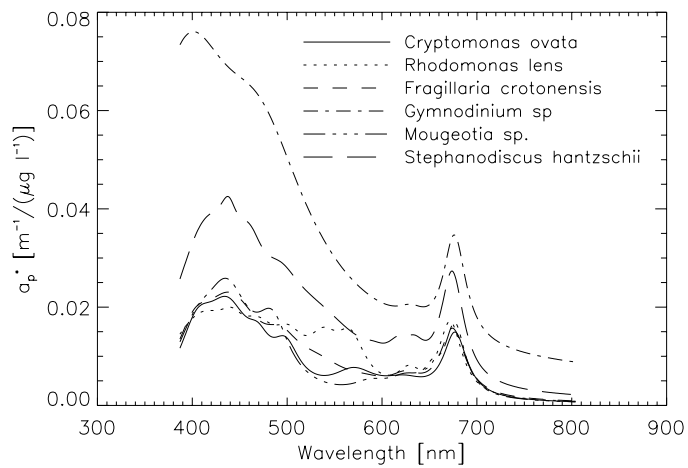


**Figure 2.10** Specific absorption spectra of typical algae species of Lake Constance (Gege, 1994). The differences are caused by varying internal and external structures as well as varying pigment sorts and concentrations.

In this study, no own absorption measurements were made<sup>1)</sup>, and literature values of Lake Constance are used instead (Fig. 2.10). Varying pigment sorts, shapes, and internal structures lead to different specific absorption spectra for different algae. The specific phytoplankton absorption can be simulated using the empirical model as shown in Lee et al. (1998):

$$a_p^*(\lambda) = \{c_0(\lambda) + c_1(\lambda) \ln[ a_p^*(440\text{nm}) / a_{p,0}^* ]\} \times a_p^*(440\text{nm}), \quad (2.38)$$

where  $a_{p,0}^* = 1 \text{ m}^{-1}/(\mu\text{g l}^{-1})$ ,  $c_0$  and  $c_1$  are determined by fitting Eq. 2.38 to measured spectra. The advantage of this model is that the entire spectra can be approximated with only one free parameter:  $a_p^*(440\text{nm})$ . Tab. 2.5 shows the typical variation range of this parameter for various algae species.

**Table 2.5**  $a_p^*(440 \text{ nm})$  for the algae species shown in Fig. 2.10.

Algae Species	$a_p^*(440 \text{ nm})$ [ $\text{m}^{-1}/(\mu\text{g l}^{-1})$ ]
<i>Cryptomonas ovata</i>	0.0218
<i>Rhodomonas lens</i>	0.0200
<i>Fragillaria crotonensis</i>	0.0230
<i>Gymnodinium sp.</i>	0.0685
<i>Mougeotia sp.</i>	0.0254
<i>Stephanodiscus hantzschii</i>	0.0421

The parameters  $c_0$  and  $c_1$  were determined for the algae species of Lake Constance illustrated in Fig. 2.10. In order to obtain only positive values for  $c_1$ , – which cannot be expected if a simple regression is used – the fitting parameters were calculated in the following way:

$$c_0(\lambda) = \max \left[ \frac{a_{p, \text{species}}^*(\lambda)}{a_{p, \text{species}}^*(440\text{nm})} \right] \quad [-] \quad (2.39)$$

and

<sup>1)</sup> The measurements of phytoplankton absorption is often prone to errors and depend on the measurement set-ups. See Pegau et al. (1995) for more details about such measurements.

$$c_I(\lambda) = \text{average} \left[ \frac{a_{p, \text{species}}^*(\lambda) / a_{p, \text{species}}^*(440\text{nm}) - c_0(\lambda)}{\ln[ a_p^*(440\text{nm}) / a_{p, 0}^* ]} \right] \quad [-] \quad (2.40)$$

The object of this algorithm is to establish continuous spectra for  $c_0(\lambda)$  and  $c_1(\lambda)$  with only positive values. Since the input algae spectra of the different species differed strongly, the signature is less uniform than in Lee et al. (1998) (Fig. 2.11). Nevertheless, the specific absorption could be modelled in an accurate way even for single species (Fig. 2.11). The best agreements were found at both absorption maxima; the highest relative errors occur between 500 nm and 600 nm caused by differing pigments in each species, and low value magnitudes.

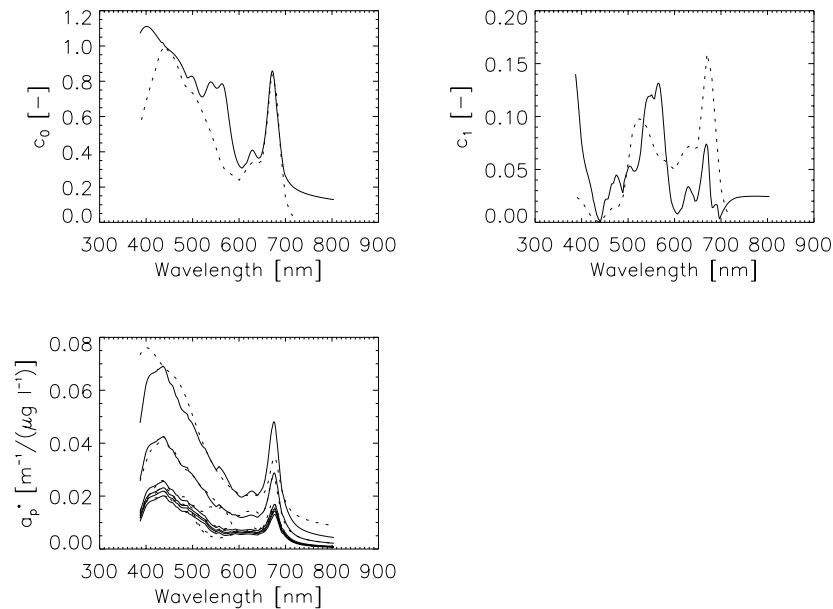
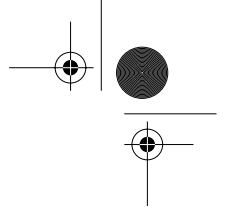


**Figure 2.11** Upper two graphs: fitting parameters of Eq. 2.38 to six algae spectra of Lake Constance (solid) compared with the values obtained by Lee et al. (1998) (dotted). Lower graph: modelled spectra using derived parameters (solid) and measured spectra (dotted).



### *Detritus and Inorganic Particles*

Particulate matter can be divided into living organic material (mainly phytoplankton), non-living organic particles (detritus) and inorganic material. The absorption of phytoplankton has been discussed above. The sum of dead organic and inorganic components is referred to as *tripton*. Inorganic particles are usually assumed to be non-absorbing (Dekker, 1993).

Detritus has an exponential absorption similar to gelbstoff (Dekker, 1993). The discrimination between phytoplankton, detritus, and inorganic material is generally non-trivial. Bricaud and Stramsky (1990) give a review on the discrimination of these fractions.

## 2.7 Scattering

The scattering is considered to consist of two different contributions: pure water, and particulate matter. Since the operational models are based on the backscattering coefficient, the main emphasis is put on this parameter.

### *Water*

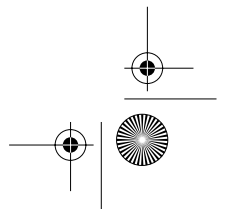
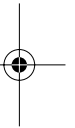
The scattering of light in water can be described almost perfectly with Rayleigh theory which is valid if the wavelength is much larger than the scatterer – in this case the water molecule. According to this theory, the coefficients have a strong wavelength dependence and the total light scattering caused by water  $b_w$  can be calculated as follows (Morel, 1974):

$$b_w(\lambda) = b_w(\lambda_0) \left( \frac{\lambda}{\lambda_0} \right)^{-4.32}, \quad (2.41)$$

with  $b_w(\lambda_0) = 0.0028 \text{ m}^{-1}$  for  $\lambda_0 = 500 \text{ nm}$ . The wavelength dependence of  $\lambda^{-4.32}$  rather than  $\lambda^{-4}$  – as expected for perfect Rayleigh scattering – results from the wavelength dependence of the index of refraction. Since the phase function of water is symmetrical, the forward  $b_{f,w}$  and backward scattering  $b_{b,w}$  are both  $0.5 \cdot b_w$ .

### *Particulate Matter*

Most estimates on scattering properties are derived from the marine environment (EC, 1999). Angular scattering measurements in the laboratory are even more difficult to perform than absorption measurements. Carefully made and widely cited - but of course not perfect - scattering measurements are found in Petzold (1972), which are shown in Fig. 2.12.



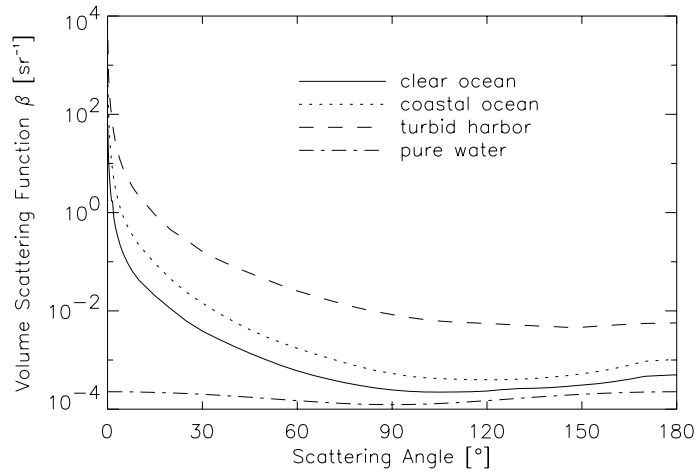
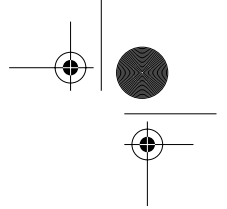


**Figure 2.12** Volume scattering function of natural water measured by Petzold (1972) and of pure water (Morel, 1974). Since the scatterer and the wavelength are the same characteristic size, the phase function is strongly peaked in forward direction ( $\lambda = 514$  nm with a FWHM of 75 nm).

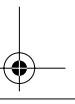
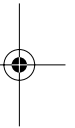
Scattering strongly depends on the particle size distribution function (Baker and Lavell, 1984). The higher the abundance of little particles, the stronger the backscattering due to the larger total cross section.

Particulate matter can be separated into organic and inorganic matter. The scattering of the *organic* matter is assumed to correlate with *CHL*:

$$b_{b,org}(\lambda) = CHL \times b_{b,org}^*(\lambda_0) \left( \frac{\lambda_0}{\lambda} \right)^m \quad [m^{-1}]. \quad (2.42)$$

Gege (1995) shows that for algae smaller than  $5 \mu m$  in diameter, a moderate wavelength dependence can be expected (i.e.  $m = 1$ ), and that for larger algae, this dependence can be neglected (i.e.  $m = 0$ ).

According to Sathyendranath et al. (1989), the phytoplankton scattering coefficient can also be estimated with:



$$\begin{aligned}
 b_{b,org}(\lambda) &= \frac{b_{b,org}(550) \cdot a_p(550)}{a_p(\lambda)} \quad (2.43) \\
 &= CHL \cdot \frac{b_{b,org}^*(550) \cdot a_p(550)}{a_p(\lambda)} \\
 &= CHL \cdot b_{b,org}^*(\lambda)
 \end{aligned}$$

However, Eq. 2.43 is only valid close to the reference wavelength at 550 nm but not below 400 nm and above 700 nm where  $a_p(\lambda)$  can assumed to be equal to zero. For wavelengths at which particles are strongly absorbing, the scattering is reduced<sup>1)</sup> such that the total attenuation is only weakly dependent on wavelength (Gordon et al., 1988). Although this dependence is not included in Eq. 2.42, the scattering effect is generally sufficiently approximated.

At low pigment concentrations, most of the particle backscattering results from scattering by phytoplankton detrital material (e.g., fragments of broken cells). The ratio of viable phytoplankton to detrital particles increases with the phytoplankton concentration and consequently, the particle backscattering probability decreases.

By definition, *inorganic* particulate matter does not correlate with *CHL*<sup>2)</sup>. The size of particles ranges from  $10^{-8}$  m to  $10^{-6}$  m and is therefore smaller than most organic particulate matter. The wavelength dependence of  $b_{b,inorg}$  can be described similar to water or algae:

$$b_{b,inorg}(\lambda) = b_{b,0} \left( \frac{\lambda_0}{\lambda} \right)^m \text{ [m}^{-1}\text{]}, \quad (2.44)$$

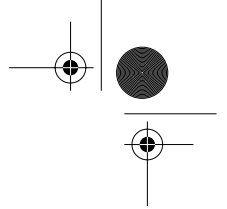
with  $b_{b,0} \equiv b_{b,inorg}(\lambda_0)$  at the reference wavelength  $\lambda_0 = 550$  nm. Because of their small size, a weak wavelength dependence can be assumed:  $0 \leq m \leq 1$ .

## 2.8 Bio-Optical Model

For the analysis performed in this study, it is worthwhile to define a bio-optical model which summarizes the influence of all optically relevant parameters. The absorption model is given by:

<sup>1)</sup> See Chapter 2.10.

<sup>2)</sup> Of course, organic material can not correlate with chlorophyll. However, the term "organic" has been used as algae are the most important portion of the organic particles.



$$a(\lambda) = a_w(\lambda) + a_d(\lambda) + a_g(\lambda) + CHL \cdot a_p^*(\lambda). \quad (2.45)$$

The following model is used for scattering:

$$b_b(\lambda) = b_{b,w}(\lambda) + CHL \cdot b_{b,org}^*(\lambda) + b_{b,0} \cdot b_{b,inorg}^*(\lambda). \quad (2.46)$$

The equations for organic (Eq. 2.42) and inorganic (Eq. 2.44) scattering are generalized and no explicit wavelength dependence is given.

## 2.9 Complex Index of Refraction

The complex index of refraction  $m(\lambda)$  concisely describes the effects of electromagnetic wave propagation, i.e. scattering and absorption by particles or refraction at medium interfaces:

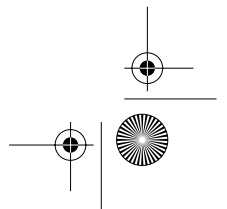
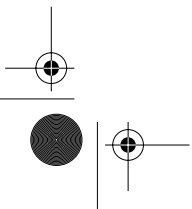
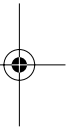
$$m(\lambda) = n(\lambda) + i n'(\lambda) [-], \quad (2.47)$$

where the real part  $n(\lambda)$  refers to the scattering property and the imaginary part  $n'(\lambda)$  to the absorption property.

In order to describe the geometrical optical properties of water,  $n(\lambda)$  is of special interest. The relative<sup>1)</sup> index of refraction of water  $n_w$  depends on temperature, salinity and wavelength. Quan and Fry (1995) give an approximation which is shown in Fig. 2.13 for different temperatures. The temperature dependency can usually be neglected without major errors. In general, a value of 1.34 is taken for all wavelengths which leads to a maximum error of approximately 2%. The dependence on salinity is only important for ocean water but not for fresh waters. In this study, we always used the approximation given by Quan and Fry to avoid additional uncertainties.

The  $n$  distribution of particles found in natural waters is often bimodal. Living phytoplankton typically have relative indices in the range of 1.01 to 1.09. Detritus and inorganic particles generally have higher indices, namely in the range of 1.15 to 1.20 relative to water (Jerlov, 1976). Typical values are 1.05 for algae and 1.16 for inorganic particles.

<sup>1)</sup> Indices of refraction are always relative quantities; in this case, relative to air.



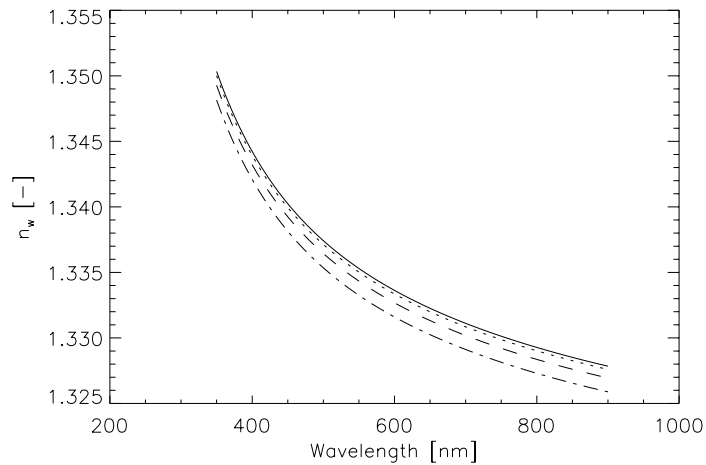
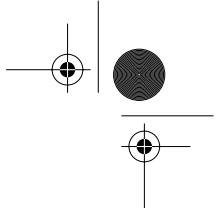


**Figure 2.13** Real part of the refractive index of water for 0° (top curve), 10°, 20°, and 30° Celsius, respectively.

## 2.10 Mie Scattering

Direct measurements of the phase function are difficult to carry out, as the required angular resolution is diminished due to the strong forward direction of light scattering (Mobley, 1994). Theoretically, all scattering parameters can be calculated using Mie theory (Mie, 1908) which provides all relevant parameters for the description of scattering phenomena. The solution is exact and valid for all sizes of spheres, indices of refraction, and wavelengths. However, if the particle size is much smaller than the wavelength, then the scattering is more easily described by Rayleigh theory; if the particle size is much larger than the wavelength, then the scattering is best described by geometrical optics. Thus the use of Mie theory is usually constrained to the description of scattering phenomena if particle size and wavelength are in the same order.

Light propagation can be characterized by the Stokes vector:



$$\begin{bmatrix} L_1 \\ L_2 \\ L_3 \\ L_4 \end{bmatrix}, \quad (2.48)$$

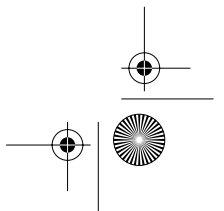
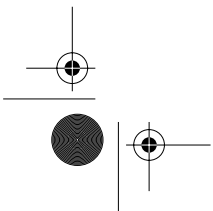
where  $L_1$  is the total radiance,  $L_2$  and  $L_3$  describe the linear polarization state of the radiance, and  $L_4$  is related to the state of circular polarization. All four Stokes parameters have units of radiance, and each is a function of position, time, direction, and wavelength.

If a light beam interacts with any medium or interface (e.g. a particle), the amplitudes of the Stokes parameters change. The amplitude scattering matrix describes this transformation:

$$\begin{bmatrix} L_1^s \\ L_2^s \\ L_3^s \\ L_4^s \end{bmatrix} = \frac{1}{k^2 r^2} \begin{bmatrix} S_{11} & S_{12} & 0 & 0 \\ S_{12} & S_{11} & 0 & 0 \\ 0 & 0 & S_{33} & S_{34} \\ 0 & 0 & -S_{34} & S_{33} \end{bmatrix} \begin{bmatrix} L_1^i \\ L_2^i \\ L_3^i \\ L_4^i \end{bmatrix}, \quad (2.49)$$

where the superscripts  $s$  and  $i$  indicate the scattered components and the incident components, respectively. All terms are a function of wavelength and scattering angle. Mie theory calculates the elements of this scattering matrix. The collimated light beam is described as an electromagnetic plane wave, and the sphere is treated as a dielectric body. Maxwell's equations are then solved including the boundary conditions at the surface of the sphere. Details of the theory can be found in van de Hulst (1957) and in Bohren and Huffman (1983).

Relevant parameters are size, shape, internal structure and relative complex refractive index of the particle, and the wavelength. The relevant parameter describing the size of the sphere is its diameter  $D$  relative to the wavelength of the light in the medium:



$$\alpha \equiv \frac{\pi D}{\lambda_w} = \frac{\pi D n_w}{\lambda_{Vacuum}}, \quad (2.50)$$

where  $\alpha$  is the size parameter,  $\lambda_w$  the wavelength of the monochromatic light in the surrounding medium,  $n_w$  the refractive index of the medium, and  $\lambda_{Vacuum}$  the wavelength in vacuum.

Beside the scattering matrix, the Mie calculations also yield the efficiency factors. The scattering efficiency  $Q_b$ , for example, is the scattered fraction of radiant energy incident to the sphere. Accordingly, the total absorption efficiency  $Q_a$  is the fraction of incident energy that is absorbed by the sphere. Fig. 2.14 shows the strong dependence of  $Q_b$  on the size parameter  $\alpha$  and the relative complex part of the refractive index  $n$  assuming no absorption.

The bulk scattering coefficient  $b$  within a volume  $V$  is calculated by adding up the contributions of all particles characterized by their diameter  $D$  (Mobley, 1994):

$$b = \int_0^{\infty} F(D) s(D) Q_b(D) dD \quad [\text{m}^{-1}]. \quad (2.51)$$

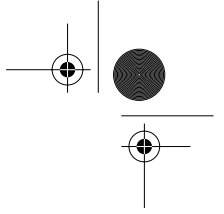
For a spherical particle, the geometrical cross section  $s$  is given by  $\pi D^2/4$ . The size distribution  $F(D)$  is defined in Eq. 2.34. The absorption coefficient  $a$  and the beam attenuation  $c$  are defined likewise.

Van de Hulst (1957) gives various approximations for the determination of the absorptions and total scattering efficiency factors. However, for the backscattering coefficient, we had to perform exact Mie calculations since no such approximation exists. In order to calculate the backscattering coefficient, the wavelength dependent phase function (Eq. 2.13) has to be determined and integrated from  $\pi/2$  to  $\pi$  (Eq. 2.12). If the amplitude scattering matrix is known, the phase function is calculated for unpolarized light by (Bohren and Huffman, 1983):

$$\tilde{\beta} = \frac{S_{11}}{Q_b(D) s(D) k^2} \quad [-], \quad (2.52)$$

where  $k$  [ $\text{m}^{-1}$ ] is the wavenumber, and  $S_{11}$  [-] the first element of the amplitude scattering matrix given in Eq. 2.49.

The cell matter absorption  $a_{cm}$  [ $\text{m}^{-1}$ ] can be easily related to the bulk absorption  $a$  if all particles contain the same pigment concentration. In case of spherical particles, this is equal to:



$$a_{cm}(\lambda) = \frac{a(\lambda)}{\frac{\pi}{6} \int_0^{\infty} F(D) D^3 dD} \quad [\text{m}^{-1}], \quad (2.53)$$

where  $a_{cm}$  is related to the imaginary part of the index of refraction  $n'$  by (Kerker, 1969):

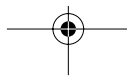
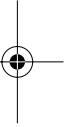
$$a_{cm}(\lambda) = \frac{4\pi n'(\lambda)}{\lambda} \quad [\text{m}^{-1}]. \quad (2.54)$$

As the same molecule parameters give rise to absorption and scattering,  $n$  can be related to  $n'$  using the Kramers-Kronig relation (Gege, 1994):

$$n(\lambda) = n(\lambda_0) + \frac{2}{\pi} (\lambda_0^2 - \lambda^2) \text{P} \int_0^{\infty} \frac{\lambda' n'(\lambda')}{(\lambda^2 - \lambda'^2)(\lambda_0^2 - \lambda'^2)} d\lambda'. \quad (2.55)$$

The letter “P” before the integral indicates that the contribution at the poles within the integral is not included (*principal value*). This equation allows the determination of the spectral signature of  $n(\lambda)$  with known  $n'$  determined by Eq. 2.53 and Eq. 2.54 and with an assumption made for  $n(\lambda_0)$ .

The calculations were performed with the software module PAR (Appendix B.3). All calculations were made for spherical particles (see comments in Chapter 2.5). First, the scattering efficiency as a function of the size parameter  $\alpha$  was determined. The oscillation shown in Fig. 2.14 is a typical property of Mie scattering. It results from interferences between the portion of the wave front passing nearby the sphere and the portion transmitting through it. This resonance also explains why it is hard to predict the scattering behaviour if particle and wavelength are the same size. The higher  $n$ , the shorter the periods of the oscillation. For  $\alpha \rightarrow \infty$  the scattering coefficient approximates 2.



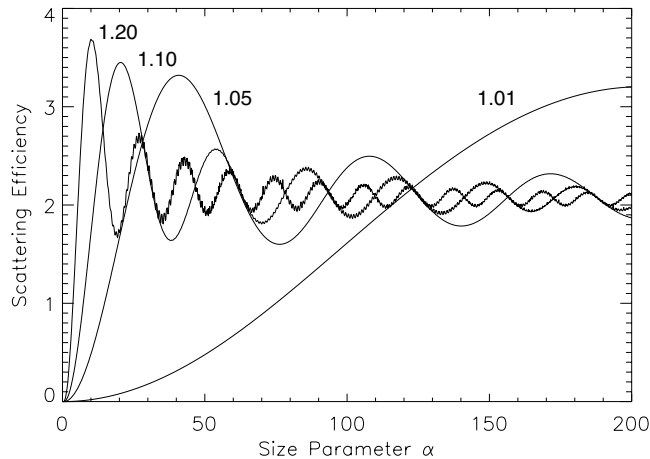
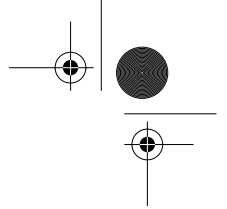


**Figure 2.14** The scattering efficiency  $Q_b$  as a function of the size parameter  $\alpha$  (Eq. 2.50) and the real part of the refractive index  $n$ . The larger  $n$ , the shorter the periods and the faster  $Q_b$  converges to 2 (the calculations are made for  $n' = 0$  and  $n = 1.01, 1.05, 1.10, 1.20$ ).

Fig. 2.15 shows the contributions of different diameter classes to the scattering coefficients assuming no absorption. The maximum of the *total scattering coefficient*  $b$  at  $10 \mu\text{m}$  is a consequence of the maximum of  $Q_b$  for this diameter. The maximum moves to lower diameter values for higher refractive indices (see also Fig. 2.14). Thus the higher the refractive index, the more important become the little particles and the higher are the scattering coefficients (Fig. 2.16). Note that dead organic material usually exhibits high refractive indices (Chapter 2.9); this is another explanation of the important role of detritus for scattering.

The larger the wavelength compared to the particle size, the less pronounced the forward scattering. Consequently, small particles become relatively more important for backscattering than for total scattering ( $b/b_b$  ratio shown in Fig. 2.15). The influence of the wavelength was only weak compared to the influence of the particle diameter (Fig. 2.17); this corresponds to Eq. 2.42 and Eq. 2.44.

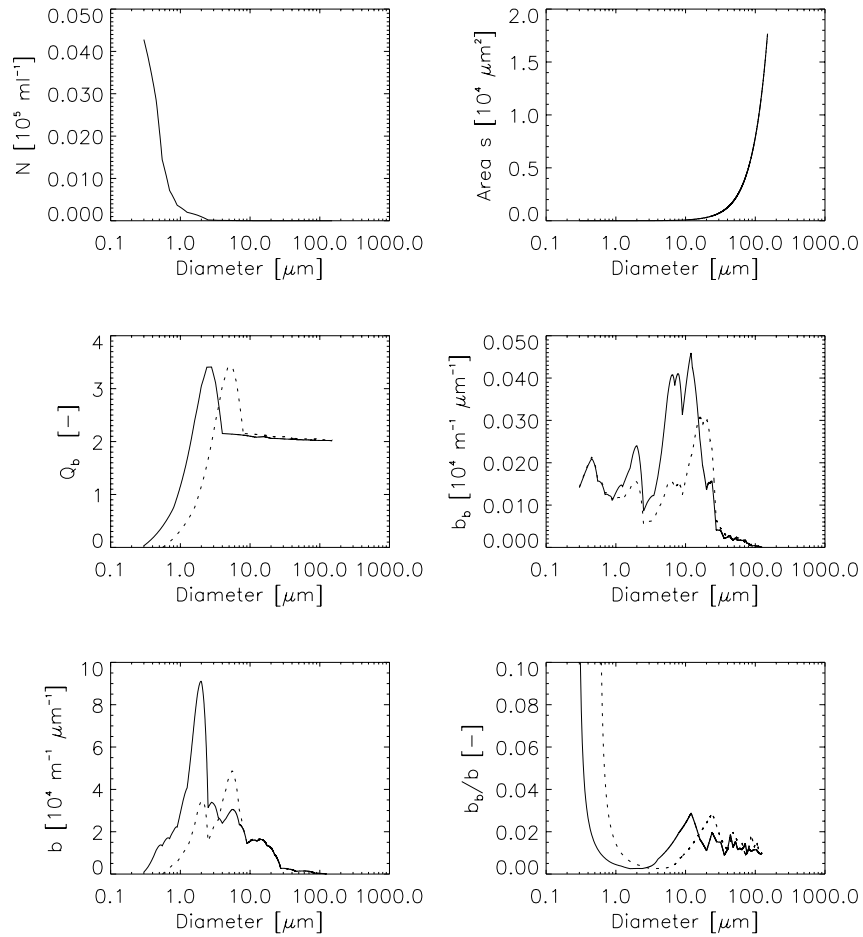


**Figure 2.15** The scattering coefficients are a function of the cumulative size distribution  $N$  (top left, data from Lake Zürich), the geometrical cross section of the particles (top right), and the efficiency coefficients  $Q_b$  (centre left) all of which depend on the particle diameter. The calculations were performed for refractive index  $n_p = 1.1$ . The product of these parameters determines the pertinence of the different diameter classes to the backscattering coefficient  $b_b$  (centre right) and the scattering coefficient  $b$  (bottom left). Note that the scattering coefficients are normalized to the diameter interval (solid line: 400 nm, dotted line: 800 nm).

## 2.10 Mie Scattering

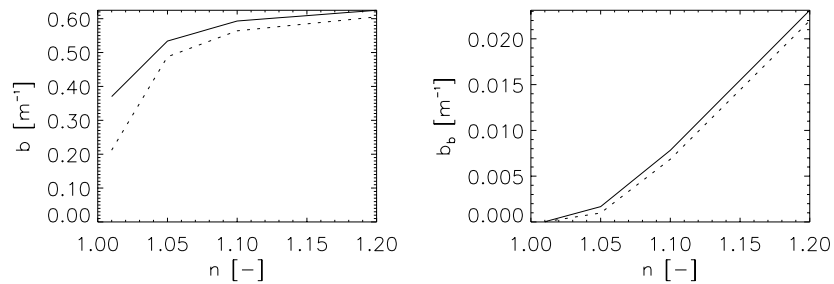


**Figure 2.16** Total scattering and backscattering coefficients as a function of the real refractive index  $n$  (solid: 400 nm, dotted: 800 nm).

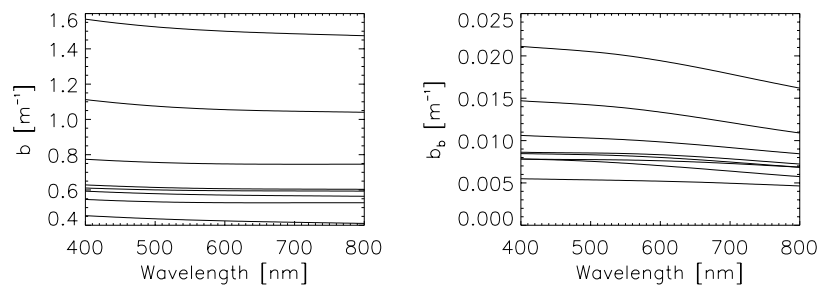


**Figure 2.17** Wavelength dependence of the total scattering and backscattering coefficients for different test sites in Lake Zürich (26.8.1998, samples just below the water surface). The calculations were performed for real refractive index  $n = 1.1$ . The differences between the curves of the different sizes show the importance of the particle size distribution on the scattering properties.

The smooth signature of the curves shown in Fig. 2.17 is due to the neglect of absorption. As stated above, the Kramers-Kronig relation (Eq. 2.55) allows the investigation of the influence of absorbing particles. The imaginary refractive index  $n''$  is calculated using Eq. 2.53 and Eq. 2.54 with  $n(500\text{nm}) = 1.1$ , and the phytoplankton absorption given by Lee's formula (Eq. 2.38) with  $a_p^*(440\text{nm}) = 0.03 \text{ m}^{-1} / (\mu\text{g l}^{-1})$  and  $CHL = 5 \mu\text{g l}^{-1}$ . The models (Fig. 2.18) show the large impact of absorption on the absolute quantities and relative changes of the signature of  $b$  and  $b_b$ . The results confirm Eq. 2.43 which states that the scattering coefficients are inversely proportional to the absorption coefficients.

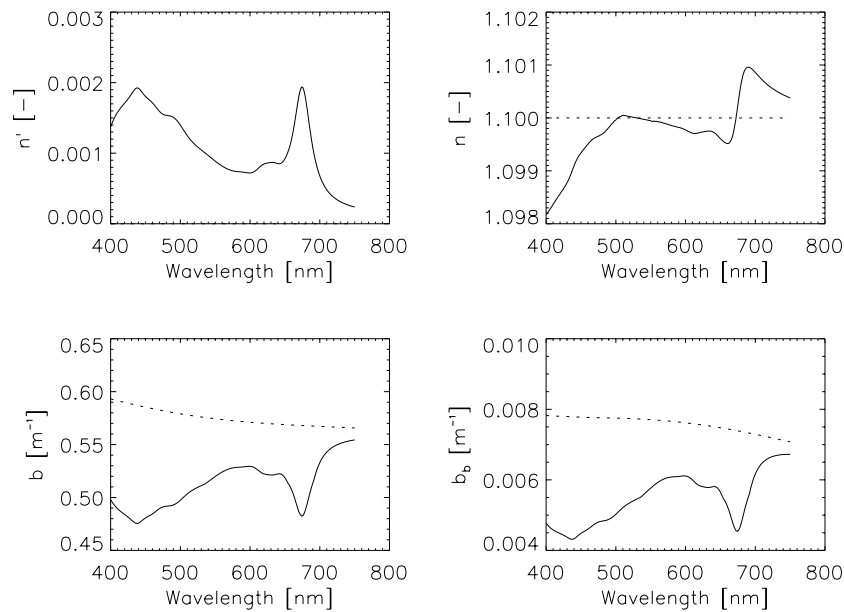
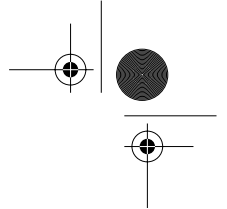


**Figure 2.18** The influence of absorbing particles on the scattering properties. Top left: imaginary part of the refractive coefficient. Top right: real part of the refractive coefficient (solid: with absorption, dotted: without absorption). Bottom left: total scattering coefficient. Bottom right: backscattering coefficient.

Theoretically, scattering in water bodies can be accurately described with Mie theory, the relation between absorption and scattering given by the Kramers-Kronig relation, and some assumptions about the absorption and  $n(\lambda_0)$ . This subject has been studied thoroughly in the literature (Kirk, 1975a.; Kirk, 1975b; Kirk, 1976; Bricaud and Morel, 1986; Gege, 1994).

In practice, not all driving factors of scattering are known such as the complex indices of refraction of the scatterer as a function of wavelength, the exact particle size distribution, the internal structure of the algae, and all three dimensions of the particle. However, Bricaud et al. (1988) reported for diverse phytoplankton species, that the influence of cell shape and internal structures on the attenuation and scattering coefficient does not appear crucial. It could be concluded that our calculations well reproduce the reality, as only  $n(\lambda_0)$  is not known exactly. However, the results have first to be compared with real measurements before the accuracy of our approach can be assessed (see Chapter 3.5 and Chapter 3.6).



## 2.11 Determination of Water Quality Parameters

The determination of the radiation is called *forward modelling* if the concentration of the lake water constituents and all other model parameters are known. This has been described in the previous chapter. However, in practice, the radiation is known and the water constituents are to be determined; this is called *inversion* or *backward modelling*.

Different implementations of inversion algorithms are found in the literature. They can be characterized by their empiricism, by the number of iterations, by the ability to determine more than one parameter simultaneously, and by the variable which is minimized to find the solution.

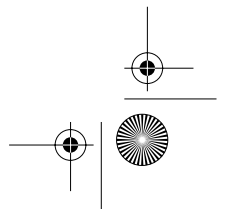
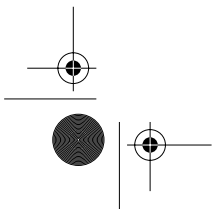
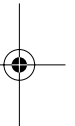
In most cases, a distinction is made between empirical and analytical methods. *Empirical* methods use only statistical dependencies, whereas *analytical* methods use physical knowledge. The use of empirical (i.e., statistical) methods is in general not suitable for the analysis of inland waters, as not all constituents are statistically correlated. As stated in Chapter 2.4, particulate matter can be autochthonous or allochthonous, but only the former is statistically correlated to pigments. Analytical models do not have these restrictions, because the influence of all sorts of parameters can be included. On the other hand, physical models and the inherent parameters must be well-defined. And even if they are exactly known, the separation of the influence of the constituents on the signature is only possible if their inherent properties differ from each other significantly. Additionally, analytical models should only be considered, if hyperspectral data are available which account for small-scale spectral features. Intermediate stages of empiricism are considerable. *Semi-empirical* methods use physical knowledge for the determination of a model equation, but determine the model parameters statistically, based on measurements. *Semi-analytical* methods use simplified physical models and employ parameters that still have a physical meaning.

Methods can be classified by the number of iterations. *Explicit* solutions are obtained by formulas that yield the desired parameter as a function of measured radiometric quantities in a straightforward process. Solutions of this kind are rare. *Implicit* solutions are obtained by solving a sequence of direct problems in an iteration process.

The ability to determine more than one parameter simultaneously is another important issue, as in inland waters, constituents can not correlate with each other.

Finally, the methods can be divided into methods that minimize over *biophysical* variables or over the *radiometric* variables, respectively.

There is a wide range of methods that can be found in the literature and



only a selection can be presented here: band ratio, differential absorption method, derivative spectra, curve fitting, matrix inversion, look-up table, and neural networks. The first three methods are statistical approaches, the next two invert the single scattering approximation, and the latter two are analytical methods. Tab. 2.6 shows the characterization of all methods discussed in the following section. In this work, the main focus is put on the determination of chlorophyll *a* as it is a suitable parameter for the determination of the water quality (Chapter 1.2).

**Table 2.6** Characterization of inversion methods.

	empirical	semi-empirical	semi-analytical	analytical	explicit	implicit	minimizes biophysical variable	minimizes radiometric variable	determines each parameter separately	determines all parameters simultaneously
Band ratio	+	+	(+)		+		+		+	
Differential absorption		+			+		+		+	
Derivative spectra	+				+		+		+	
Curve fitting			+			+		+		+
Matrix inversion			+		+			+		+
Look-up table				+		+		+		+
Neural networks				+	+		+			+

### *Band Ratio*

The chlorophyll *a* concentration (*CHL*) can be calculated as follows (Gordon and Morel, 1983; O'Reilly et al., 1998; Sturm 1993):

$$\log(CHL) = c_0 + c_1X + c_2X^2 + c_3X^3, \quad (2.56)$$

where *X* is given by either of the expressions:

$$\begin{aligned}
 X &= \frac{L_w(\lambda_1)}{L_w(\lambda_2)} \text{ or } X = \log \frac{L_w(\lambda_1)}{L_w(\lambda_2)} \text{ or } X = \frac{R_{rs}(\lambda_1)}{R_{rs}(\lambda_2)} \text{ or} \\
 X &= \log \frac{R_{rs}(\lambda_1)}{R_{rs}(\lambda_2)} \text{ or } X = \log \frac{R(\lambda_1)/Q(\lambda_1)}{R(\lambda_2)/Q(\lambda_2)} \quad (2.57)
 \end{aligned}$$

or an equivalent ratio. In most cases, only the first two or three terms of Eq. 2.56 are considered (i.e.  $c_2 = c_3 = 0$ ).  $L_w$  is the water-leaving radiance,  $R_{rs}$  the ratio of the water-leaving radiance to the downwelling irradiance (Eq. 2.7), and  $R/Q$  the ratio of the upwelling radiance to the downwelling irradiance in water (Eq. 2.6). The model parameters  $c_i$  can be determined using imaging and field data (semi-empirical) or modelled data (semi-analytical).

For open ocean water,  $\lambda_1$  is usually taken at the first chlorophyll absorption maximum at 440 nm, and  $\lambda_2$  at 550 nm where the radiation is only weakly dependent on *CHL*. For coastal waters or inland waters,  $\lambda_1$  is chosen at the second absorption maximum at 670 nm (since the first maximum is covered by gelbstoff absorption and other pigments) and  $\lambda_2$  at 700 nm (Dekker, 1993) where the radiation only weakly depends on *CHL*.

This method can also be used for the determination of suspended matter, as shown in Gordon and Morel (1983) or in Lathrop et al. (1991).

#### Differential Absorption Method

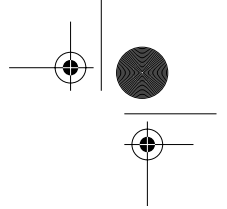
This method is similar to the band ratio method<sup>1)</sup>, but uses not only one, but at least two reference wavelengths. One possible implementation of this technique is the continuum interpolated band ratio (CIBR):

$$R_{CIBR} = \frac{L_M \cdot (\lambda_{r2} - \lambda_{r1})}{L_{r1} \cdot (\lambda_{r2} - \lambda_m) + L_{r2} \cdot (\lambda_{r1} - \lambda_m)}, \quad (2.58)$$

which is correlated with *CHL*.  $L_{r1}$ ,  $L_{r2}$ , and  $L_m$  are the water-leaving radiances at  $\lambda_{r1}$ ,  $\lambda_{r2}$ , and  $\lambda_m$ , respectively where  $\lambda_m$  lies between the other two bands, and is preferably situated in the centre of the absorption feature of interest.

Bruegge et al. (1990) used this method for the first time for the determination of water vapour in the atmosphere. Since more than one reference band is used, it is expected that this method yields more stable results than the band ratio methods. Kurer (1994) applied this approach to AVIRIS data for the detection of chlorophyll *a*.

<sup>1)</sup> In fact, the band ratio methods represent the simplest form of a differential absorption method.



### *Derivative Spectra*

This method is traditionally used in laboratory spectroscopy for the separation of overlapping influences of different substances (Martin, 1957), but has also been applied to hyperspectral field data (e.g., Chen et al., 1992, Goodin et al., 1993). The derivative reflectance spectra with respect to the wavelength is calculated and correlated with the parameter of interest. This method requires high radiometric precision and many adjacent small bands. As these data requirements are hardly met by today's systems, this method, to the author's knowledge, has not yet been applied to remote-sensing data.

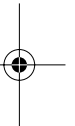
### *Curve Fitting*

The single scattering approximation (Eq. 2.21) can be solved for water constituent concentration using standard non-linear least-squares fitting routines as applied in Bukata et al. (1995), Doerffer and Fischer (1994), and Gege (1994). These routines determine the parameter set iteratively where the gradient of a figure of merit (i.e., the root mean square) with respect to the desired parameters is zero.

In this study, the Levenberg-Marquard algorithm was used (Press et al., 1988). First, an initial parameter set is chosen and  $R/Q$  is evaluated using Eq. 2.21. If the modelled value is close to the measured one, then the parameter set is chosen as the solution. Otherwise, a new parameter set is taken using the derivations of  $R/Q$  with respect to each constituent. This procedure is repeated until an acceptable solution is found (Fig. 2.19).

A disadvantage of curve fitting methods is that no minimum, or at least not the absolute minimum, of the merit function can be found, but only a local minimum depending on the starting value. This is a problem particularly if the initial guess is far from the effective solution. Another problem is the determination of the convergence tolerance which determines if the resulting parameter set is found. Usually the optimization routine is discontinued after a specified number of iterations in order to prevent endless loops. This inversion method is also much slower than the matrix inversion method. On the other hand, the convolution of the signal with the response function of the sensor<sup>1)</sup> is easily done. First, the reflectance is calculated quasi-continuous and then convolved to the sensor specifications; this corresponds to the real

<sup>1)</sup> Convolution is the algorithm that describes the weighting of a physical signal (e.g. radiance) with the single response functions of the bands of a sensor. This weighting can be expressed with  $S_i = \int S(\lambda) \times RSP_i(\lambda) d\lambda / \int RSP_i(\lambda)$ , where  $S_i$  is the convolved signal,  $s$  the continuous signal,  $\lambda$  the wavelength,  $RSP_i$  the response function of channel  $i$ . In case of symmetrical response functions and if the response function lies in a linear region, then the convolution leads to the same value as the original signal at centre wavelength. At peaks and troughs, the convolved signal is lower or higher, respectively, than the original signal leading to signatures with less pronounced extremes.



physical situation as opposed to the calculation sequence of the matrix inversion method<sup>1)</sup>.

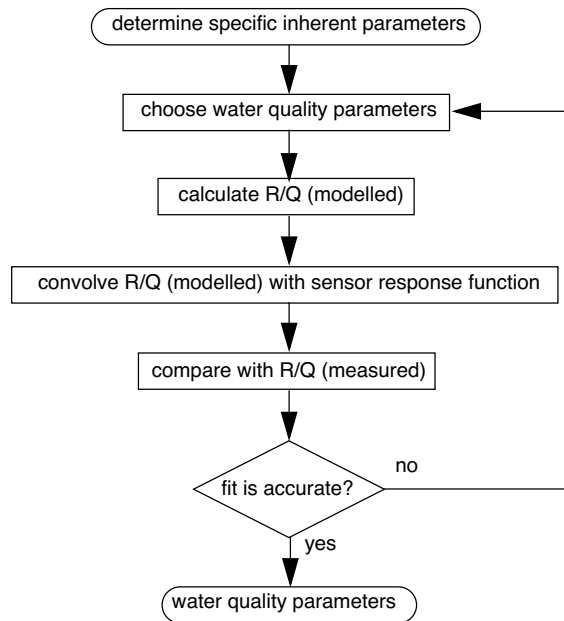


**Figure 2.19** Flowchart of the curve fitting method. This algorithm involves several iterations, rendering it slower than a straightforward method. Compare with the matrix inversion method (Fig. 2.20). Modified from Keller (2001).

### Matrix Inversion

The matrix inversion approach tries to determine *CHL* by inverting the single scattering approximation (Eq. 2.21) with matrix inversion techniques. The approximation can be rewritten as a linear equation system for the desired water constituents (Hoge and Lyon, 1996; Vasilkov, 1997; Keller et al., 1998).

The equation system depends on the assumption made for absorption and scattering. For example, if we define:

$$a(\lambda) = a_w(\lambda) + a_g(\lambda) + CHL \cdot a_p^*(\lambda), \quad (2.59)$$

<sup>1)</sup> Here, R/Q is assumed to be well-known (i.e., errors introduced by pre-corrections are not included).

and

$$b_b(\lambda) = b_{b,w}(\lambda) + CHL \cdot b_{b,org}^*(\lambda) + b_{b,0} \cdot b_{b,inorg}^*(\lambda), \quad (2.60)$$

we obtain an equation system for  $CHL$  and  $b_{b,0}$ :

$$\begin{aligned} & CHL \{ \omega(\lambda) [a_p^*(\lambda) + b_{b,org}^*(\lambda)] - b_{b,org}^*(\lambda) \} \\ & \quad + b_{b,0} \cdot b_{b,inorg}^*(\lambda) \{ \omega(\lambda) - 1 \} \\ & = b_{b,w}(\lambda) - \omega(\lambda) [b_{b,w}(\lambda) + a_w(\lambda) + a_g(\lambda)] \end{aligned} \quad (2.61)$$

with the single-scattering coefficient  $\omega(\lambda)$  defined in Eq. 2.22. If more than two bands are used, Eq. 2.61 becomes an overdetermined equation system (i.e., one equation for each band) which can be solved using standard least square matrix inversion techniques. In this study, the singular value decomposition was applied (Press et al., 1988). The form of Eq. 2.61 which is not unique, has been chosen this way, as it yields the most stable results. Especially the reciprocal of  $\omega(\lambda)$  has been omitted, since the weighting of small values would lead to artefacts in the inversion process.

This method is advantageous as the solution can be found in a straightforward manner without any iteration techniques (Fig. 2.20) rendering this method to be very fast. The disadvantage is that the convolution of the inherent spectra with the response function of the sensor has to be carried out before the evaluation of Eq. 2.21. This effect leads to a biased error. The broader the width of the sensor bands, the greater the additional uncertainty.

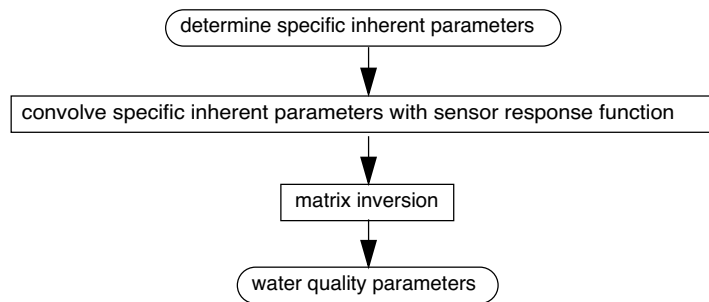
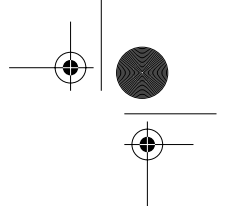


**Figure 2.20** Flowchart of the matrix inversion algorithm. This method is straightforward and fast. Compare with the curve fitting method (Fig. 2.19). Modified from Keller (2001).



### *Look-up Table Approach*

The remote-sensing reflectance or the at-sensor radiance is calculated for different combinations of constituent concentrations and atmospheric parameters. The modelled spectra are compared with the measured values, and that combination which shows the least differences (i.e., the smallest root mean square) is taken as the solution set. In general, the calculation of the LUT is very time consuming, but allows the use of exact reference models. The larger the generated LUT, the slower become access and inversion.

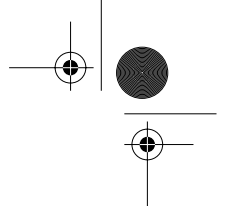
### *Neural Networks*

In a first step, a LUT is generated, which serves as a basis for the (time consuming) training of a neural network (Buckton et al., 1999; Kleiner and Brown, 1999; Schiller and Doerffer, 1999). The advantage of this approach is that even large LUT can be inverted very fast and that non-linearities are considered.

Theoretically, the neural network could also be fed with *in situ* measurements which would be of great advantage as we could neglect details of the physical processes and parameters. However, the number of weights needed for the determination of the network is large (in the order of  $10^2$  to  $10^3$  values), so that it is virtually impossible to provide enough measurement points.

## **2.12 Review**

Tab. 2.7 lists the advantages and disadvantages of empirical and analytical methods. The main advantage of analytical methods is the ability to determine simultaneously more than one parameter and to adjust model parameters without spectral measurements, allowing the generalization of the method for other times and water types. Additionally, it is possible to make predictions about the performance of future sensors. On the other hand, empirical methods allow a quick implementation and therefore a fast overview of the information content in spectral image data, even if inherent parameters of the waters are not known.

**Table 2.7** Advantages and disadvantages of empirical and analytical approaches.

	Empirical methods	Analytical methods
Approach	statistical	physical
Physical knowledge (model and input parameters)	not necessary	necessary
Mathematical skills required	little	strong
Inversion	easy, fast and robust	difficult, slow and less robust
Calibrated instrument	not required	required
Simultaneous determination of different water parameters	not possible in general	possible
Extrapolation (different water types, time)	not possible in general	possible
Instrument and scene dependence	yes	no

The suitable potential inversion methods for the most important parameters in remote-sensing of inland waters - chlorophyll *a*, particulate matter, and gelbstoff - are tabulated in Tab. 2.8. Note that band ratio, differential absorption, and derivative spectra methods can not be applied if the spectral inherent property of the parameter of interest has a "flat" signature without any absorption feature, as it is the case for gelbstoff and also to a certain extend for suspended matter, which can hardly be calculated by these methods.

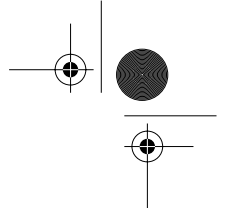
The accuracy of the different methods depends on the water type, which makes it difficult to predict the performance of a method. If the relationship between optically relevant constituents is stable, then empirical methods can lead to more accurate results than analytical methods. In any case, the choice of a method should also take into account the available sensor. The application of physical models can be an overkill, if only multi-spectral sensors are used with broad bands. Additionally, empirical methods can be the only convenient solution if remote-sensing data cannot be calibrated.

**Table 2.8** Potential of inversion methods.

	Chlorophyll <i>a</i>	Particulate Matter	Gelbstoff
Band ratio	x	x	
Differential absorption	x		
Derivative spectra	x		
Curve fitting	x	x	x
Matrix inversion	x	x	x
Look-up table	x	x	x
Neural networks	x	x	x

In this study, emphasis is put on two semi-analytical approaches – curve fitting and matrix inversion – due to the following reasons:

- Empirical methods prove very successful in open ocean waters, but less successful in more complex coastal waters and inland waters. Furthermore, they do not allow an insight to the physics which is the only way of improving inversion techniques.
- For the monitoring of the water quality usually no real time information is needed by the end-user (Dekker et al., 1998). This allows the use of physical methods which need in general more computing time.
- The LUT and the neural network approaches were not pursued in this study, as a fast response on changing conditions in a lake and knowledge (e.g., changing inherent parameters) is not realistic. Furthermore, it is disadvantageous that the inversion is kept in a black-box and that consequently, several parts of the physical model cannot be validated easily for their plausibility.
- The curve fitting and matrix inversion methods allow a flexible and simultaneous determination of different parameters. Additionally, the various steps involved in the analysis can be separated and tested. A comparison between these two methods is given in Chapter 5.6.



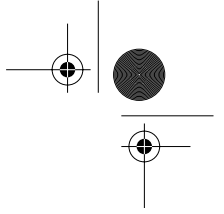
## 2.13 Conclusions

The main goal of this chapter was to show which parameters influence the spectral signature and how these different effects can be separated in the inversion procedure. The most important aspects are:

- The following parameters should be available for the characterization of a lake although it is well understood that only in few cases all of these parameters are known: pigment concentrations (chlorophyll *a*, phaeophytin), suspended matter concentration (organic and inorganic), particle size distribution, *DOC* concentration, gelbstoff absorption, algae species composition, specific algae absorption, Secchi depth, *in situ* transmission, *in situ* radiometric measurements, and information about the lake bottom including water depth.
- Empirical inversion methods are robust and does not require absolutely calibrated or atmospheric and air-water interface corrected input data.
- Analytical inversion methods include the influence of different constituents. Additionally, they allow generalizations of the results and predictions for new remote-sensing systems. However, the inherent parameters and the bio-optical model have to be accurately known.
- Unambiguous inversion results can only be obtained if the influence on the signature of the various constituents differ significantly from each other.

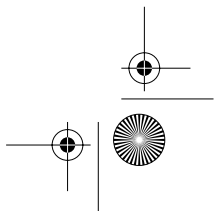
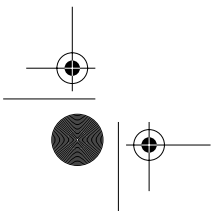
Our own measurements and calculations showed following results:

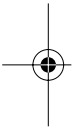
- The particle distribution was divided into two segments above and below the particle size of around 10  $\mu\text{m}$ . Both segments could be described by the Junge distribution. The particulate matter distribution classes did not correlate with *CHL*. Therefore, it is not expected that the backscattering coefficient depends on this constituent; this will have consequences on the determination of *CHL*, since the reflectance is nearly proportional to the backscattering coefficient.
- The gelbstoff absorption could be well described with an exponential model. The absolute value was highly variable, whereas the exponent varied only little and corresponded well with literature values. The absorption was only weakly dependent on the *DOC* concentration.
- Each algae group has its specific phytoplankton absorption caused by different pigments and internal structures. Nevertheless, in most cases, it can be accurately approximated with only one free parameter,  $a_p^*$  (440 nm).
- Mie calculations can support the determination of relevant parameters

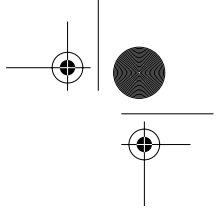


## 2.13 Conclusions

for remote-sensing methods. It could be shown that the size distribution and the complex index of refraction determine the scattering. Almost all backscattering originates from the particles smaller than  $10 \mu\text{m}$  because of their total geometrical cross section and their higher refractive index.







## Chapter 3

# Radiometry in Natural Waters

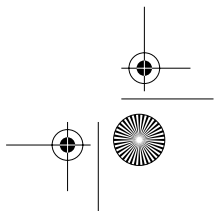
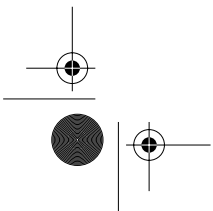
*In situ* radiometric measurements are required for the calibration and validation of radiative transfer models and inversion methods. Unfortunately, radiometric measurements are among the least reliable of all physical measurements (Kostkowski, 1997). This chapter outlines aspects of the spectrometer specification, the absolute radiometric calibration, and the problems associated with shipboard radiance measurements. After the theory, own measurements are described with the goal to determine the dependence of inherent parameters on chlorophyll *a*.

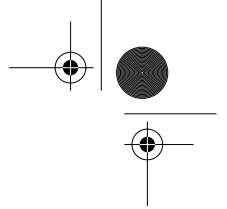
### 3.1 Spectroradiometer

The quality of underwater spectroradiometer measurements depends on the following keypoints:

- *Method.* The time of a spectral scan is important because the environment is changing with time (atmosphere, capillary waves, currents). For the same reason, it ought to be possible to make simultaneous radiometric measurements in up- and downward direction. If it is not possible to measure simultaneously at different depths, an additional sensor for reference measurements above the water surface is recommended.
- *Operationality.* Material and staff have to be considered. Ideally, the measurement of additional parameters such as water depth (e.g., pressure) or inclination is feasible.
- *Size of the underwater box.* Self-shading effects of mooring and holding devices must be minimized (e.g., with the use of fibre optics).
- *Quality.* It is determined by the spectral range, number of channels, spectral resampling interval, full width at half maximum (*FWHM*), accuracy of the spectral and radiometric calibration, reproducibility, and signal-to-noise ratio (*SNR*).
- *Price and additional development adaptation costs.* This aspect is important as normally, the instruments are not generally available.

For this study, two different underwater spectroradiometer systems were used. In the beginning, the LI-COR LI-1800UW was employed. Due to its





limitations, it was decided to buy a system, the GER1500 double field-of-view system. Both systems are described in the following sections. A summary of the technical specifications of the instruments is given in Appendix A.

#### *LI-COR LI-1800UW*

This system includes a spectroradiometer that is mounted in a watertight box. It uses a silicon detector to provide measurements between 300 and 1100 nm with wavelength sampling intervals of 1, 2, 5 or 10 nm. Light is sampled through a cosine receptor enabling the measurement of down- or upwelling irradiance (Fig. 2.2). With scan rates ranging from 20 - 45 nm per second, a scan over the entire wavelength range takes 20 to 40 seconds. Since the instrument was rented, the calibration was beyond direct control.

The LI-1800UW system has some major limitations:

- It is not possible to measure simultaneously in up- and downward direction.
- It is not possible to measure the upwelling radiance. In comparison to the measurements of remote-sensing devices, this is of great interest. The transformation of irradiances to radiances<sup>1)</sup> is in general not intuitive due to the non-uniform radiation distribution.
- Scanning systems result in noisy spectra due to capillary waves especially near the air-water interface (Fig. 3.2).
- Since more than one scan has to be performed in order to minimize the effects of surface waves, and since up- and downwelling irradiance have to be measured one after the other, the measurement of an entire depth profile is not operational (1/2 hour for 4 depths).

#### *GER1500 DFOV System*

Due to the limitations of the LI-COR system, the double field-of-view system of GER (GEOPHYSICAL & ENVIRONMENTAL RESEARCH, USA) was procured. It consists of two GER1500 spectroradiometers that simultaneously measure the upwelling radiance  $L_u$  and the downwelling irradiance  $E_d$ . The integration time can be varied from 5-160 ms. Each spectroradiometer uses a 512 channel silicon linear array detector that measures between 350 nm and 1050 nm with a bandwidth of approximately 3 nm.

Both instruments were mounted in an underwater box (Fig. 3.1) and controlled from the surface via a RS232 interface<sup>2)</sup>. Power supply is ensured within the same cable coat. The instruments can be operated with a car battery

<sup>1)</sup> irradiance = angle dependent radiance integrated over the whole hemisphere (see Chapter 2.2).

<sup>2)</sup> The underwater box was developed and constructed by University of Uppsala, Sweden (D. Pierson and S. Djurstrom).

### 3.1 Spectroradiometer

(24 V) which allows measurements during one entire day.

The upward pointing instrument is fitted to an opal glass cosine collector in order to measure  $E_d$ . The downward instrument looks through a silicon window at the bottom of the box measuring  $L_u$ , but it can also be connected to a fibre optic cable whose end is approximately 0.5 m away from the underwater box to minimize self-shading effects caused by the box. This set-up was not available for the first sampling periods and consequently, all measurements were performed with the window configuration.

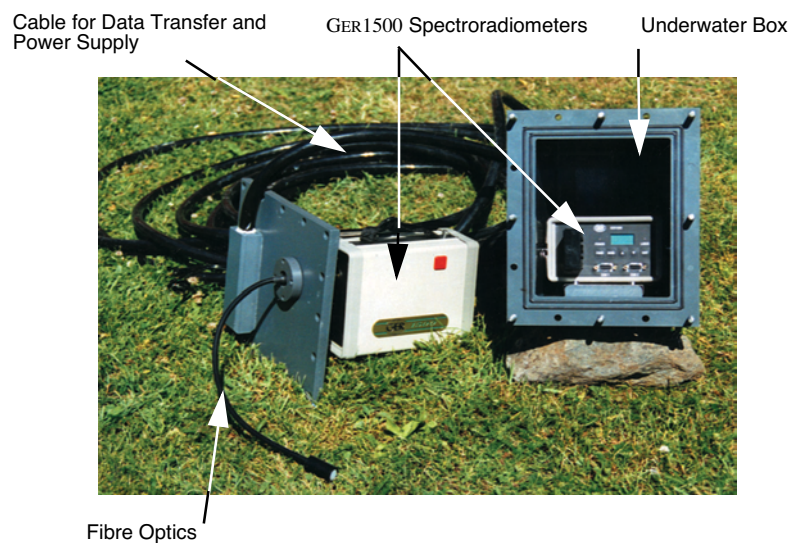
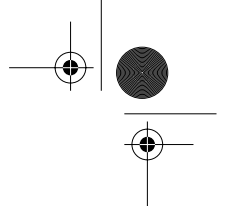


**Figure 3.1** The GER1500 DFOV System consists of two field spectrometers mounted in an underwater box (l x w x h = 35 cm x 35 cm x 41 cm). The instruments are controlled from the surface via a connection cable. In the figure, the fibre optics is also shown which can be attached instead of a window on the bottom side of the box for the measurements of the upwelling radiance.

In the following chapters, emphasis is put on the measurements performed by the GER1500 DFOV system due to the reasons mentioned above, but also because more measurements were performed with this system, and more auxiliary data were available.



### 3.2 Absolute Radiometric Calibration

An absolute radiometric calibration is needed if absolute quantities are required, if two different instruments are compared to each other, and if no measurements of a reference target can be made, as it is the case for the measurements with the GER1500 DFOV system. These instruments were calibrated using an integrating calibration sphere standard (OPTRONIC LABORATORIES). The following aspects have to be considered:

- *Absolute Standard.* Calibration lamps may degrade with time. If ratios of measurements of two instruments ( $R, R_{R_N}$ ) are calculated, only a relative radiometric calibration is needed.
- *Linearity.* This is especially important if a wide range of energy is measured. This was successfully tested for both GER1500 spectrometers.
- *Temperature Dependence.* Calibration tests of a GER3700 spectrometer did not show temperature dependence for a similar SiO detector (Schaepman, 1998) and it is assumed that such effects can be neglected for the measurements using the GER1500 DFOV system.
- *Angular Response Function.* Errors may be introduced by non-perfect cosine properties of the irradiance collector. In air, satisfying collecting properties are achieved by roughening the surface. However, when submerged in water, the roughened surface ceases to be effective, and the collecting properties change significantly. It is particularly difficult to measure accurately at large zenith angles. The systematic error introduced by an imperfect cosine collector cannot be characterized by a single number, since the measurement depends on the properties of the collector as well as the radiance distribution which changes with location and depth. Smith (1969) calculated errors for a typical radiance distribution for a cosine collector – similar to the one used in the GER1500 DFOV system– of 5.3% at 4.24 m and 6.3% at 66.1 m depth.
- *Polarization Effects.* Schaepman (1998) showed experimentally for a GER3700 that for perfectly polarized incoming light, the errors introduced are in the order of 6%. And in fact, the underwater light fields are partially elliptically polarized. This is caused by aerosol scattering, scattering by water molecules and by small particles, as well as by refraction processes at the air-water interface. Assuming that the incoming light is 50% polarized and that the probability is 50% that the instrument is oriented that way, that such polarization effects occur, then the uncertainty can be assumed to be about  $0.5 \cdot 0.5 \cdot 6\% = 1.5\%$ . It is expected that the additional error introduced by the window of the underwater box is within a similar range.

- *Pressure effects* (Mueller and Austin, 1995). They were not considered in this study as the measurements were performed at a maximum depth of only 20 m.
- *Immersion Effect*. The air calibrations have to be corrected for underwater use since the transmissivity of an opal glass or a diffusor is less in water than in air due to internal and external interface reflections. This effect must be considered whenever measurements above and below the water surface are made or two different instruments are compared to each other.
  - *Irradiance Collector*. Westlake (1965) gives an approximate correction value for the immersion factor of 1.25 which has to be multiplied with the air calibrated measurements. Smith (1969) showed that the spectral dependence of the correction factor is directly correlated to the collector absorbance. He determined a factor of 1.39 for 430 nm which decreases almost linearly to 1.25 for 750 nm. The usage of the mean value of 1.32 for the whole spectral range leads to a maximum uncertainty of 5%.
  - *Radiance Collector*. In order to correct a radiance detector, also the change of the FOV due to the change of the refraction index has to be considered. The air-calibrated measurements has to be multiplied by the immersion factor (Mueller and Austin, 1995):

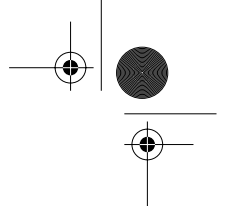
$$F_i = n_w(\lambda) \times \left[ \frac{n_w(\lambda) + n_{glas}(\lambda)}{1 + n_{glas}(\lambda)} \right]^2, \quad (3.1)$$

where  $n_{glas}$  is the refraction coefficient of the window of the underwater enclosure. For  $n_{glas} = 1.46-1.90$ ,  $F_i(\lambda)$  lies between 1.67-1.74. If the mean of this range, 1.705, is used for further calculations, then the maximum error is about 2%. Aas (1994) suggested a factor of 1.73, which also lies in the suggested interval.

Adding up the errors introduced by the angular response function (only irradiance collector), the polarization effects (spectrometer and window of the underwater box), and immersion effects, the maximum overall error of irradiance measurements is:

$$\sqrt{0.05^2 + 0.015^2 + 0.015^2 + 0.05^2} = 7.4\%,$$

and for radiance measurements:



$$\sqrt{0.015^2 + 0.015^2 + 0.02^2} = 2.9\% .$$

Of course, uncertainties introduced by the measuring set-up are not included in these numbers. This will be discussed in the next chapter.

### 3.3 Shipboard Measurements

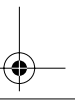
Near surface measurements should be performed at least at the top three optical depths (Eq. 2.19). In order to reliably extrapolate to  $z = 0$ , it is essential to obtain a profile at least for the top optical depth (Mueller and Austin, 1995).

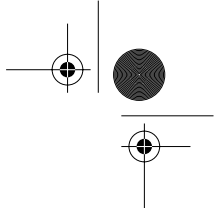
There are three primary sources of error in the determination of apparent optical properties: the perturbation by the ship, changing atmospheric conditions, and surface waves. The influence of the *ship shadow* depends upon the solar zenith angle, the spectral attenuation in the water, cloud cover, ship size and colour, and the geometry of instrument deployment (Mueller and Austin, 1995). The influence of the ship shadow is best characterized in terms of the attenuation length  $1/K_d(\lambda)$ . The minimum distance  $d$  away from the ship where the influence of the ship can be neglected for  $E_d(\lambda)$  measurements can be estimated for a clear sunny sky by (Mueller and Austin, 1995):

$$d = \frac{0.75}{K_d(\lambda)} \text{ [m]} . \quad (3.2)$$

Accordingly, the distance from the ship is required to be  $3/K_u(\lambda)$  [m] for  $E_u(\lambda)$  and  $1.5/K_d(\lambda)$  [m] for  $L_u(\lambda)$  measurements. This can be achieved with floating plastic frames, extended booms or optical free-fall instruments. Gordon (1985) shows, based on Monte Carlo simulations, that the downwelling irradiance is relatively unperturbed by self-shading effects in the case of collimated illumination, while large effects are observed in the case of diffuse illumination. In the framework of our own measurements, the instruments were lowered by a winch attached to the rail. However, since only small boats were used compared to the ships used for ocean measurements for which the estimated distances are defined, it can be expected, that the measurements are reliable if the measurements are always performed between sun and boat (and not in the shadow behind the boat).

*Atmospheric variability* depends primarily upon sun elevation and variations in cloud cover. First order correction can be made using above water (on deck) measurements of downwelling spectral irradiance. In this study, no such instrument was available, but it is of course highly recommended.





*Surface waves* primary influence near-surface measurements (in air for upwelling radiation and in water for downwelling radiation). Plausibility tests should be made in order to decide whether and when measurements should be excluded from the analysis.

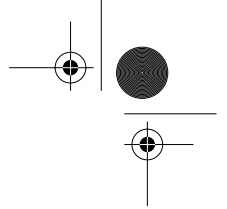
### 3.4 Determination of Inherent Parameters

As stated in the introduction of Chapter 2, inherent optical properties of water depend only on the medium, while apparent properties depend on the medium and the light field within the medium. The determination of inherent parameters in the laboratory is time consuming and often erroneous. Particularly absorption measurements and the determination of the scattering phase functions are rarely comparable between several measurement set-ups.

**Table 3.1** Semi-analytical models relating inherent and apparent parameters valid just below the air-water interface. All parameters are defined in Chapter 2.

Input Eqs.	Output Eqs.
Eq. 2.30	$b_b = \frac{K_d}{0.110} \cdot \frac{R}{Q} \quad (3.3)$
Eq. 2.32	$b_b = (2.8264R(1) - 3.8947R^2(1) - 36.232R^3(1)) \cdot K_d/D_0 \quad (3.4)$ with $R(1) = R(D_0=1)$
Eq. 2.22	$a = b_b \frac{1-\omega}{\omega} \quad (3.5)$ for known $R/Q$ , with $\omega$ given by Eq. 2.21, and $b_b$ by Eq. 3.3 for known $R$ , with $\omega$ given by Eq. 2.28/Eq. 2.29, and $b_b$ by Eq. 3.4
Eq. 2.31	$a = \frac{1}{1.0395} \frac{K_d}{D_0} - b_b \quad (3.6)$ for known $R/Q$ , with $b_b$ given by Eq. 3.3 for known $R$ , with $b_b$ given by Eq. 3.4
Eq. 2.27	$a = (0.975 - 0.629 \cos(\theta_{sw})) \frac{b_b}{R(z=0 \text{ m})} \quad (3.7)$ with $b_b$ given by Eq. 3.4 and $\theta_{sw}$ = sun zenith angle in water





Another possibility is the use of semi-analytical models given in Chapter 2.3, allowing the calculation of the total backscattering and absorption coefficients based on apparent quantities such as  $D_0$ ,  $K_d$ ,  $R$  or  $R/Q$ . The first term was calculated using Eq. 2.25, the other terms were determined by *in situ* measurements. Tab. 3.1 shows the re-arranged equations from Tab. 2.1.

As the main emphasis is put on the determination of  $CHL$ , the dependence of inherent properties on  $CHL$  is of special interest. The following models were investigated for scattering (Eq. 2.46):

$$b_b(\lambda) - b_{b,w}(\lambda) = b_{b,inorg}(\lambda) + CHL \cdot b_{b,org}^*(\lambda), \quad (3.8)$$

$$b_b(\lambda) - b_{b,w}(\lambda) = CHL \cdot b_{b,org}^*(\lambda), \quad (3.9)$$

where  $b_{b,inorg}$  and  $b_{b,org}^*$  are the inorganic and the specific organic backscattering coefficients, respectively.

Furthermore, the following model is tested for absorption (Eq. 2.45):

$$a(\lambda) - a_w(\lambda) - a_g(\lambda) = a_d(\lambda) + CHL \cdot a_p^*(\lambda), \quad (3.10)$$

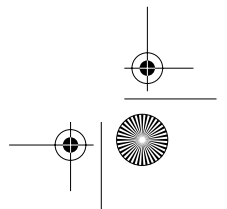
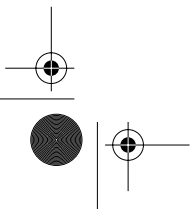
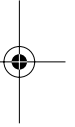
where  $a_g$ ,  $a_d$  and  $a_p^*$  denote the gelbstoff, detritus and specific phytoplankton absorption coefficients, respectively.

The quantities known or approximated are on the left hand side of the equation, the searched quantities on the right. As these are linear relations (for each wavelength), simple linear regression techniques lead to the scattering properties,  $b_{b,inorg}(\lambda)$  and  $b_{b,org}^*(\lambda)$ , and absorption properties,  $a_d(\lambda)$  and  $a_p^*(\lambda)$ .

For the calculations the software module RADIO has been developed, which is described in Appendix B.3.

### 3.5 LI-COR Measurements in Lake Zug

LI-COR measurements were carried out in Lake Zug (Chapter 1.3) in the framework of the CASI campaign in August 1997. Measurements were performed at five sites in up- and downwelling directions just above the water surface and at 0.5, 2.0, 3.5, and 5.0 m below the water surface. In order to minimize the surface effects caused by capillary waves (Fig. 3.2), several scans were taken (five scans close to the air-water interface). However, the measured spectrum had to be smoothed with a low pass filter before it could be carried on. Beside the radiometric measurement, chlorophyll *a* ( $CHL$ ) and dissolved organic carbon ( $DOC$ ) were also determined. See Chapter 5.2 for



information about the sampling sites and the measured parameters.

Since the instrument measures the downwelling irradiance, the irradiance reflectance  $R$  and downwelling diffuse attenuation  $K_d$  could be determined (Fig. 3.3). Only the topmost values in water were used for the determination of the reflectance. The attenuation coefficient was calculated by fitting all measurements to an exponential function (see Eq. 2.9). Note that  $K_d$  is equal for almost all sampling stations.

As stated in Chapter 2.1, the reciprocal of  $K_d$  is equal to the penetration depth for remote-sensing purposes. For Lake Zug, this was 1 m to 3 m depending on the wavelength. Since the maximum of the chlorophyll  $a$  concentration is at 3 m depth, it could be concluded that the influence of the vertical distribution of chlorophyll  $a$  on the water-leaving radiance is weak.

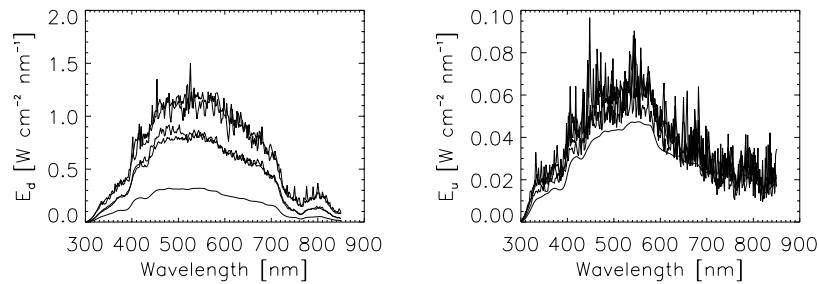


**Figure 3.2** Down- and upwelling irradiance measurements with the LI-COR system near the air-water surface for five sites in Lake Zug (left diagram: -0.5 m below the interface, right diagram: +0.5 m above the air-water interface). The measurements were disturbed by surface waves.

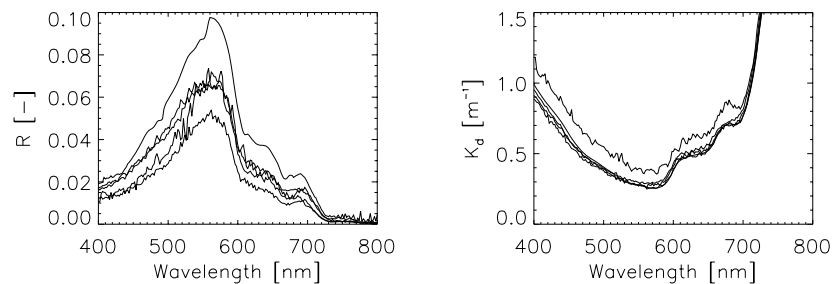
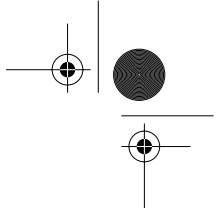


**Figure 3.3** Irradiance reflectance  $R = E_u/E_d$  and diffuse attenuation coefficient  $K_d$  based on top measurements at five sites in Lake Zug.



These two parameters allow the determination of the scattering coefficient  $b_b$  (Eq. 3.4) and the absorption coefficient  $a$  (Eq. 3.5 - Eq. 3.7). The case studies are summarized in Tab. 3.2 and Tab. 3.3.

**Table 3.2** Case studies for the determination of the scattering coefficient based on LI-COR measurements.

	Model	$b_b$
I	Eq. 3.4	Eq. 3.8
II	Eq. 3.4	Eq. 3.9

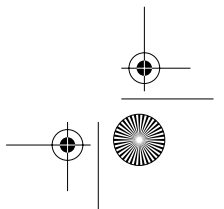
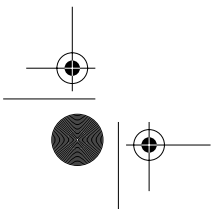
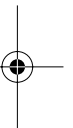
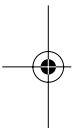
**Table 3.3** Case studies for the determination of the absorption coefficient based on LI-COR measurements.

	Model	$a$
I	Eq. 3.5	Eq. 3.10
II	Eq. 3.6	Eq. 3.10
III	Eq. 3.7	Eq. 3.10

As the gelbstoff absorption  $a_g$  has not been measured, it had to be parameterized with the *DOC* concentration using Eq. 2.35 and Eq. 2.36. The fit parameters were assumed to be equal to the values determined for Lake Zürich:  $S = 0.071 \text{ nm}^{-1}$ ,  $a_g^* = 0.048 \text{ l mg}^{-1}$ .

As stated above, the chlorophyll dependence of the backscattering coefficient on chlorophyll  $a$  is of special interest. However, no such relationship could be found neither for the scattering coefficient (Fig. 3.4) nor for the absorption coefficient (Fig. 3.5). Possible reasons for these results are that there is no such correlation, the data set was too small ( $n = 5$ ), the radiometer was not sensitive enough, or the measurements were incorrect due to surface wave effects or changing atmospheric conditions.

The spectral signature of the determined backscattering coefficient is similar to the calculated values using Mie theory (Fig. 2.18). It can be concluded that both, the determination of the backscattering coefficient based on Mie calculations and radiometric *in situ* measurements, represent well the actual situation in the water as both were determined independently of each other. We are fully aware, that this is only a qualitative comparison, and further work should aim at quantitative calculations, which is behind the



## 3.5 LI-COR Measurements in Lake Zug

subject of this study (here only the signature and influencing parameters were of interest).

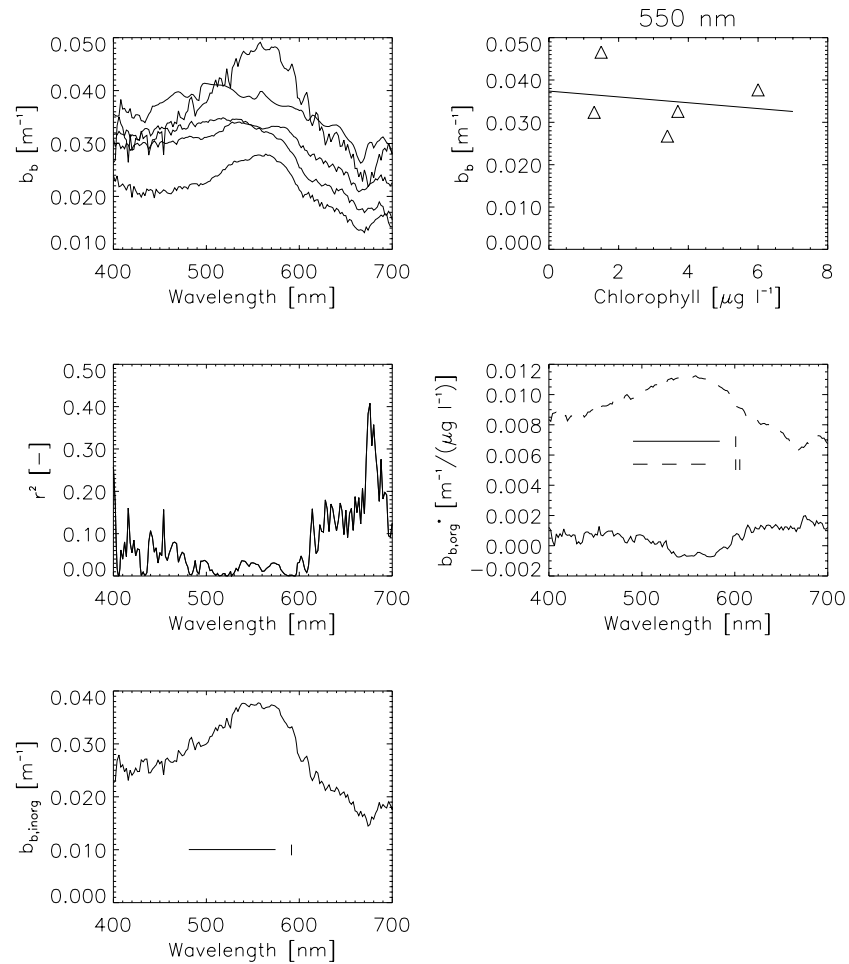


**Figure 3.4** Determined total backscattering coefficient  $b_b$  based on LI-COR measurements in Lake Zug for different sites (top left figure). The dependence of the scattering coefficient  $b_b$  on chlorophyll is only weak (top right, 550 nm), resulting into low correlation coefficients  $r^2$  (centre left). The specific organic ( $b_{org}$ ) and inorganic ( $b_{inorg}$ ) scattering spectra show only little variations (centre right and bottom left). The case studies (I and II) are summarized in Tab. 3.2.

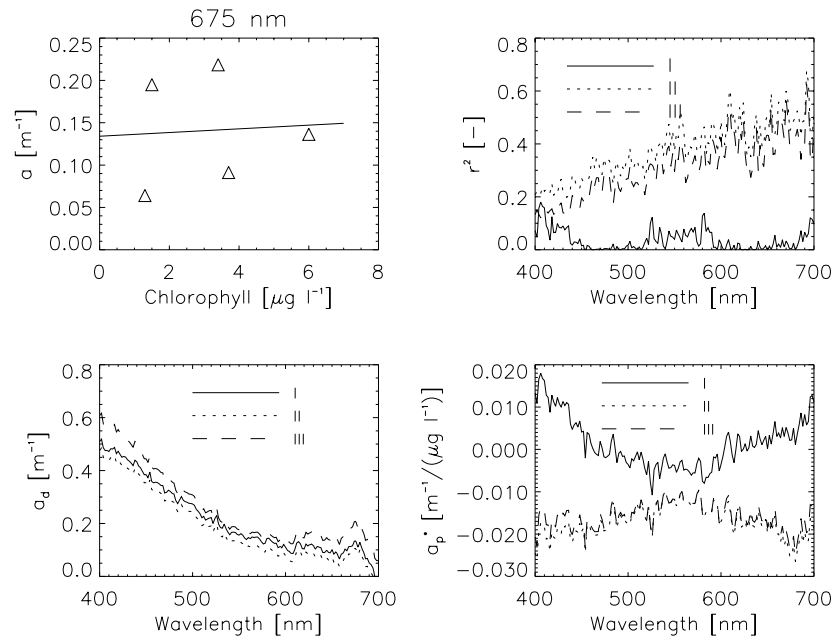
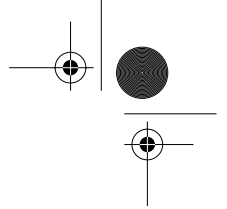


**Figure 3.5** Determined absorption coefficient based on LI-COR measurements in Lake Zug. The dependence of the absorption coefficient  $a$  on chlorophyll is only weak (top left figure, 675 nm), resulting into low correlation coefficients  $r^2$  (top right). The resulting specific detritus absorption spectra  $a_d$  are almost identical for all cases (bottom right). The phytoplankton absorption spectra  $a_p$  have an accidental appearance (bottom left). The case studies (I, II, and III) are summarized in Tab. 3.3.

### 3.6 GER1500 DFOV Measurements in Lake Zürich and Walensee

Between June 1998 and June 1999, measurements were performed in Lake Zürich and Walensee (Chapter 1.3). The main goal of the campaign was to become familiar to the spectral properties of different water types and their relationships with water quality parameters.

The measurements were performed in co-operation with the *Wasserversorgung Zürich* which routinely determines the water quality at several stations. Four main stations are situated in Lake Zürich at Lachen, Stäfa, Thalwil, and Zollikon, and one station in the middle of Walensee. With regard to remote-sensing applications, several interesting parameters were



### 3.6 GER1500 DFOV Measurements in Lake Zürich and Walensee

73

measured: Secchi depth, diverse pigments (chlorophyll *a* & *b* among others), *DOC* concentration, and algae composition. If possible, the gelbstoff absorption and the particle size distribution was measured in the laboratory for a better characterization of the water. Additional radiometric measurements were performed during a HYMAP campaign on August 26, 1998, at the lake dam near Rapperswil. For the characterisation of the atmosphere, the cloud cover was recorded.

The box including the instruments was lowered with a winch attached to the rail to the desired depth where a measurement was conducted. The first measurement is made with the whole box above the water surface, followed by a measurement with only the top end above but the bottom end below the interface. All subsequent samplings were taken with the whole box in the water (i.e., -0.1 m, -0.5 m, -1.0 m, -2.0 m,..., -18.0 m).

One disadvantage of the window solution provided by the underwater box is, that the measurements in up- and downwelling direction are not performed at the same depth as the upper and the lower window are separated due to the height of the box (0.41 m). For the determination of  $R/Q$  and the corresponding  $K_d$ , it was therefore necessary to interpolate the measurements in both directions to a reference depth (upper window). For stable atmospheric and air-water interface conditions, this approach is sufficient, for instable conditions, this leads to erroneous and useless data. This is especially a problem if the variations in the radiometric measurements introduced by such conditions is higher than the variations by changing inherent parameters. Consequently, the data had to be checked first. Of course, the most elegant solution would be to measure upwelling radiance and downwelling irradiance simultaneously at the same depth with an additional measurement of the downwelling irradiance at another depth (Bochter and Wallhäuser, 1996).

In the following sections, measurements and derived quantities are presented. Where not indicated otherwise, all measurements refer to Lake Zürich at the sampling location Thalwil on September 9, 1998. These data were chosen for illustration, because of ideal weather conditions (i.e., clear atmosphere), and as large chlorophyll *a* concentration gradients were measured in the water profile due to a blue algae bloom located at 10 m depth (Fig. 3.6).

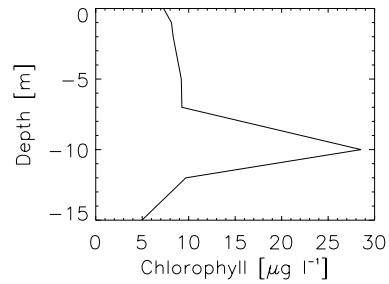


**Figure 3.6** Chlorophyll *a* concentration profile at the station Thalwil in Lake Zürich on September 9, 1998. A pronounced maximum is visible at 10 m due to a blue algae bloom.

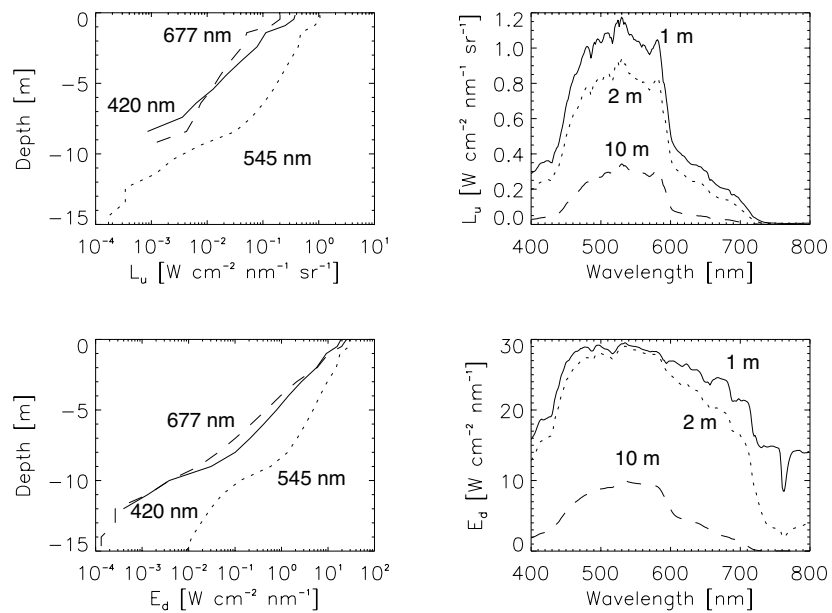


**Figure 3.7** Upwelling radiance  $L_u$  and downwelling irradiance  $E_d$  measurements.

As expected, the upwelling radiance is zero above 700 nm due to the high water absorption. The  $L_u$  and  $E_d$  measurements (Fig. 3.7) show that the expected exponential decay with depth is only valid in a first approximation. This has also consequences on the derived attenuation coefficient (Fig. 3.8) which varies with depth. The comparison with the chlorophyll  $a$  profile shows, that this parameter was strongly related to this constituent. On the other hand, the reflectance was almost constant over depth except for the near-infrared bands. The fact that the influence of the chlorophyll  $a$  concentration on the reflectance is only weak can also be shown if different reflectances are plotted at different sites with varying concentration; the resulting spectra seemed to be stronger influenced by other parameters, such as inorganic particulate matter. This has of course impacts on the retrieval of chlorophyll based on  $R/Q$  measurements.

With known  $R/Q$  and  $K_d$ , Eq. 3.3 can be used for the calculation of  $b_b$ , and Eq. 3.5 and Eq. 3.6 for the determination of  $a$ .  $R/Q$  was extrapolated just below the surface.  $K_d$  was calculated by fitting all  $E_d$  measurements above 5 m to an exponential function. Whenever possible, the gelbstoff absorption was measured in the laboratory. If no such measurements were available,  $a_g$  was parameterized with Eq. 2.35 and Eq. 2.36 based on the parameters determined for Lake Zürich:  $S = 0.071 \text{ nm}^{-1}$ ,  $a_g^* = 0.048 \text{ l mg}^{-1}$ . All measurements of Lake Zürich and Walensee were included in the analysis ( $n = 19$ ). The case studies are summarized in Tab. 3.4 and Tab. 3.5.

**Table 3.4** Case studies performed for the determination of the scattering coefficient based on GER1500 measurements.

	Model	$b_b$
I	Eq. 3.3	Eq. 3.8
II	Eq. 3.3	Eq. 3.9

**Table 3.5** Case studies performed for the determination of the absorption coefficient based on GER1500 measurements.

	Model	$a$
I	Eq. 3.5	Eq. 3.10
II	Eq. 3.6	Eq. 3.10

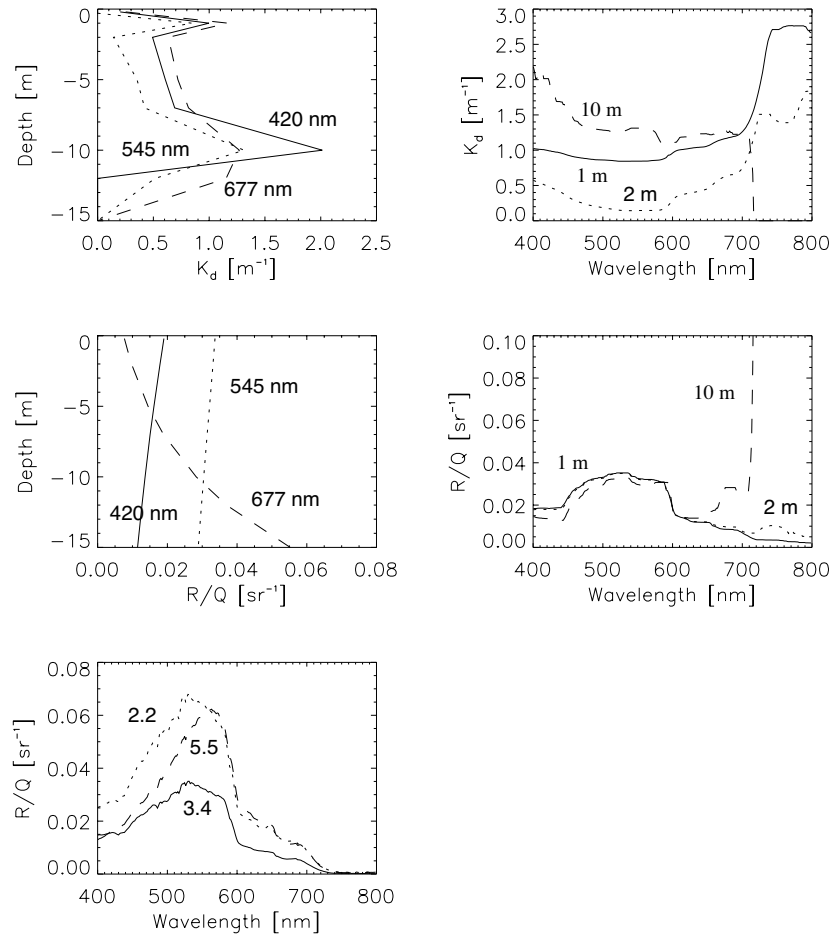


**Figure 3.8** Diffuse attenuation coefficient  $K_d$  and reflectance  $R/Q$  at 1, 2 and 10 m (top), for different wavelengths (centre), and for different stations in Lake Zürich with varying chlorophyll *a* concentrations [ $\mu\text{g l}^{-1}$ ] on August 26, 1998 (bottom).

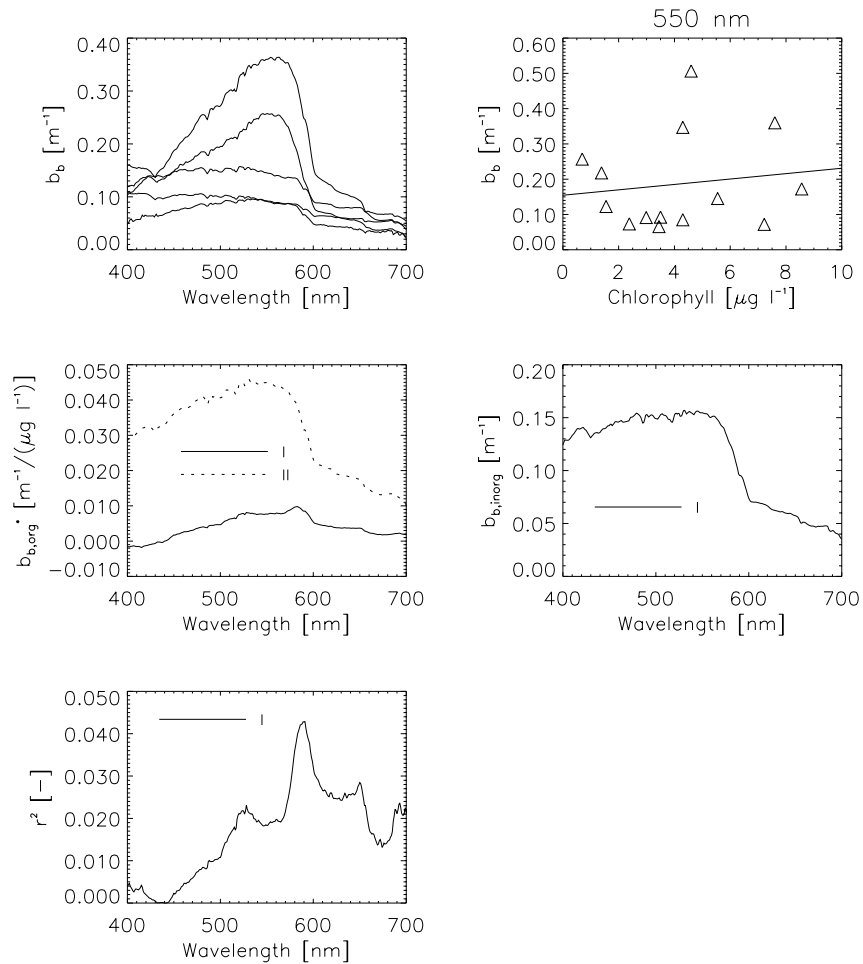


**Figure 3.9** Determined backscattering coefficient  $b_b$  based on GER1500 measurements for five different stations (top left). The case studies are summarized in Tab. 3.4. An example fit is shown in the top right image. However, only weak correlations  $r^2$  between scattering coefficient  $b_b$  and chlorophyll  $a$  concentration could be found leading to ambiguous organic ( $b_{b,org}$ ) and inorganic ( $b_{b,inorg}$ ) scattering values.

As shown in Fig. 3.9 and Fig. 3.10, the dependence of the calculated backscattering and absorption coefficients on chlorophyll  $a$  were ambiguous due to the high variations of the determined coefficients, the small *CHL* gradients and the low number of data points. Consequently, the application of

Eq. 3.8 and Eq. 3.10 yielded only low correlations coefficients. This confirms that inland waters have highly variable constituents which are strongly influenced by inorganic and non-living organic material, rendering optical remote-sensing a demanding task.

However again, the spectral signature of the determined total backscattering coefficient is similar to the calculated values using Mie theory (Fig. 2.18); this confirms the results obtained in the last chapter that both, the determination of the backscattering coefficient based on Mie calculations and radiometric *in situ* measurements represent well the actual situation.

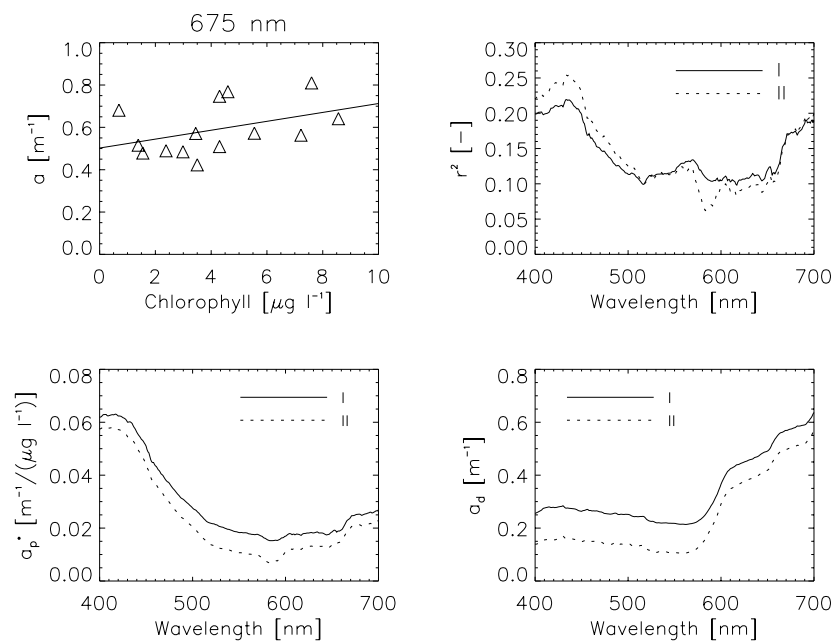
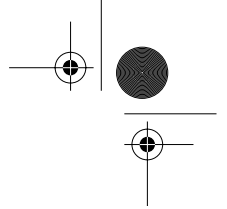


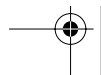
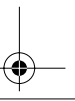
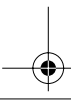
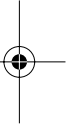
**Figure 3.10** Determined absorption coefficient  $a$  based on GER1500 measurements. An example fit is shown in the first image for case (I). The case studies are summarized in Tab. 3.5. Again, only low correlations could be found leading to ambiguous specific phytoplankton ( $a_p$ ) and detritus ( $a_d$ ) absorption values.

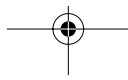


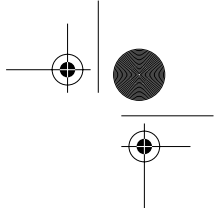
### 3.7 Conclusions

In Chapter 3, *in situ* measurement of radiometric quantities and their usefulness for the determination of inherent parameters are presented. The main results are:

- Radiometric measurements are often erroneous due to changing atmospheric conditions, air-water interface effects, influences by the boat used for sampling, self shading, and calibration problems mainly introduced by immersion effects and imperfect cosine receptor properties. The maximum errors due to calibration uncertainties are 7% for cosine collectors, and 3% for radiance measurements.
- Measurements above the air-water interface showed that in the lakes of interest, the water-leaving radiance above 750 nm usually can be neglected. This is an important prerequisite for the atmospheric correction presented in Chapter 4.
- Radiometric *in situ* measurements showed that lakes have highly variable constituents which are strongly influenced by non-living organic and inorganic material. Especially  $R/Q$  did not show a clear chlorophyll dependence, what of course has impacts on the retrieval of this parameter based on imaging spectrometer data. The results obtained for the backscattering coefficients confirm the findings in Chapter 2.5, where only weak correlations between particulate matter and chlorophyll *a* were found.
- The determined total backscattering coefficient based on Mie calculations (Chapter 2.10) and radiometric *in situ* measurements showed similar spectral signatures. This is remarkable as both methods are independent of each other. It can be concluded that the results of the two presented methods represent well the actual situation in the investigated waters.
- The influence of a non-uniform vertical distribution on the water-leaving radiance is only weak since the penetration depth of remote-sensing sensors is only 1 to 3 m in the investigated waters.





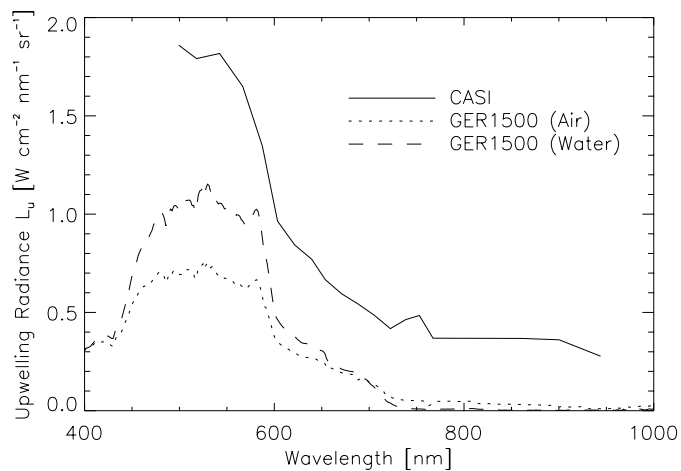


## Chapter 4

# Atmosphere and Air-Water Interface

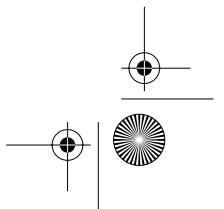
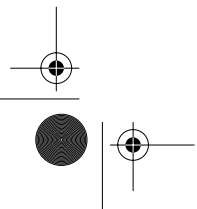
"...quand tout est bleu, le ciel est bleu,  
la montagne est bleue, l'eau est bleue..."  
Charles-Ferdinand Ramuz, *Passage du Poète*

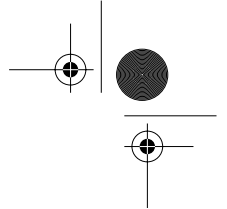
For the application of analytical inversion methods or for empirical methods which should be extrapolatable to different water types (i.e., various lakes and times), it is necessary to correct atmospheric and air-water interface effects which strongly influence the signal measured at a sensor (Fig. 4.1).



**Figure 4.1** Upwelling radiance measured by an airborne sensor (CASI, Lake Zug) and with a spectroradiometer (GER1500 DFOV system, Lake Zürich) above and below the water surface. The atmospheric path-scattered radiance leads to higher values measured by an airborne sensor compared to those directly measured above the interface. The radiance in the water is higher than above the interface due to the different refraction indices of air and water (see Chapter 4.6 and Chapter 4.7).

The theory describing atmospheric effects and a possible inversion method are outlined in the first part of this chapter. It will mainly follow the theory





given in the manual of ATCOR 4 (Richter, 1999) because this model builds the basis of the algorithm developed in this study. In the second part, air-water interface effects are treated and the implemented method correcting these effects is described.

#### 4.1 Atmospheric Radiative Transfer Code MODTRAN

There are different kinds of atmospheric correction models of which Schläpfer (1998) gives a short summary. Only the radiative transfer method will be discussed here, since it has some unique properties. It considers the angular dependence and the radiant path in the atmosphere; this is crucial for sensors (e.g., airborne) with a large field of view. Furthermore, it allows the simulation of the at-sensor radiance; this is important if the design of a new imager has to be tested (e.g., Börner et al., 2001).

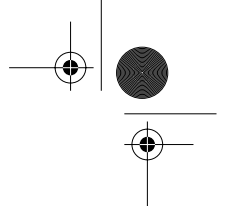
In this study, the atmospheric and air-water corrections are based on the radiative transfer code *Moderate Resolution Atmospheric Radiance and Transmittance Model* (MODTRAN) (Berk et al., 1989). The code calculates atmospheric transmittance and radiance for wave numbers from 0 to 50'000  $\text{cm}^{-1}$  at a spectral resolution of primarily 2  $\text{cm}^{-1}$  (20  $\text{cm}^{-1}$  in the UV).

For the determination of the model, various parameters have to be set. Here, not all of them are described, but only those having strong impacts on the modelling results: the atmospheric model, the aerosol model, and the visibility or meteorological range, respectively.

The *atmospheric model* describes the vertical temperature profile, the atmospheric pressure, and the vertical distribution of the atmospheric gaseous constituents. In the visible part of the spectrum, the main influences on the signature are prominent in the water vapour and ozone absorption bands. If these bands are not included in the inversion, the influence of the atmosphere can generally be neglected. The most relevant models for this particular analysis are (i.e., relevant for Switzerland in summer time when all measurements were performed): (i) midlatitude summer – normally the best choice in our climate zone, (ii) US-standard – drier atmosphere than (i).

The *aerosol model* determines the scattering and absorption properties of the aerosols. The influence on the spectrum is stronger in the “blue” region of the spectrum. Relevant models are: (i) rural – the best choice for rural regions or for urban regions with non-polluted air, (ii) urban – best model for industrial areas or polluted air extending in rural regions.

The *visibility* is a measure for the aerosol concentration in the atmosphere. It is operationally defined as the maximum horizontal distance at which two



targets can be distinguished by a human observer. Of course, the determination of this parameter is not strictly objective. The estimated values depend on the observer's visual acuity, but also on the viewing direction; lower values are reported when looking towards the sun due to the strong forward scattered radiation, whereas too high visibilities are observed when looking away from the sun. However, more objective determinations are possible using physical measurements. If the visibility is defined quantitatively, the term *meteorological range VIS* is used. In MODTRAN, *VIS* is defined by the Koschmieder formula (Berk et al., 1989):

$$s \cdot k(550\text{nm}) \equiv \frac{3.912}{VIS} - b_{Ray}(550\text{nm}) \equiv b_{ext}(550\text{nm}), \quad (4.1)$$

where  $s$  is the aerosol concentration at the surface,  $k$  the specific attenuation coefficient,  $b_{Ray}$  the Rayleigh scattering coefficient ( $\approx 0.012 \text{ km}^{-1}$ ), and  $b_{ext}$  the aerosol attenuation at the surface. The specific attenuation coefficient is by definition equal to 1 at 550 nm for all models; this implies that at 550 nm the aerosol attenuation is only determined by the meteorological range. The sensitivity to the quantities determined by MODTRAN is high for low visibilities (<25 km) and the determination of this parameter is therefore crucial for less clear atmospheric conditions. If only the observer visibility  $VIS_{obs}$  is available, the meteorological range *VIS* can be estimated as:

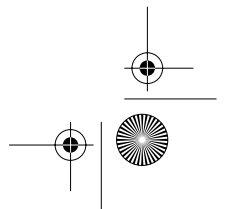
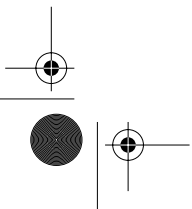
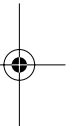
$$VIS = (1.3 \pm 0.3) \cdot VIS_{obs}. \quad (4.2)$$

## 4.2 Introduction to ATCOR 4

ATCOR 4 is a computer program designed for the atmospheric correction of airborne imaging spectrometer data, developed by Richter (1999) for reflective and thermal bands<sup>1)</sup>. The original algorithm allows the consideration of the external ( $x, y, z$ ) and internal (roll, pitch, yaw) orientation of the airplane; in the rewriting of the algorithms, this feature was not included in order to keep the code simple. ATCOR proposes an adjacency correction that is also presented here.

According to Kaufman and Sendra (1988), the monochromatic radiative transfer equation can be written as (Fig. 4.2):

<sup>1)</sup> The correction for the latter region is not presented, as this part of the spectrum was not used in the analysis.



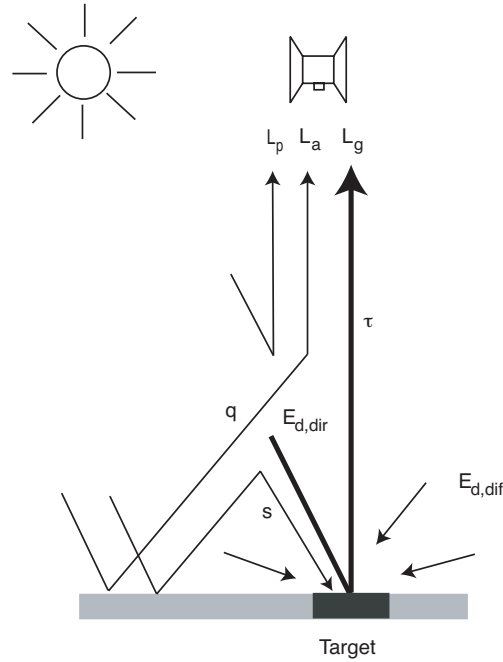


**Figure 4.2** Components contributing to the at-sensor radiance  $L_s$ , where  $L_p$  is the path radiance,  $L_a$  the adjacency radiance, and  $L_g$  the radiance containing information about the target pixel.  $E_{d,dir}$  and  $E_{d,dif}$  are the downwelling direct and diffuse irradiance on the ground, respectively,  $q$  the ratio of direct and diffuse transmittance at the sensor which determines the adjacency effect,  $s$  the spherical albedo of the atmosphere, and  $\tau$  the total (direct and diffuse) ground-to-sensor transmittance.

$$L_s(\lambda) = L_p(\lambda) + \frac{\rho(\lambda)}{\pi} \tau(\lambda) E_d(\lambda, \rho_r(\lambda)) \quad [\text{W m}^{-2} \text{sr}^{-1} \text{nm}^{-1}], \quad (4.3)$$

where  $L_s$  is the at-sensor radiance for the surface reflectance  $\rho$  [-],  $L_p$  [ $\text{W m}^{-2} \text{sr}^{-1} \text{nm}^{-1}$ ] the path radiance,  $\tau$  [-] the total (direct and diffuse) ground-to-sensor transmittance,  $\rho_r$  [-] the reference background reflectance, and  $E_d$  [ $\text{W m}^{-2} \text{nm}^{-1}$ ] is the total downwelling irradiance (i.e., the sum of direct  $E_{d,dir}$  and diffuse  $E_{d,dif}$  irradiance).

The surface reflectance  $\rho$  is defined by:

$$\rho(\lambda) \equiv \frac{\pi L_u(\lambda)}{E_d(\lambda)} \quad [-]. \quad (4.4)$$

The monochromatic equation has to be resampled with the spectral response functions of the sensor. Assuming constant reflectance in the scope of the response function  $RSP^i$  of each channel  $i$ , we can write:

$$L_s^i = L_p^i + \frac{\rho}{\pi} (E_{t, dir}^i + E_{t, dif}^i) \quad [\text{W m}^{-2} \text{sr}^{-1} \text{nm}^{-1}], \quad (4.5)$$

with

$$L_s^i = \frac{\int_{\lambda_1}^{\lambda_2} L_s(\lambda) RSP^i(\lambda) d\lambda}{\int_{\lambda_1}^{\lambda_2} RSP^i(\lambda) d\lambda} \quad [\text{W m}^{-2} \text{sr}^{-1} \text{nm}^{-1}], \quad (4.6)$$

$$L_p^i = \frac{\int_{\lambda_1}^{\lambda_2} L_p(\lambda) RSP^i(\lambda) d\lambda}{\int_{\lambda_1}^{\lambda_2} RSP^i(\lambda) d\lambda} \quad [\text{W m}^{-2} \text{sr}^{-1} \text{nm}^{-1}], \quad (4.7)$$

$$E_{t, dir}^i = \frac{\int_{\lambda_1}^{\lambda_2} \tau(\lambda) E_{d, dir}(\lambda) RSP^i(\lambda) d\lambda}{\int_{\lambda_1}^{\lambda_2} RSP^i(\lambda) d\lambda} \quad [\text{W m}^{-2} \text{nm}^{-1}], \quad (4.8)$$

$$E_{t,dif}^i = \frac{\int_{\lambda_1}^{\lambda_2} \tau(\lambda) E_{d,dif}(\lambda) RSP^i(\lambda) d\lambda}{\int_{\lambda_1}^{\lambda_2} RSP^i(\lambda) d\lambda} \quad [\text{W m}^{-2} \text{ nm}^{-1}]. \quad (4.9)$$

The broader  $RSP^i(\lambda)$ , the larger is the introduced error caused by the assumption of constant reflectance. For water applications, this is critical at the chlorophyll *a* absorption maxima at 440 nm and 670 nm.

The reflectances  $\rho$  and  $\rho_r$  are not known before the correction and must therefore be determined iteratively. The correction involves three steps. First, Eq. 4.5 is solved for  $\rho$  by neglecting the influence of the adjacency effect:

$$\rho^{(1)} = \frac{\pi \cdot (d^2 L_p^i - L_p^i)}{\tau \cdot (E_{t,dif}^i(\rho_r = 0.15) + E_{t,dif}^i(\rho_r = 0.15))} \quad [-], \quad (4.10)$$

where  $E_{t,dif}^i$  and  $E_{t,dif}^i$  are evaluated for a reference background  $\rho_r = 0.15$ . The parameter  $d$  [-] is the sun-earth distance (astronomical units) for the date of image acquisition given by:

$$d = 1 + 0.0167 \cdot \sin\left(\frac{2\pi \cdot (doy - 93.5)}{365}\right), \quad (4.11)$$

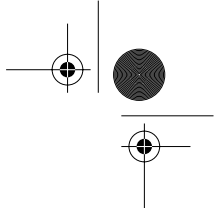
where *doy* is the Julian day of year. The factor  $d^2$  scales the measured signal since path radiance and the global flux are calculated for  $d = 1$ .

Secondly, the adjacency effects are corrected. The exact calculation of the adjacency radiation is too complex and uses too much computation time. In general each pixel is corrected with respect to the reflectances of the adjacent pixels (Richter, 1996):

$$\rho^{(2)} = \rho^{(1)} + q(\rho^{(1)} - \langle \rho \rangle). \quad (4.12)$$

The function  $q$  is the ratio of the diffuse and the direct transmittance at the sensor. Richter (1996) suggests a simple average of a defined region around the centre pixel. The adjacency effect is discussed in more detail in Chapter 4.4.

Thirdly, the atmospheric albedo of the total downwelling irradiance is included, initially calculated for  $\rho_r = 0.15$ . The correction is performed with the difference  $\langle \rho \rangle - \rho_r$ :



$$\rho^{(3)} = \rho^{(2)} + [1 + s(\langle \rho \rangle - \rho_r)], \quad (4.13)$$

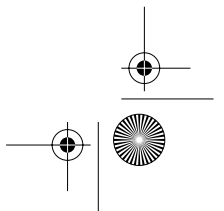
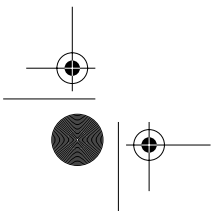
where the spherical albedo of the atmosphere  $s$  [-] accounts for atmospheric backscattering to the ground.

ATCOR 4 is divided into three main program modules. The module ATLUT organizes and calculates all terms of Eq. 4.10 including  $s$ , and the diffuse and direct transmittance for the determination of  $q$ . Since the diffuse and direct transmittances are stored, it is also possible to use the LUT for the calculation of the at-ground flux which will be used for the calculation of the air-water interface transfer equations (Chapter 4.7). The model RESLUT performs the resampling according Eq. 4.6 - Eq. 4.8, and finally, the module ATCOR determines the reflectance following Eq. 4.10 - Eq. 4.13.

All calculations are made with the DISORT option of MODTRAN using 8 streams. For the calculations of the terms, environmental parameters (ground altitude, sun azimuth and zenith angle), flight parameters (flight altitude and heading of the aircraft), sensor specific parameters (centre wavelength, FWHM, view angle) and atmospheric parameters (meteorological range, atmospheric and aerosol model) are needed.

### 4.3 At-Sensor Radiance

In order to give a first insight in the physical mechanisms, MODTRAN modelling is used to show how the at-sensor radiance depends on meteorological range  $VIS$  and ground reflectance (Fig. 4.3).



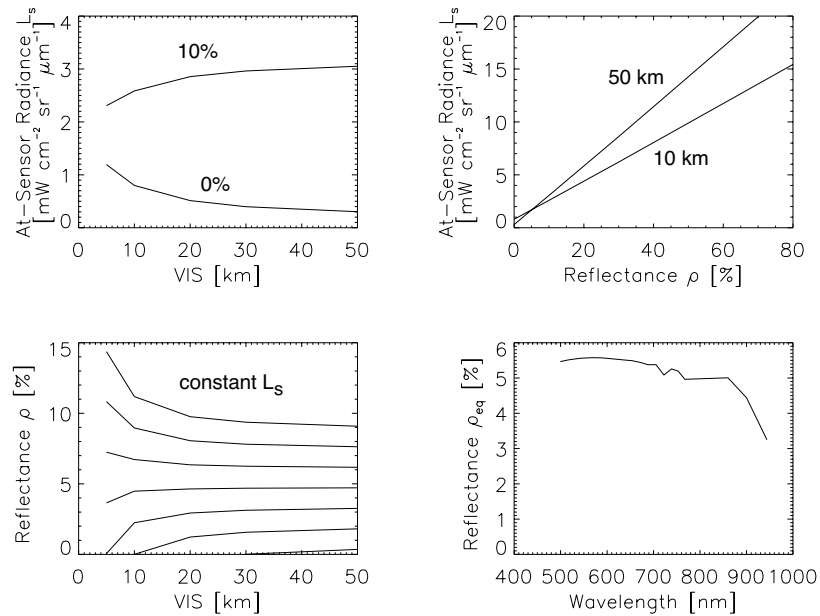


**Figure 4.3** Influence of the ground reflectance and the meteorological range  $VIS$  on the at-sensor radiance at 670 nm. Top figures: the at-sensor radiance as a function of the ground reflectance (0%, 10%) and  $VIS$  (10 km, 50 km). Bottom left: the reflectance  $\rho$  for variable  $VIS$  and constant  $L_s$ . Bottom right: reflectances where  $VIS$  does not influence the at-sensor radiance ( $\rho_{eq}$ ). All simulations were performed with the midlatitude summer model and rural aerosols.

The results show that a cleaner atmosphere (i.e., high visibility) does not automatically result in higher  $L_s$ , as it would be expected because the signal from the ground is less affected by atmospheric effects. However, the modelling shows that this is only true for high ground reflectances. In case of low reflectance, the path scattered radiance becomes the most important term, and consequently, the cleaner the atmosphere, the lower the signal at the sensor. It follows that there must be a reflectance level  $\rho_{eq}$  for each wavelength where  $VIS$  does not influence  $L_s$  any more; the further away the reflectance from  $\rho_{eq}$ , the more important is the determination of the visibility.

#### 4.4 Adjacency Effects

The adjacency radiance  $L_{adj}$  becomes important if adjacent pixels strongly differ in brightness (Kaufman, 1989, Tanré et al., 1987, Proy, 1989). Fig. 4.4 shows two possible optical paths that lead to this effect.

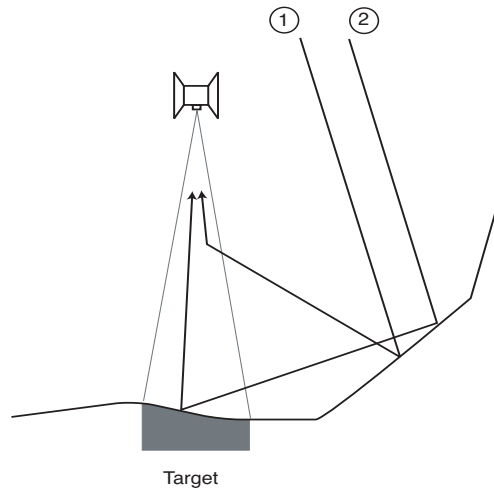


**Figure 4.4** Contributions to the adjacency effect: 1) radiation that reaches the adjacency of the target pixel but not the target itself, 2) radiation that reaches the adjacent region and the target pixel. Multiple scattering in the atmosphere or multiple reflections on the ground may occur, but were not shown in this figure.

The effects are a function of different variables:

- *Reflectances*. Because in the near-infrared, water has low and vegetation high reflectances, adjacency effects often occur in coastal areas, resulting in too high signals over the lake (Fig. 4.5).
- *Atmospheric aerosols*. The higher the aerosol concentration, the larger the atmospheric scattering and the more pronounced the adjacency effects. The scattering is higher for low wavelength, and adjacency effects can be neglected for wavelengths above  $1 \mu\text{m}$  (Tanré et al., 1987; Richter, 1990).
- *Recording geometry*. An increase of the sensor flight altitude<sup>1)</sup> or a decrease of the sun zenith angle leads to a longer path through the atmosphere and therefore to more intense adjacency effects.
- *Distance*. The distance between target and adjacent region influences the

<sup>1)</sup> This effect is limited within the earth's atmosphere.

adjacency effect. Richter (1990) found a relevant distance of 100 to 500 m, Kaufman (1989) a distance of 1 to 2 km. The aerosol concentration influences this distance. If the concentration is high, then the influence of nearby pixels is more important. If the concentration is low, then more remotely situated pixels become relatively more important. For a pure Rayleigh atmosphere, the adjacency effects are noticeable at a horizontal distance of up to 10 km (Deschamps et al., 1980).

- *Slope and Aspect.* The topographic orientation of the adjacent pixels and of the target pixel influence the size of the adjacency effects. In the analysis, the bidirectional distribution function (BRDF) of the reflectance must be considered.

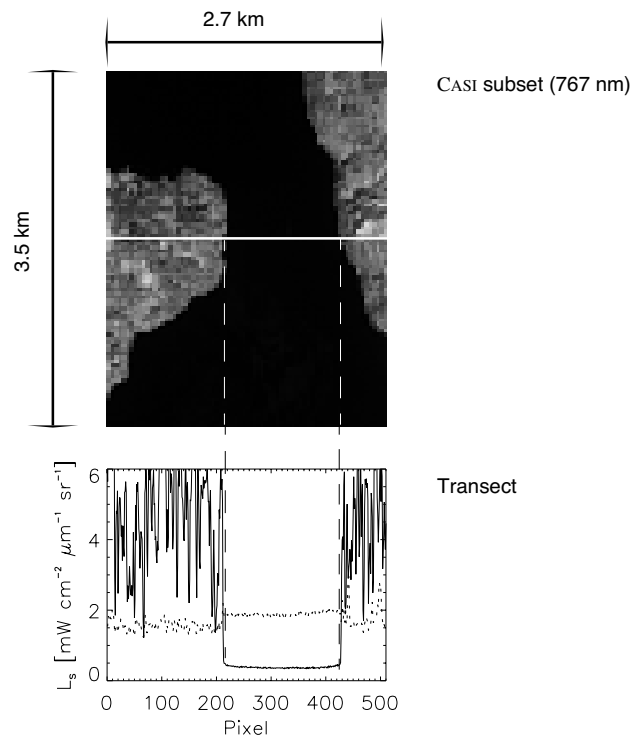
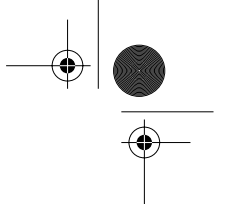


**Figure 4.5** Transect of the CASI scene (dotted: 518 nm, solid: 767 nm). One pixel corresponds to 5.3 m. Although adjacency effects are expected to be stronger in the visible part of the spectrum due to Rayleigh scattering, they occur mainly in the near-infrared due to large reflectance differences between land vegetation and water. More information about the image data can be found in Chapter 5.2.



## 4.4 Adjacency Effects

91

As mentioned above, Richter (1996) suggests a simple average of a defined region around the centre pixel for the correction for the adjacency effect. Vermote et al. (1994) define a spatial weighting function used in the atmospheric correction program 6S. Considering a circular target of radius  $r$  and reflectance  $\rho_c$  surrounded by homogenous surface of reflectance  $\rho_r$ , the weighted average reflectance is given by:

$$\langle \rho \rangle = F(r)\rho_c + (1 - F(r))\rho_r \quad [-], \quad (4.14)$$

where  $F(r)$  determines the relative contribution of surface points not further than the distance  $r$  [km] away from the origin. This filter depends on wavelength, viewing angle, sensor altitude, sun zenith angle, scattering properties of the atmosphere, and distance to the centre pixel. Vermote et al. determined filter functions for Rayleigh scattering  $F^r(r)$  and aerosol scattering  $F^a(r)$  by Monte Carlo simulations. For satellites, they are given by:

$$F^a(r) = 1 - (0.375 \cdot \exp(-0.20r) + 0.625 \cdot \exp(-1.83r)) \quad [-] \quad (4.15)$$

and

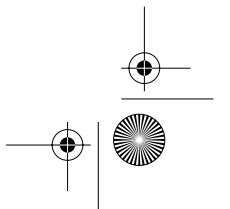
$$F^r(r) = 1 - (0.930 \cdot \exp(-0.08r) + 0.070 \cdot \exp(-1.10r)) \quad [-]. \quad (4.16)$$

For airborne sensors, these filter functions have to be adjusted with a look-up table given in the atmospheric correction program 6S. These filter functions were weighted with their corresponding diffuse transmittance,  $\tau_d^r$  and  $\tau_d^a$ , from the target to the sensor resulting in  $F(r)$ <sup>1)</sup>:

$$F(r) = \frac{\tau_d^r F^r(r) + \tau_d^a F^a(r)}{\tau_d^r + \tau_d^a} \quad [-]. \quad (4.17)$$

Fig. 4.6 shows the results of such a simulation of the weighting function for the 1997 CASI campaign over Lake Zug. The sensor flew 3.7 km above the lake. For the understanding of the behaviour of Eq. 4.17, the dependence of  $\tau_d^r / (\tau_d^r + \tau_d^a)$  on the meteorological range  $VIS$  and wavelength  $\lambda$  must be considered. The higher  $VIS$  and the lower  $\lambda$ , the larger becomes this ratio. At long wavelengths, the ratio is equal to zero and  $F(r)$  corresponds

<sup>1)</sup> The MODTRAN output does not include information about Rayleigh and aerosol scattering but information on the sum of both contributions. However, the Rayleigh scattering can accurately be determined for specific atmospheric compositions, if the calculations are performed for high visibilities (i.e. > 150 km). Slightly better results can be obtained if the calculations are done for at least two high visibilities, and if these results are plotted against  $1/VIS$ . Rayleigh scattering is then equal to the extrapolated values at  $1/VIS = 0$ .



approximately to the aerosol filter function  $F^a(r)$ .

Of course, this modelling does not include all relevant factors described above; especially the topographic orientation is not treated in our considerations. However, it clearly explains the wavelength dependence of the adjacency effect occurring in imaging spectroscopy data.

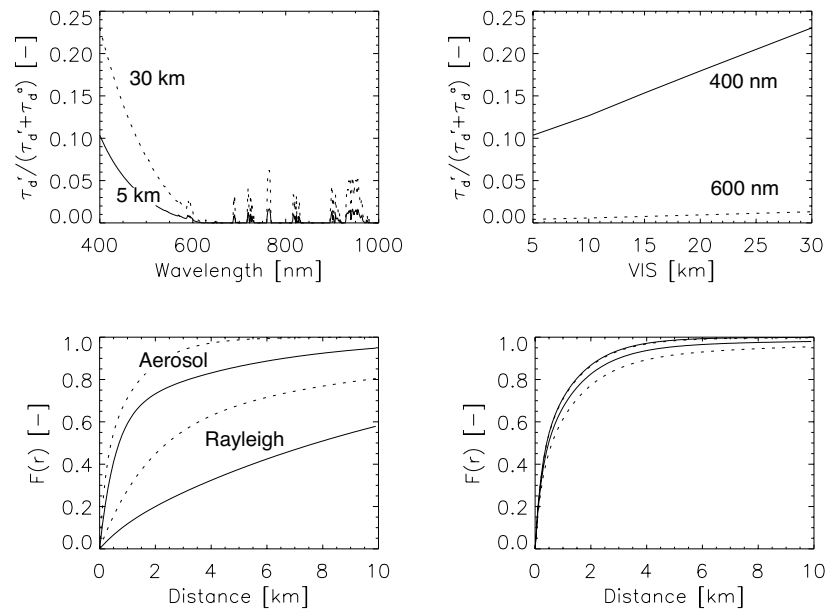
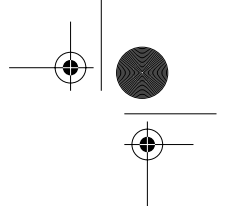


**Figure 4.6** Calculation of the environmental weighting function for an airborne sensor 3.7 km above ground, performed for the US-Standard atmosphere with urban aerosols. Top left: ratio of Rayleigh transmittance to total transmittance as a function of wavelength. Top right: ratio of Rayleigh transmittance to total transmittance as a function of meteorological range  $VIS$ . Bottom left: filter functions for Rayleigh and aerosol scattering for a sensor 3.7 km above ground (solid) and for a satellite (dotted). Bottom right: environmental weighting function  $F(r)$  for an airborne sensor as a function of the distance to the origin, the wavelength (upper two lines: 400 nm, lower two lines: 600 nm), and the meteorological range  $VIS$  (solid: 5 km, dotted: 30 km).

#### 4.5 Experimental Determination of Adjacency Effects

In this experiment the adjacency effects were evaluated using a GER3700 field spectrometer (Appendix A) mounted on a helicopter (Schaeppman et al.,



1997; Cathomen, 1997). The measurements were performed over Lake Zug on September 25, 1996.

The same transect was flown at eleven different altitudes ranging from 100 m to 1800 m above the lake. At the same time, different limnological parameters (chlorophyll *a*, *DOC*, Secchi depth, and spectral measurements with the LI-COR radiometer) were measured from two boats. For the monitoring of the atmosphere, a REAGAN sun photometer was used (Appendix A)<sup>1)</sup>. The calibration of the spectroradiometer was performed using a SPECTRALON reference panel located next to the sun photometer. Before, during, and after the helicopter flight, the panel was being measured with the radiometer still mounted on the helicopter.

The main goal of this experiment, the determination of the adjacency effects, was not obtained, mainly due to the large ground sampling distance and the limited flight altitude. On the eastern lake border, the measurements did not show any significant contribution of the expected adjacency effect and on the western end, only a slightly higher value for the 1800 m transect at a distance of 300 m from the lake border was observed. Of course, modellings as presented in Chapter 4.4 could serve as an aid for a better experimental design.

## 4.6 Air-Water Interface Processes

Refraction and reflection must be taken into account when radiation enters and leaves the water body. Snell's law provides the relationship between angles and indices of refraction, if a harmonic wave crosses the plane interface between two media:

$$n_a(\lambda) \sin \theta_a = n_w(\lambda) \sin \theta_w \quad [-], \quad (4.18)$$

where  $\theta_a$  and  $\theta_w$  are the incident zenith angles in air and water, respectively. The refraction of air  $n_a$  is taken as unity, and the relative index of refraction of water  $n_w$  is generally taken as 1.34 for the visible part of the spectrum (see Chapter 2.6). Snell's law explains why the upwelling radiance in water is higher than in air (Fig. 4.1): The air-incident radiance is focused into a smaller solid angle, whereas the water-incident radiance is spread into a wider solid angle in accordance with the reciprocity principle. Total reflectance occurs for air-incident rays at 90°, whereas for water-incident rays total reflection already occurs at 48°. This angle is given by Snell's law with

<sup>1)</sup> The usefulness of such measurements will be demonstrated in Chapter 5.4.

$\theta_a = 90^\circ$ . Consequently, the whole above-water atmospheric hemisphere is projected in an underwater cone with a solid angle of  $2 \times 48^\circ = 96^\circ$ .

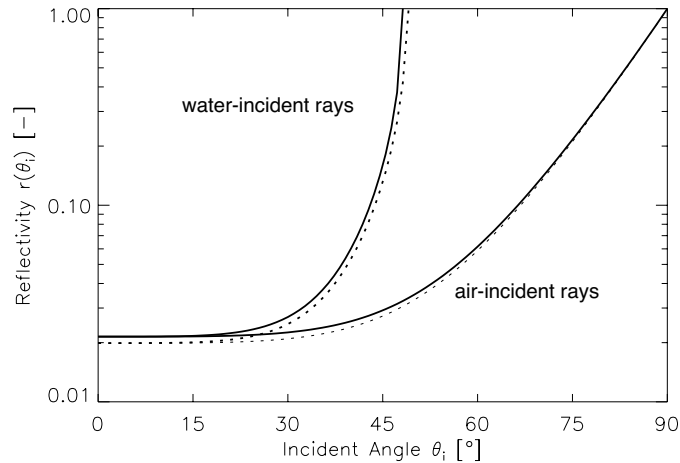


**Figure 4.7** Fresnel reflectivity of water and air incident rays, respectively (solid: 400 nm, dotted: 800 nm). Water-incident and air-incident means that the rays cross the interface from the water or air side, respectively.

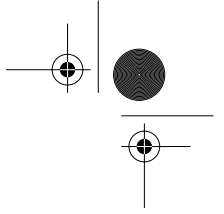
Fresnel's formula calculates the reflectivity<sup>1)</sup>  $r$  of a flat air-water surface for given zenith angles of incidence and refraction,  $\theta_i$  and  $\theta_r$ . In case of unpolarized incident radiant energy, this is given by:

$$r(\theta_i, \lambda) = 0.5 \left( \frac{\sin(\theta_i(\lambda) - \theta_r(\lambda))}{\sin(\theta_i(\lambda) + \theta_r(\lambda))} \right)^2 + 0.5 \left( \frac{\tan(\theta_i(\lambda) - \theta_r(\lambda))}{\tan(\theta_i(\lambda) + \theta_r(\lambda))} \right)^2 \quad [-]. \quad (4.19)$$

The reflectivity is mainly a function of the incident angle  $\theta_i$  and only weakly dependent on the wavelength  $\lambda$  as illustrated in Fig. 4.7 for water- and air-incident cases.

In case of zero absorption<sup>2)</sup>, the relative rates of refracted and reflected radiation add up to 1. Although the transfer of a single light beam is theoretically determined, the correction for the effects at the interface is

- 1) The term *reflectivity* is used for the discrimination to the term *reflectance* defined in Chapter 2.1. Sometimes also the term *specular reflectance* is used to discriminate it from the "normal" reflectance.
- 2) This can be assumed for radiation of low irradiances and of low photon energies. See discussion in Mobley (1994).



difficult to carry out in practice. A first difficulty comes with the determination of the transfer function of the downwelling and upwelling irradiance, because the radiance distribution in the hemisphere is generally unknown. A second difficulty arises from direct sun reflection at the water surface which depends on the recording geometry and the wave slope and which therefore may be variable within a scene; this phenomenon is usually called sun *glint* or *glitter*. Despite these problems, it is possible to describe the air-water interface processes as we will see in the following sections.

#### 4.7 Air-Water Interface Transfer Equations

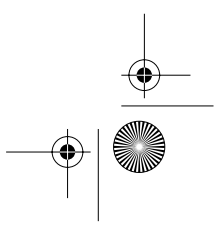
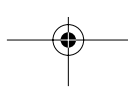
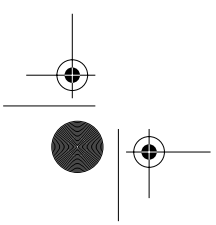
The air-water interface transfer can be summarized with (Mobley, 1994):

$$\frac{\rho(a, \xi)}{\pi} \equiv \frac{L_u(a, \xi)}{E_d(a)} = R_{R_s}(a, \xi) + r(a \rightarrow w, \xi) \quad [\text{sr}^{-1}]. \quad (4.20)$$

The remote-sensing reflectance  $R_{R_s}$  is given by (Eq. 2.7):

$$R_{R_s}(a, \xi) \equiv \frac{L_w(a, \xi)}{E_d(a, \xi)} = \frac{t(a \rightarrow w)t(w \rightarrow a, \xi' \rightarrow \xi)R(w)}{n_w^2(1 - R(w)r(w \rightarrow a))} \frac{Q}{Q} \quad [\text{sr}^{-1}], \quad (4.21)$$

where  $L_w$  is the water-leaving radiance. Eq. 4.20 takes into account (Fig. 4.8) the surface reflection of downwelling irradiance  $r(a \rightarrow w, \xi)$ , the transfer of the downwelling irradiance in the waterbody  $t(a \rightarrow w)$ , the internal reflection of the upwelling radiance at the interface  $r(w \rightarrow a)$ , and the transfer of upwelling radiance across the interface  $t(w \rightarrow a, \xi' \rightarrow \xi)/n_w^2$ . The first term in brackets describes the origin of the radiation ( $a = \text{air}$ ,  $w = \text{water}$ ), the second term where the radiation is pointing to,  $\xi$  is the viewing zenith angle in air, and  $\xi'$  the corresponding angle in water.



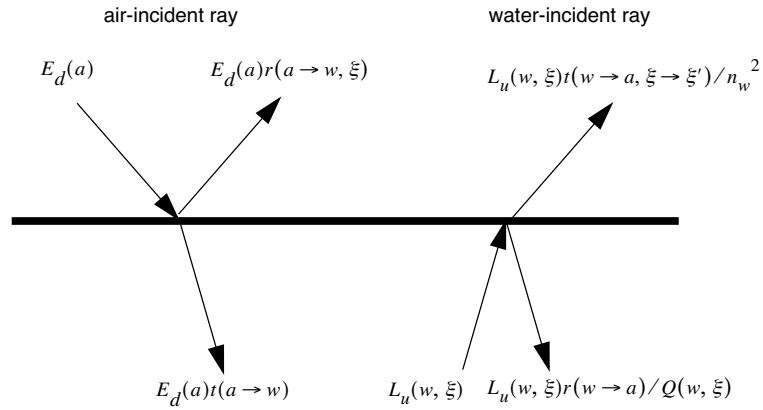


**Figure 4.8** Radiation transfer at the air-water interface. The definition of the transfer functions are given in the text.

The description of the transfer functions of the *downwelling* radiation is done after Bukata et al. (1995) who distinguish different transfer functions for sunlight and diffuse skylight.

The *surface reflection* is expressed as:

$$r(a \rightarrow w, \xi) = (1 - \beta)f_1 + \beta f_2 \text{ [sr}^{-1}\text{]}, \quad (4.22)$$

where  $\beta$  is the ratio of the direct sunlight to the total irradiance,  $f_1$  and  $f_2$  are the ratios of diffuse skylight and direct sunlight which are reflected at the air-water surface, respectively.

The *transfer function of the downwelling irradiance* is given as:

$$t(a \rightarrow w) = (1 - \beta)f_3 - \beta f_4 \text{ [-]}. \quad (4.23)$$

$f_3$  and  $f_4$  are the ratios of diffuse skylight and direct sunlight that enter the water body. The factors  $f_i$  are described in detail in Tab. 4.1.

## 4.7 Air-Water Interface Transfer Equations

**Table 4.1** Transfer functions for downwelling radiation (Bukata et al., 1995).

$f_1 = \alpha r_0 + \gamma_1$ [sr <sup>-1</sup> ]	(4.24)	Diffuse surface reflection function
with		
$\alpha \equiv L_{sky}(\lambda, 0^\circ)/E_{sky}(\lambda)$ [sr <sup>-1</sup> ]		Ratio of downwelling zenith sky radiance to downwelling sky irradiance
$r_0$ [-]		Fresnel reflectivity for vertical incidence
$\gamma_1$ [sr <sup>-1</sup> ]		Fraction of sky radiance reflected by surface waves (can be neglected for wind velocity $v_{wind}$ in the range 0 - 10 ms <sup>-1</sup> )
$f_2 = \frac{r(\xi) \exp(-\tan^2 \delta / S^2)}{4\pi S^2 \cos \xi \cos^4 \delta}$ [sr <sup>-1</sup> ]	(4.25)	Direct surface reflection (glitter) for viewing angle $\xi$ , Zenith angle of the direction normal to the surface $\delta$ (Eq. 4.30), and mean square wave slope angle $S^2$ (Eq. 4.29)
with		
$r(\xi)$ [-]		Fresnel reflectivity for viewing angle $\xi$
$f_3 = 1 - r_{sky} - \gamma_3$ [-]	(4.26)	Diffuse surface transfer function
with		
$r_{sky}$ [-]		Fresnel reflectivity of an uniformly diffuse sky irradiance from a flat air-water interface = 6.6% (Jerlov, 1976)
$\gamma_3$ [-]		Fraction of sky irradiance reflected by surface waves, e.g., for wind velocity $v_{wind} = 4$ ms <sup>-1</sup> , $\gamma_3 = -0.010$ and for $v_{wind} = 7$ ms <sup>-1</sup> , $\gamma_3 = -0.014$
$f_4 = r(\theta) \left\{ \begin{aligned} &1/2[1 + I(k)] \\ &+ \frac{1}{2\sqrt{\pi}} a S \cdot \exp(-k^2) \\ &+ \frac{1}{4} b S^2 [1 + I(k) - 2\pi^{-1/2} k \cdot \exp(-k^2)] \\ &+ \frac{1}{4} c S^2 [1 + I(k)] \\ &+ \dots \end{aligned} \right\}$ [-]	(4.27)	Direct surface transfer function for mean square wave slope angle $S^2$ (Eq. 4.29) (Cox and Munk, 1955)

**Table 4.1** Transfer functions for downwelling radiation (Bukata et al., 1995). (Continued)

with

$$r(\theta) \text{ [-]}$$

Fresnel reflectivity of direct solar irradiance from a flat air-water interface for solar zenith angle  $\theta$ 

$$k \equiv \cot(\theta)/2S \text{ [-]}$$

$$I(k) \equiv 2\pi^{-1/2} \int_0^k \exp(-t^2) dt \text{ [-]}$$

Error integral

$$F \equiv \rho(\theta) \cos \theta \text{ [-]}$$

$$a \equiv \left. \frac{1}{F} \frac{dF}{d\theta} \right|_{\theta} \text{ [-]}, \quad b \equiv \left. \frac{1}{2} + \frac{1}{2F} \frac{d^2F}{d\theta^2} \right|_{\theta} \text{ [-]},$$

$$c \equiv \left. \frac{1}{2} + \frac{\cot\theta}{2F} \frac{dF}{d\theta} \right|_{\theta} \text{ [-]}$$

The Fresnel reflectivities do not depend on the atmospheric conditions and are almost wavelength independent. However, the ratios  $\alpha$  and  $\beta$  show strong dependence on wavelength and meteorological range  $VIS$ , especially for  $VIS < 20$  km (Fig. 4.9); these terms must therefore be known accurately for adequate interface corrections. Note that  $\alpha$  would be equal to  $1/\pi = 0.34$  for an equally distributed radiance. The influence of the aerosol model on  $\alpha$  and  $\beta$  is only weak and can be neglected.

The wave slope distribution  $P$  is described by the isotropic Gaussian distribution. If the wind direction is not considered,  $P$  is defined as (Cox and Munk, 1954):

$$P \equiv \frac{1}{\pi S^2} \exp\left(-\frac{\tan^2 \delta}{S^2}\right) \text{ [-]}. \quad (4.28)$$

The mean square wave slope angle  $S^2$  is given by:

$$S^2 = 0.003 + 0.00512 \cdot v_{wind} \text{ [-]}, \quad (4.29)$$

where  $v_{wind}$  is the wind velocity given in  $[\text{ms}^{-1}]$  and  $S^1$  given in radians. This relation is only valid for steady state conditions and long wind fetch

<sup>1)</sup> Note that  $S^2$  is the variance and  $S$  the standard deviation of the variations of the wave slope angle. Consequently,  $S$  is the root mean square wave slope and not the mean wave slope which is zero.

## 4.7 Air-Water Interface Transfer Equations

distances. The zenith angle of the direction normal to the surface  $\delta$  is calculated as follows:

$$\cos(\delta) = \frac{(\cos(\theta_s) + \cos(\theta_v))^2}{1 + \cos(2\omega)} \quad [-], \quad (4.30)$$

with  $\omega$  given by:

$$\cos(2\omega) = \cos(\theta_s)\cos(\theta_v) + \sin(\theta_s)\sin(\theta_v)\cos(\phi_s - \phi_v) \quad [-], \quad (4.31)$$

where  $\theta_s$  and  $\theta_v$  are the sun and sensor viewing zenith angles,  $\phi_s$  and  $\phi_v$  the azimuth angles of the sun and sensor viewing direction, respectively.

Eq. 4.29 affects the factors  $f_2$  and  $f_4$  as stated in Tab. 4.1. The influence of the wind velocity on  $f_2$  is especially significant, whereas it is almost negligible for  $f_4$  (Fig. 4.10). However, the factor  $f_2$  is very small, so that it does not have to be considered<sup>1)</sup>. Note, that glitter introduced by boats is not included in these terms, neither is the influence of wave breaking or whitecaps.

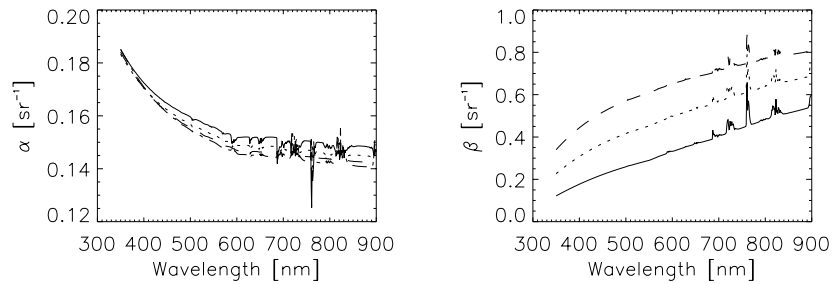


**Figure 4.9** The ratios  $\alpha = L_d(0^\circ)/E_d$  and  $\beta = E_{d,dif}/E_{d,tot}$  modelled with MODTRAN for rural aerosols, constant sun zenith angle ( $48^\circ$ ), and variable VIS (solid: 5 km, dotted: 10 km, dashed: 20 km).

<sup>1)</sup> This is only true if the sensor is flown in the solar principle plane (which is therefore usually the preferred heading); if the sensor flies perpendicular to this plane, strong glitter effects occur which can hardly be corrected for.

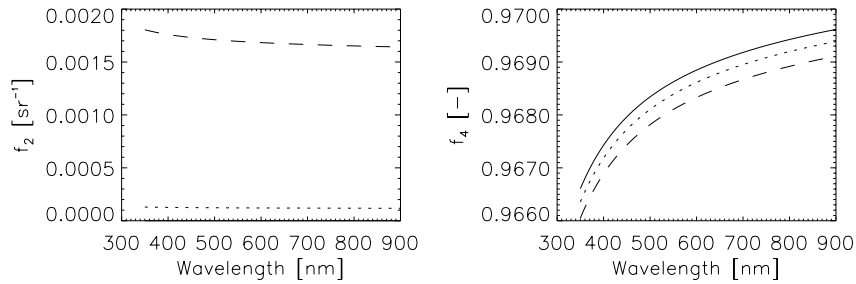


**Figure 4.10** Wind affected parameters for a sensor in the solar principle plane: surface glitter coefficient  $f_2$  and transfer coefficient  $f_4$  for constant sun zenith angle ( $48^\circ$ ) and variable wind velocity (solid:  $2 \text{ ms}^{-1}$ , dotted:  $5 \text{ ms}^{-1}$ , dashed:  $10 \text{ ms}^{-1}$ ). Note that for wind velocity =  $2 \text{ ms}^{-1}$ ,  $f_2$  is too small ( $< 10^{-7}$ ) to be visible in the diagram.

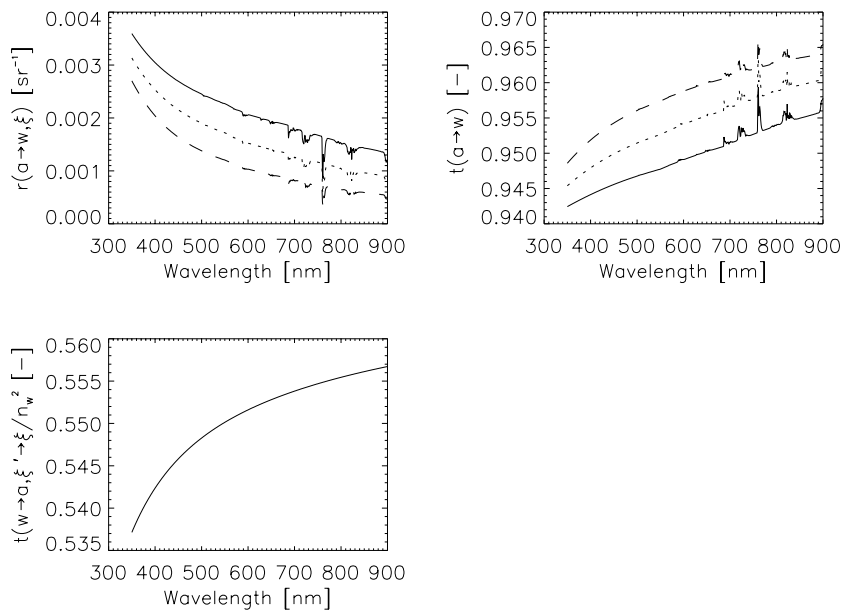
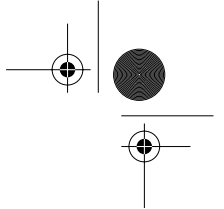


**Figure 4.11** Transfer functions for constant sun zenith angle ( $48^\circ$ ) and variable  $VIS$  (solid: 5 km, dotted: 10 km, dashed: 20 km). Note that  $t(w \rightarrow a, \xi' \rightarrow \xi)$  does not depend on the meteorological range  $VIS$ .



## 4.7 Air-Water Interface Transfer Equations

101

The *internal reflection*  $r(w \rightarrow a)$  is typically smaller than 0.7 (Mobley, 1994). However, its influencing can be neglected in the blue and red part of the spectrum as the reflectance  $R$  is almost zero, whereas in the green part this would lead to considerable errors.

And finally, the *transfer function of the upwelling radiance* is calculated by Mobley (1994):

$$t(w \rightarrow a, \xi' \rightarrow \xi)/n_w^2 = (1 - r(\xi'))/n_w^2 [-], \quad (4.32)$$

where  $r(\xi')$  is the Fresnel reflectivity for the upwelling radiance coming from  $\xi'$  and pointing in the direction of the viewing angle of the sensor  $\xi$ .

Fig. 4.11 shows the three relevant transfer coefficients as a function of wavelength and meteorological range. The most important conclusions of these modelling calculations are:

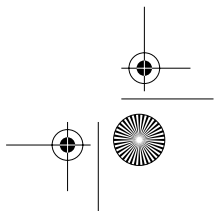
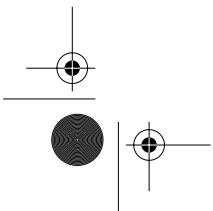
- The transfer functions  $t(a \rightarrow w)$ ,  $r(w \rightarrow a)$  (not shown), and  $t(w \rightarrow a, \xi' \rightarrow \xi)/n_w^2$  depend only weakly (or not at all) on wavelength and meteorological range; the variations are only about 1-2%. Thus, all three parameters can be assumed to be constant for the calculations. Good estimations for these parameters valid for non-extreme situations are:  $t(a \rightarrow w) = 0.955$ ,  $r(w \rightarrow a) = 0.7$ , and  $t(w \rightarrow a, \xi' \rightarrow \xi) = 0.98$ .
- On the other hand, the transfer function  $r(a \rightarrow w, \xi)$  significantly depends on both wavelength and meteorological range and is therefore crucial for the air-water interface correction. Note that the lower the meteorological range, the higher the surface reflection; this is caused by the higher amount of diffuse light and resulting larger average zenith angles which lead, according to Fresnel' law, to higher reflection (Fig. 4.7).

If we can presume that the water-leaving radiance is negligible (which is usually the case in the near-infrared due to the high water absorption), then Eq. 4.20 can be simplified to:

$$\rho(a, \xi)/\pi = r(a \rightarrow w, \xi) [\text{sr}^{-1}]. \quad (4.33)$$

The equation states that the remote-sensing reflectance is equal to the surface reflection, therefore independent of the water constituents, and only dependent on atmospheric parameters. This approach can be used for a pixel-wise determination of the meteorological range, as shown in Chapter 5.4.

More insight into the physics of radiation transfer at the air-water interface is given by Walker (1994) which treats the influence of the atmosphere, sea-surface statistics, sun glitter, and whitecaps in more detail.



## 4.8 Verification of the Transfer Equations

For a verification of the transfer equations, GER1500 measurements in Lake Zürich and Walensee are used. Re-writing Eq. 4.20, we obtain:

$$L_u(a) = E_d(a) \cdot \left( \frac{t(a \rightarrow w)t(w \rightarrow a, \xi' \rightarrow \xi)L_u(w)}{n_w^2(1 - R(w)r(w \rightarrow a))E_d(w)} + r(a \rightarrow w, \xi) \right). \quad (4.34)$$

$E_d(a)$ ,  $E_d(w)$ , and  $L_u(w)$  are quantities which can be measured by the GER1500 system. As the upwelling irradiance is not measured, we have to introduce  $Q(w, \xi) = L_u(w, \xi)/E_u(w)$  (see Eq. 2.5), which is estimated to be equal to 4.5. All other parameters were calculated using the equations given in Chapter 4.7.

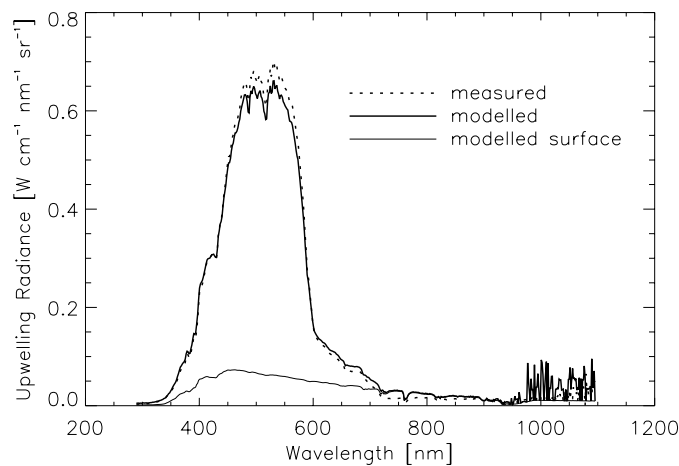
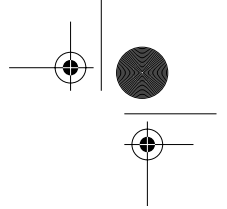


**Figure 4.12** Comparison of measured and modelled upwelling radiance above the air-water interface for a nadir looking instrument (Walensee, July 20, 1998). For the calculations, the meteorological range was set to 25 km. For a comparison, the surface reflected radiance without the water-leaving radiance is also shown ("modelled surface")

One randomly selected sample of Lake Zürich is shown in Fig. 4.12. As the measurements were performed at clear atmospheric conditions, the meteorological range was set to 25 km for the calculations<sup>1)</sup>. The agreement

<sup>1)</sup> It can be assumed that for such conditions, the exact value of  $VIS$  is not crucial for the quality of the results.



between measured and modelled  $L_u(w)$  is almost perfect. However, the achieved result is surprising as several uncertainties are contained in the model:

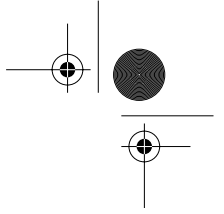
- the difficult measuring set-up on a boat,
- the inter-calibration between the two instruments,
- the immersion correction of the instruments (Chapter 3.2)
- the assumed value of  $Q(w, \xi)$ , and
- all the simplification made at the derivation of the transfer functions (Chapter 4.7).

For comparison, the surface reflected radiance is also shown in Fig. 4.12. As the water absorption is high in the near-infrared, the surface reflected radiance contributes only little to the total radiance, while in the visible part of the spectrum, the surface reflected radiance is about 10%. It is well understood, that this figures are only valid for plane surfaces which are unaffected by surface waves.

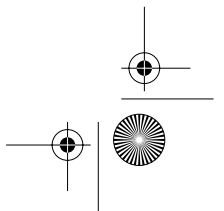
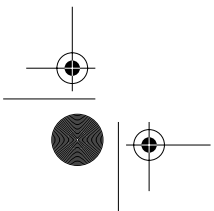
## 4.9 Conclusions

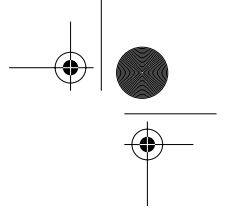
The pre-correction of image data is crucial for the determination of water constituents. In this chapter it is shown, how the various parameters needed for the atmospheric and air-water interface correction can be calculated. The conclusions drawn from this chapter are:

- The transfer equations allow an exact description of the air-water interface. They mainly depend on wind velocity, wavelength and meteorological range. By introducing transfer functions for downwelling irradiance and upwelling irradiance (i.e.,  $t(a \rightarrow w)$  and  $r(w \rightarrow a)$ ), the radiance distribution is not required. The transfer equations could be confirmed by radiometric measurements.
- For water types with only low particulate matter concentration, information in the near-infrared can be used for the determination of atmospheric parameters; this allows a pixel-wise determination of the meteorological range. Image-based methods have the advantage that inter-scene variation can be considered in the analysis.
- The determined reflectances are sensitive to the aerosol model. The atmospheric model mainly influences the reflectance at the absorption features of water vapour. If these regions of the spectrum are not included in the determination of water quality parameters, the choice of the atmosphere model is irrelevant.



- Adjacency effects have to be considered due to the small extension of lakes. Especially in the near-infrared, the influence of these effects on the at-sensor radiance is important due to the large differences between land vegetation and water reflectance.





## Chapter 5

# Imaging Spectroscopy

In this chapter, all steps needed for the determination of water constituents (see Chapter 1.1) were brought together and applied on image data, in order to investigate their impacts on the results.

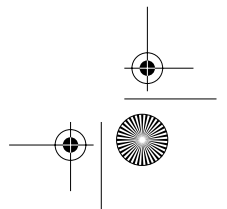
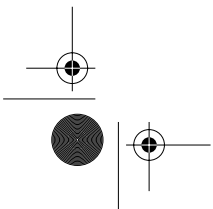
In the first section, a short introduction in imaging spectrometry is presented in order to give an outline of the technology behind the data. In the next section, the CASI campaign performed in the area of Lake Zug is presented. The data quality is tested with an image-based determination of the signal-to-noise ratio and a principal component analysis. It follows the application of the atmospheric and air-water interface correction. Finally, the determination of chlorophyll *a* and inorganic scattering coefficient is shown for different case studies.

### 5.1 Imaging Spectrometry

Imaging spectroscopy is the science of measuring and analysing data which are sampled by an imaging spectrometer, whereas imaging spectrometry is the science of measuring only. The definition of imaging spectrometry that distinguishes it from multispectral imaging is the acquisition of images in registered, contiguous spectral bands such that for each pixel, a complete radiance spectrum can be obtained. As the sensors have a large number of narrow bands, the term hyperspectral is also often used in this context.

All passive optical sensors operate on the same principles of optical radiation transfer and photon detection. Every pixel in an image represents an average in three dimensions: space ( $x, y$ ) and wavelength ( $\lambda$ ). Therefore, this three-dimensional continuous parameter space can be visualized with a data cube. The volume of integration represented by each pixel is a well-defined box, but may overlap in both spatial and spectral dimensions.

A digital data cube is achieved by a combination of scanning in the cross-track direction (perpendicular to the sensor motion) and of platform motion along the flight path direction. The most usual scanners are whisk-broom and push-broom scanners. *Whisk-broom scanners* use linear detector elements to achieve the parallel scanning of the entire spectrum of one ground element at a time. The image is obtained by rotation of a mirror at the entrance of the



sensor and by platform motion. *Push-broom scanners* have a two dimensional detector allowing a simultaneous scan of the spectrum of all pixels of one row; the third dimension again is obtained by platform motion. Fig. 5.1 illustrates these two widely used systems. Detectors consist of charge coupled devices (CCD) transforming radiation energy into electric potential. An analog-to-digital converter transforms this electric potential in a digital signal (digital number, DN) that can be related to physical units after a calibration process.

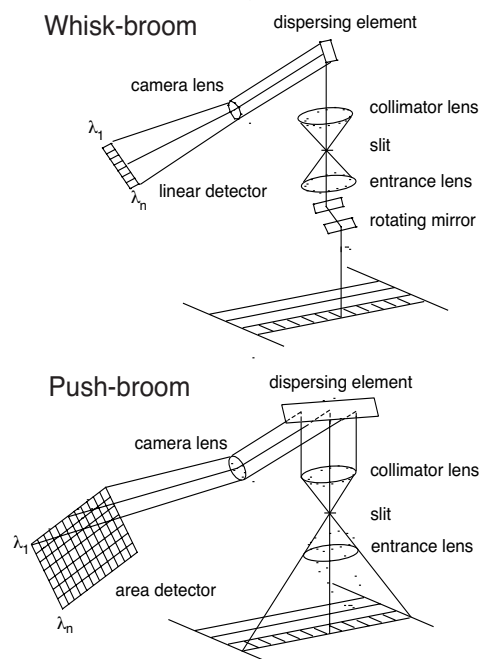
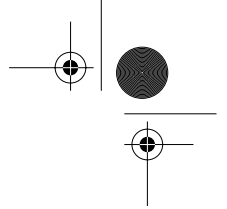


**Figure 5.1** Principles of whisk-broom and push-broom imaging spectrometers (after Goetz, 1992).

## 5.2 CASI Campaign in Lake Zug

The goal of the CASI campaign was to test the algorithms developed in this study with special emphasis put on the determination of chlorophyll *a*. The



## 5.2 CASI Campaign in Lake Zug

107

flight was performed by the Free University of Berlin in August 10, 1997, over lake Zug. The CASI system is a push-broom scanner which can be used in spatial or spectral mode. For this campaign, the sensor was flown in the spatial mode which allows to program 19 different bands in the range from 400 to 1000 nm. Tab. 5.1 summarizes the band set-up for this campaign, and some geometrical parameters. Since the internal orientation (roll, pitch, yaw) and the position of the aeroplane were not available, orthorectification and georeferencing of the scene could not be performed. A first analysis of this data set are shown in Keller et al. (1998) and Keller and Itten (2001).

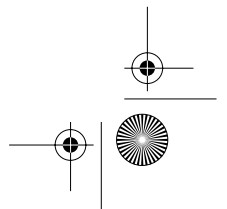
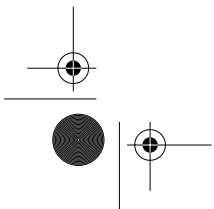
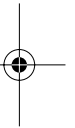
**Table 5.1** CASI set-up and geometrical parameters.

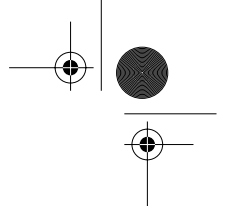
Centre wavelength [nm]	499, 518, 542, 567, 587, 603, 621, 639, 654, 671, 688, 705, 722, 739, 753, 767, 860, 900, 944
Full width at half maximum [nm]	17, 21, 28, 21, 21, 12, 25, 12, 17, 18, 17, 18, 18, 16, 14, 16, 21, 14, 14
Ground altitude of lake surface above sea level	414 m
Flight altitude above sea level	4150 m
Field of view	34.2°
Number of pixels (columns x rows)	512 x 3954
Ground sampling distance	5.3 m
Date	August 10, 1997
Flight heading	South to North
Sun azimuth / zenith angle	135° E / 48°

On the flight day, the Reagan sun photometer (Appendix A) was placed at the harbour of Zug at the northern end of the lake for the detection of atmospheric optical variations.

In order to obtain information about the spectral properties of the water, LI-COR radiometric irradiance measurements were performed at five sites in up- and downwelling directions just above the water surface and at 0.5, 2.0, 3.5, and 5.0 m below the water surface (Chapter 3.5). For logistic reasons, these measurements were performed two days before the flight.

For the determination of chlorophyll *a* and *DOC*, water samples were taken on the day of the irradiance measurements and again on the day of the flight campaign, and analysed in the laboratory. From the 13 different sites on the



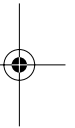


day of the flight campaign, only 8 sites were covered by the CASI scene. For a better characterisation of the lake, the algae composition — blue algae (*Planktothrix sp.*) and chromophyta (*Dinobryon sp.*) were the most relevant algae species —, and the Secchi depth were also determined. The test site locations are shown in Fig. 5.2.

It turned out that the differences of the optically relevant parameters between the sampling sites were only small (Tab. 5.2). On the other hand, the vertical variations within the profiles were much higher than the horizontal differences. As we will see, this will make it more difficult to test the inversion algorithms. Note that the reciprocal of the attenuation coefficient at 580 nm, where the light penetrates the water body the most deepest (Fig. 3.3), was almost equal to the Secchi depth. The chlorophyll *a* concentration and the Secchi depth were not correlated ( $r^2 < 0.01$ ); this is another indicator that inorganic material strongly influence the optical properties of the water.

**Table 5.2** Characterisation of the sampling sites (n.d.: not determined).

	CHL (0 m) [ $\mu\text{g l}^{-1}$ ]	CHL (3.5 m) [ $\mu\text{g l}^{-1}$ ]	DOC (0 m) [ $\text{mg l}^{-1}$ ]	Secchi depth [m]
1	2.6	n.d.	2.4	3.1
2	1.4	4.1	2.6	4.2
3	1.5	n.d.	2.5	4.1
4	2.6	6.1	2.4	4.1
5	3.5	6.3	2.4	4.4
6	3.3	n.d.	2.5	4.1
7	3.1	6.5	2.6	4.0
8	1.7	6.5	2.5	4.4



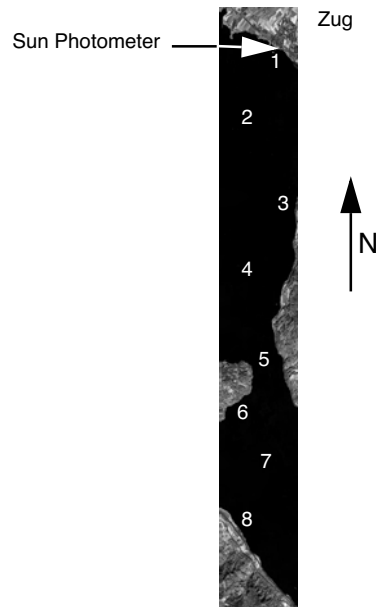


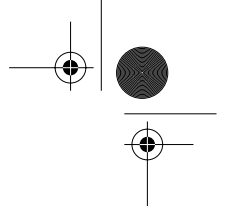
**Figure 5.2** The eight limnological sampling sites in Lake Zug (1-8). A sun photometer was placed at the harbour of Zug at the northern end of the lake. The LI-COR measurements were performed two days before the flight at the stations 1, 2, 4, 7 and between the stations 2 and 4 on the western end (not covered by the scene).

### 5.3 Information Content

In order to test the quality of imaging data, the random variability or “noise” associated with the signal of a sensor can be determined. Imaging spectrometer data contain periodic (coherent) noise and random noise, of which only the former can be removed. Random noise consists of image independent random sensor noise, image dependent photon noise, and image dependent intrapixel variability which is a result of spatially heterogeneous pixel content.

One important parameter expressing the quality of a sensor is the signal-to-noise ratio (*SNR*). The methods used for the estimation of *SNR* should be able to isolate random noise. There are several standard methods (Curran and Dungan, 1988):

- *Laboratory methods* use a bright homogeneous surface to estimate the



*SNR*. However, the signal level is artificially high and the methods do not take into account intra- and inter-pixel variability and normally do not correspond to the real in-flight conditions.

- *Dark current methods* use variation in the signal dark current as a measure of the noise which corresponds to a natural signal level. It is achieved by closing a shutter placed before the optic and subsequently measuring the resulting signal. The disadvantage is that inter-pixel variability cannot be determined.
- *Image-based methods* are frequently chosen for the determination of the *SNR*, as they have the advantage to correspond to the real in-flight conditions. Additionally, it is the only method which accounts for intra- and inter-pixel variability. A frequently used image-based method uses the average of the signal and its standard deviation of a specified area. One problem is to find a homogenous area where the scene dependent inter-pixel variation can be neglected. It would be more elegant to compare the variations of the signal caused by the variation of lake water constituents or the air-water interface with the variation of the noise caused by the sensor noise. As the standard deviation of one pixel is not defined, the “Growing Area Method” was developed as described below.

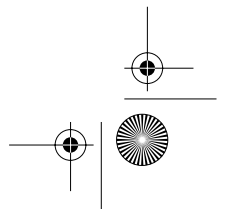
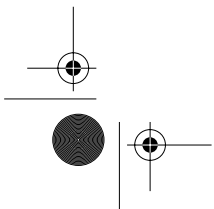
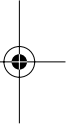
However, for the determination of the scene information not only the *SNR* is of interest, but also the amount of redundant information. Only because a spectrometer measures at  $n$  wavelengths does not mean that also  $n$  variables can be determined. Principal component analysis will help us to identify the number of determinable parameters in our data.

#### *Growing Area Method (GAM)*

We define the scene based *SNR* as the ratio of signal standard deviation  $\sigma(\text{Signal})$  to noise standard deviation  $\sigma(\text{Noise})$ :

$$SNR \equiv \frac{\sigma(\text{Signal})}{\sigma(\text{Noise})} [-]. \quad (5.1)$$

In this study, the Growing Area Method (GAM) was developed, for the determination of these parameters. The contrast of the signal was defined as the standard deviation of all water pixels. For the determination of the noise, the standard deviations *std* of a growing square around a starting point is plotted against the “square radius” (half the length of the square). We define the contrast of the noise is defined as the point of intersection of the linear regression line for the first points with the y-axis (Fig. 5.3); this value is equal to the noise equivalent at-sensor radiance difference  $NE\Delta L_s$ . This approach is



based on ideas from the semivariogram method (Schowengerdt, 1997). However, in contrast to this method, GAM does not distinguish between x- and y-dimension, and the calculated values have a more intuitive meaning.

The standard deviation  $\sigma$  is calculated as follows:

$$\sigma = t_{\alpha}^{n-1} \cdot \frac{S}{\sqrt{n}} \text{ [W m}^{-2} \text{ sr}^{-1} \text{ nm}^{-1}\text{]}, \quad (5.2)$$

where  $t_{\alpha}^{n-1}$  is given by the Student's t-statistics,  $n$  the number of the pixels in the square,  $\alpha$  the confidence interval (here a 68% confidence interval was used which corresponds to one standard deviation for the Gaussian normal distribution), and  $S$  the *empirical* standard deviation of the sample. For  $n > 100$ , this distribution is equivalent to the normal distribution. Here, the first 20 points were used for the calculation of the noise excluding the first five points since the statistical uncertainty at the determination of *std* for a small data sample is too large.

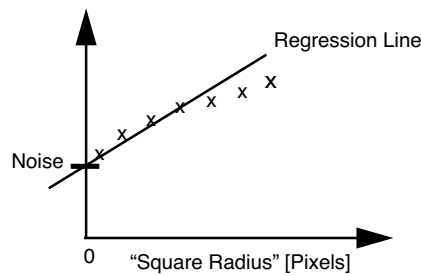


**Figure 5.3** Image-based determination of the *SNR* using the growing area method (GAM).

The calculations can be based on digital numbers, at-sensor radiance or ground reflectance. In this study, the digital numbers could not be used as the raw data were not available for the CASI scene. Consequently, the at-sensor radiance  $L_s$  is investigated, as this quantity is not affected by an error-prone atmospheric correction.

The calculations show (Fig. 5.4), that the variation of the signal is only three to four times the variation of the noise and that the noise was higher for blue and near-infrared bands resulting in poorer signal-to-noise ratios.

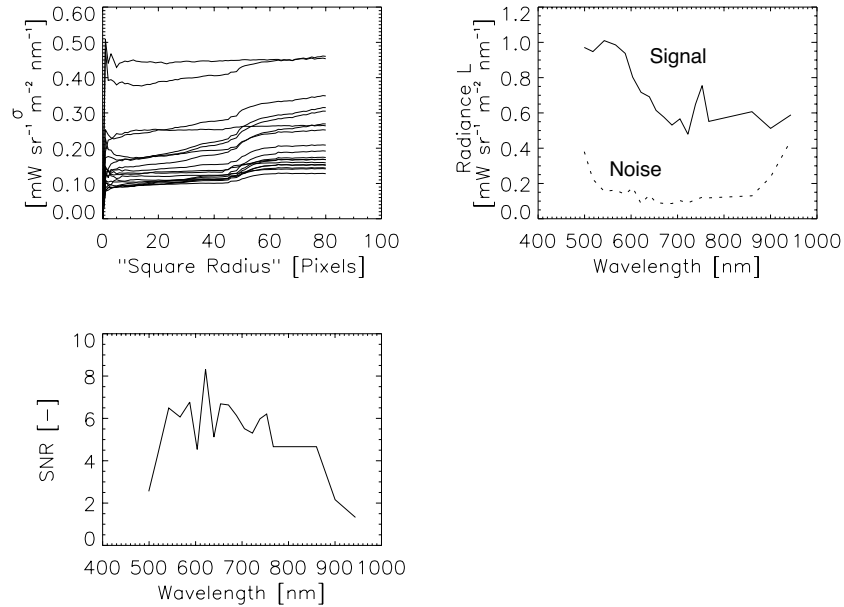


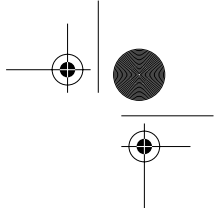
**Figure 5.4** Image-based determination of *SNR* over water pixels using the growing area method. Top left: the standard deviation *std* of the area with growing square diameter for all CASI bands. Top right: resulting signal (variation of all water pixels) and noise which is equal to the noise equivalent at-sensor radiance difference. Bottom left: resulting signal-to-noise ratio *SNR*.

#### Principal Components Analysis

Multispectral image bands are often highly correlated, i.e. they are visually and numerically similar. This correlation is caused by material spectral correlation, topographic orientation, and sensor band overlap. The principal component transformation is designed to remove this spectral redundancy and to determine the dimensionality of the data.

For the illustration of the theory, we define a data set of  $n$  bands  $\mathbf{x}$  with  $\mathbf{x}^T = [\mathbf{x}_1, \dots, \mathbf{x}_n]$  where  $\mathbf{x}_i$  are the individual pixel vectors. For the derivation of the principle components, the covariance matrix  $\Sigma_{\mathbf{x}}$  will be used, which is defined as:

$$\Sigma_{\mathbf{x}} \equiv \langle (\mathbf{x} - \mathbf{m}_{\mathbf{x}})(\mathbf{x} - \mathbf{m}_{\mathbf{x}})^T \rangle, \quad (5.3)$$



where  $\mathbf{m}$  is the mean pixel vector. It is desired to find a linear transformation  $\mathbf{a}$  of the original co-ordinates  $\mathbf{x}$ , such that:

$$\mathbf{y} = \mathbf{a}\mathbf{x} . \quad (5.4)$$

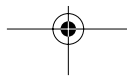
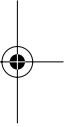
where the covariance matrix of the pixel data in  $\mathbf{y}$  space,  $\mathbf{\Sigma}_y$ , is diagonal, which refers to a image data set, in which there is no correlation between any of its components. Now, it can be shown that (Richards, 1993):

$$\mathbf{\Sigma}_y = \mathbf{a}\mathbf{\Sigma}_x\mathbf{a}^T . \quad (5.5)$$

Since  $\mathbf{\Sigma}_y$  must be diagonal,  $\mathbf{a}$  is the transposed matrix of eigenvectors of  $\mathbf{\Sigma}_x$ , and  $\mathbf{\Sigma}_y$  can be identified as the diagonal matrix of eigenvalues of  $\mathbf{\Sigma}_x$ . Each resulting eigenvalue is equal to the variance of the respective principal component image along transformed coordinate axes, and the sum of all eigenvalues is equal to the sum of all band variances of the original image. The principal component images are uncorrelated and, by convention, ordered by decreasing variances. The result is a removal of any correlation present in the original data with a simultaneous compression of most of the total image variance in less dimensions. A similar method is the maximum noise fraction (MNF) which includes knowledge about sensor noise (Green et al., 1988). However, as the sensor noise was not known, only the principal component analysis was applied.

A principal components study by Sathyendranath et al. (1989) suggests that the first six SeaWiFS bands may only have five effective degrees of freedom that can be used to determine the contents of coastal waters. Models with more parameters may lead to lower residual errors, but also to degeneracy.

Our investigation lead to similar results. For this analysis, the CASI scene was used. All water pixels were included in the analysis, leading to the variances of each principle component (Fig. 5.5 and Fig. 5.6). It could be shown, that the first three components account for 93%, and the first six components for 98% of the variation. This implies that only three or four different parameters may be determined independently with the CASI data; this is of course a strong limitation. However, this statement is only strictly true for this data set and it is expected that if more bands (especially in the blue region of the spectrum) as well as bands with smaller bandwidths and better SNR where available, more independent parameters could be determined.



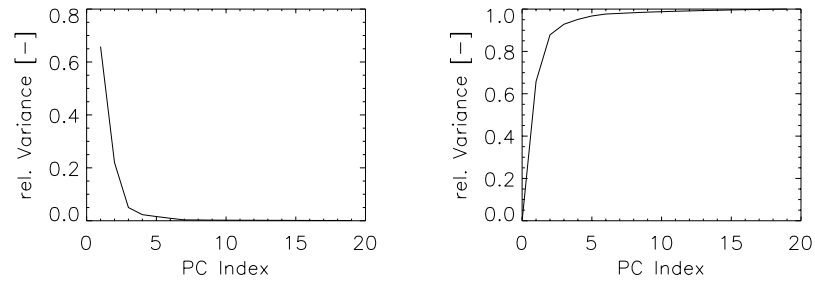


**Figure 5.5** Ratio of the variance of each principal component to the total variance ordered by size (left) and as cumulative sum (right). The first three components account for 93%, and the first six components for 98% of the variation.

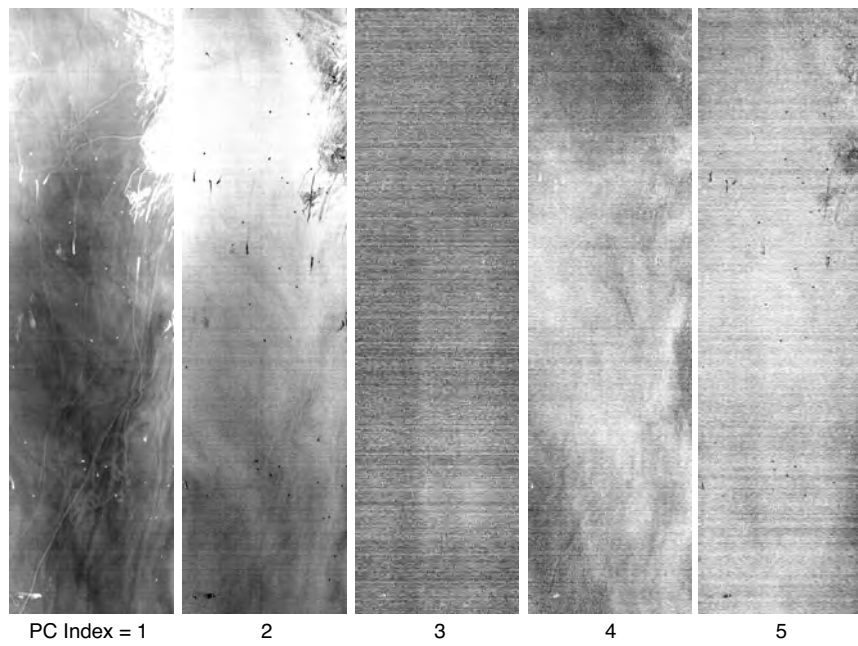
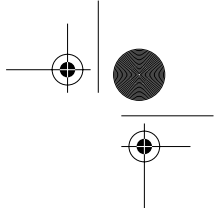


**Figure 5.6** Images of the first five principal components (detail from the North basin of Lake Zug). Only in two or three images relevant information are visible; often the variation seems to be produced by sensor noise (especially striping).



## 5.4 Atmospheric Correction

Every inversion procedure includes two steps: the determination of the model parameters and the calculation of the desired quantities. Of course, the atmospheric correction does not make any exception of this concept. In this chapter, the first step is described in more detail, whereas the second step was already presented in Chapter 4. See Fig. 5.7 for an outline of the whole algorithm.

As stated in Chapter 4.7, the transfer equation (Eq. 4.20) can be simplified to:

$$\rho(a, \xi)/\pi = r(a \rightarrow w, \xi) [\text{sr}^{-1}], \quad (5.6)$$

if it can be presumed that the water-leaving radiance is negligible, which is usually the case in the near-infrared. This is the classical *dark target approach* which is usually used for open ocean waters (Gordon and Morel, 1983; Kaufman and Sendra, 1988). This approach allows the pixel-wise determination of one atmospheric parameter (with the assumptions that all other parameters are known). Here, the meteorological range *VIS* is chosen as it is an sensitive parameter for the atmospheric and the interface correction as we have seen in the last chapters. The atmospheric and aerosol model are considered to be known from the sun photometer measurements or are determined by an educated guess. The correction algorithm is included in the module ATAQ (Appendix B.3).



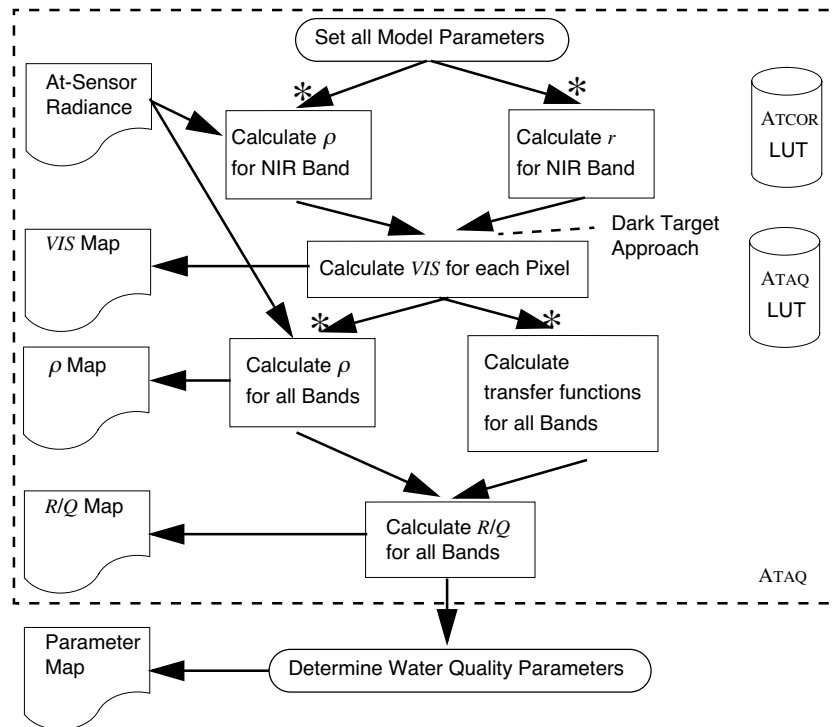
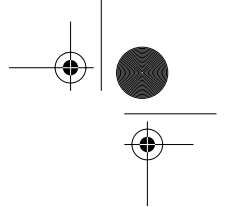


**Figure 5.7** The software module ATAQ includes atmospheric and air-water interface correction. The core of the module is the dark target approach which allows a pixel-wise determination of the meteorological range  $VIS$ . For the calculation of the atmospheric corrected reflectance  $\rho$  and the surface reflection  $r$ , ATCOR and additional ATAQ specific parameters stored in look-up tables are included; this is indicated with a star (\*) at the

The determination of the meteorological range involves several steps. First,  $\rho(a, \xi)$  and  $r$  were calculated for the near-infrared band at 860 nm for a set of meteorological ranges (i.e., 5, 10, 20, 30, 50, 75 and 100 km). This wavelength was chosen as it is not influenced by water vapour absorption and as it is far away from the visible range where the water absorption is only low; this is also the reason why all sensors dedicated for the investigation of water environments have a band in this spectral region. As the noise was too high in the near-infrared band, the data were smoothed with a low-pass box filter. For the calculation of  $\alpha$ , the LUT generated by ATCOR could be used; for the determination of  $\beta$  used in Eq. 4.22, separate MODTRAN runs had to be performed. The generation of all these terms was the most time intensive

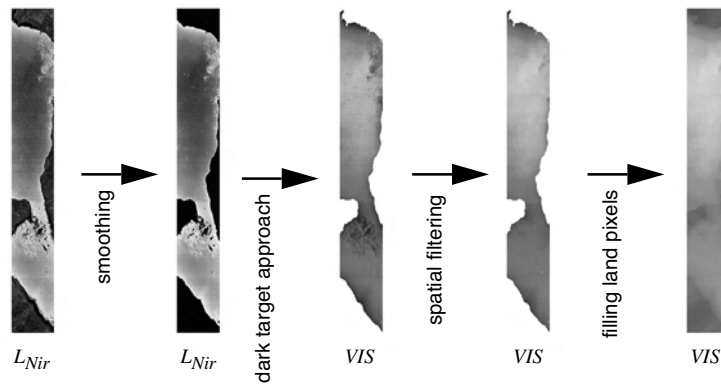


calculation part of the pre-correction; on a Sun Ultra 60 workstation, it took about 12 hours, whereas the actual application of the inversion took only about half an hour although the main part of the software was written in IDL<sup>1)</sup>. Of course, for more operational purposes, the terms could be calculated in advance for a set of several possible geometrical conditions and then interpolated for each scenario.

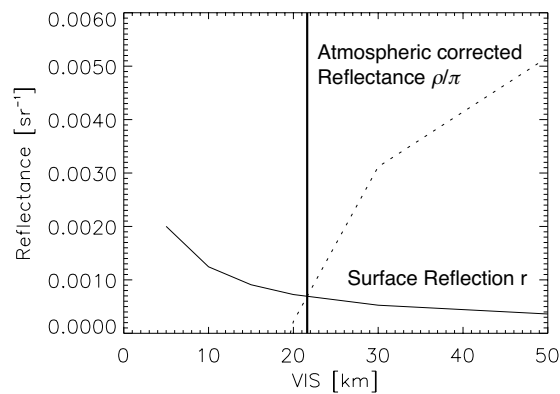
Secondly, the meteorological range is determined which fulfils Eq. 5.6. Fig. 5.9 shows that the dependence of  $\rho(a, \xi)$  on the meteorological range is strong, but that it is only weak for  $r(a \rightarrow w, \xi)$ ; it can be concluded that the former parameter has to be known very accurately, whereas the latter could be set constant (e.g., equal to zero) to save processing time.

In case of high suspended matter concentration or incorrect glitter correction, the algorithm has to be extended. In an additional step, the minimum reflectance in a certain area around each pixel is determined. In this area, at least one pixel should exist with small particulate matter concentration and no glint effect; on the other hand, the atmospheric parameters are assumed to be constant. Note that it is not possible to use directly the meteorological range due to the findings in Chapter 4.3. Then the corresponding meteorological range of the pixel with minimal reflectance is associated to the central pixel. For the CASI scene, different filter sizes were tested:  $n_s = 50, 500, 1000$ . Of course, it is also possible to determine only the darkest pixel of the entire scene, assuming that the atmospheric conditions are constant for the entire image.

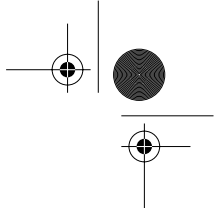
<sup>1)</sup> IDL = Interactive Data Language (<http://www.rsinc.com>). IDL is an interpreted language and therefore slower than a fully compiled language like C or Fortran.



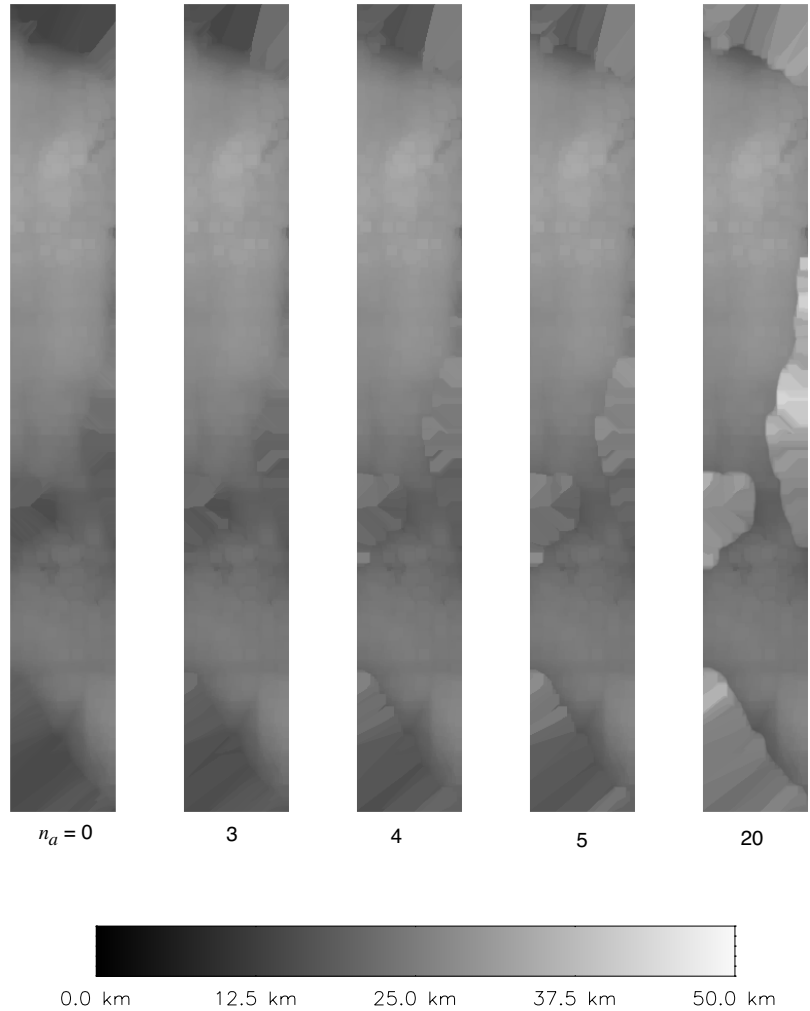
**Figure 5.8** Required steps for the generation of the VIS map. First, a near-infrared band is chosen (here at 860 nm) and low-pass filtered in order to avoid unrealistic variations, the meteorological range for all water pixels is calculated based on the dark target approach. This map has to be filtered again due to glitter effects or influences of high particulate matter concentrations. Finally, the meteorological range is calculated for the land pixels using nearest neighbour interpolation; this is required for an appropriate adjacency effect correction.



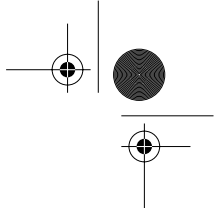
**Figure 5.9** Determination of the meteorological range using the dark target approach based on the 860 nm band of the CASI: the optimal meteorological range is where the atmospheric corrected reflectance defined as the ratio of the upwelling radiance to the downwelling irradiance [ $\text{sr}^{-1}$ ] is equal to the surface reflection as stated in Eq. 5.6; this is indicated by the vertical bar.



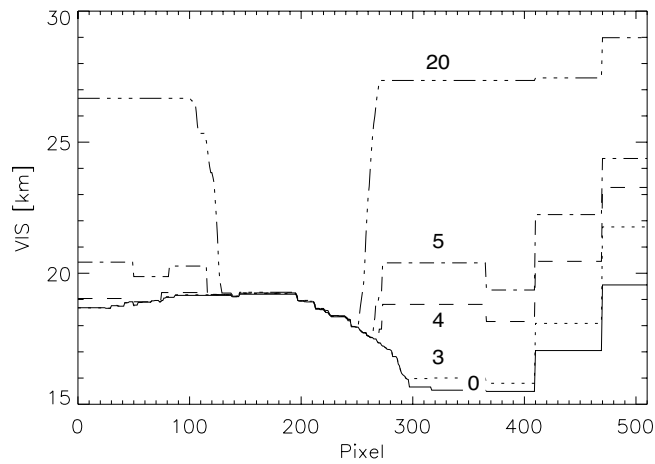
## 5.4 Atmospheric Correction



**Figure 5.10** Influence of the adjacency filter size ( $n_a$  = number of pixels) on the VIS map. The best size is where geometrical features are not visible within the scene, presumably  $n_a = 4$  for this scene. For these calculations, the spatial filtering width  $n_s$  was set to 50 pixels.



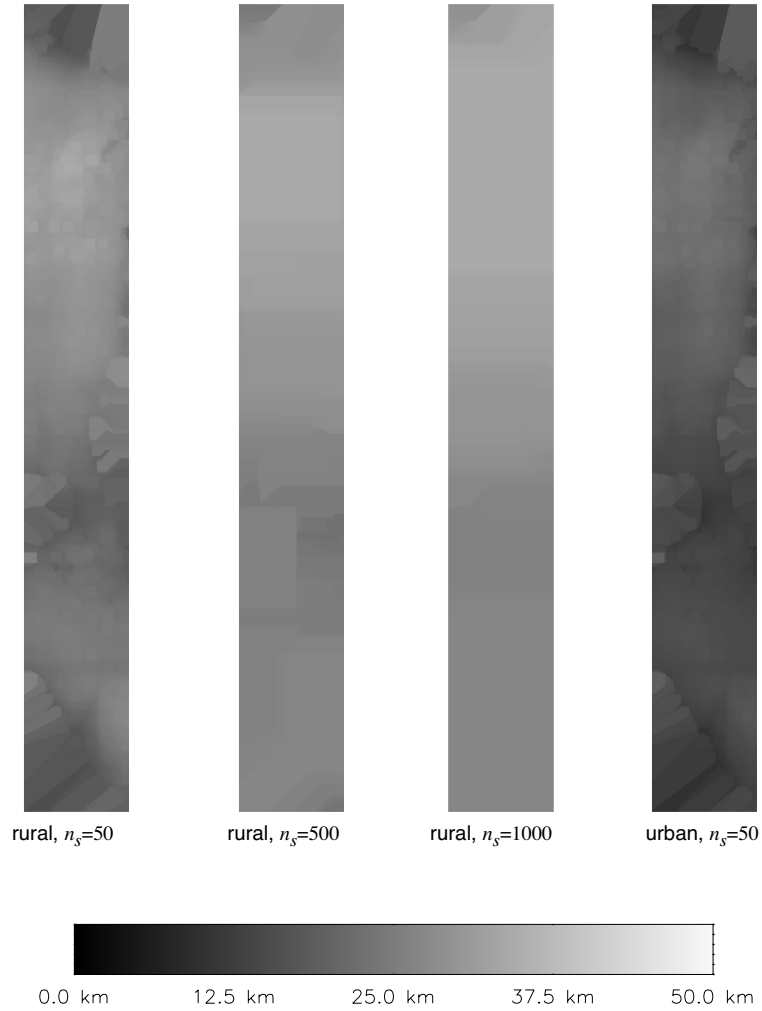
As stated in Chapter 4.4, the influence of the adjacency effect is highest for the near-infrared bands. Therefore, the filter size  $n_a$  of the adjacency post-processing has strong impacts on the determination of the meteorological range (Fig. 5.10). The best filter size is where the meteorological range does not show any geometrical features (Fig. 5.11). For the CASI scene, this is expected to be (only) 4x4 pixels. Consequently, all further calculations were performed with this filter. However, as not all relevant parameters are included in the adjacency correction (e.g., slope and aspect of land pixels or sensor characteristics), the correction is not presumed to be perfect. Fig. 5.12 shows the resulting meteorological range maps as a function of the spatial filter size  $n_s$  and the aerosol model.



**Figure 5.11** A transect through the CASI scene of the determined meteorological range  $VIS$  for different filter sizes  $n_a$  (0, 3, 4, 5 and 20 pixels). The best size is where geometrical features are not visible within the scene. Here  $n_a$  is presumed to be equal to 4.



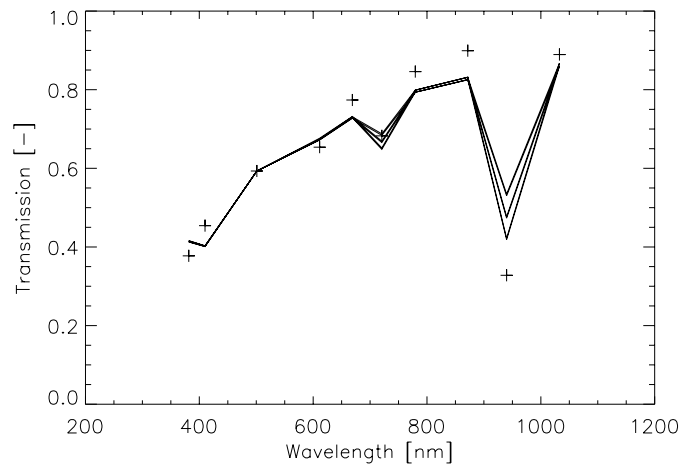
## 5.4 Atmospheric Correction



**Figure 5.12** Image-based determined VIS maps for Lake Zug for constant adjacency filter size  $n_a=4$ , and various aerosol models and spatial filter size  $n_s$  (CASI scene August 10, 1997).

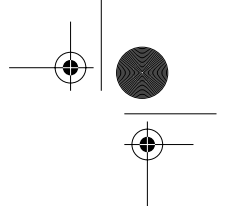


The Reagan sun photometer was used for independent verification of the method. The instrument was situated at the harbour of Zug on the northern shore of the lake. The direct transmittance was calculated using MODTRAN 4 (BETA) for given geometric conditions and different atmospheric and aerosol models with the meteorological range *VIS* as a variable input parameter. The modelled values were compared with measured values, enabling a direct determination of *VIS*. Because of the normalization used in MODTRAN (Eq. 4.1), the variations between different models are practically negligible between 500 and 550 nm (Fig. 5.13). This allows the use of the sun photometer channel at 501 nm for the calculation of *VIS*. The other bands can be applied to the definition of the atmospheric and aerosol models.



**Figure 5.13** Direct transmission for different atmospheric and aerosol models compared to the measured values (plus symbols). All models have the same transmission at 550 nm due to the normalization in MODTRAN, and differ primarily at the water vapour absorption bands at 720 nm and 940 nm.

As for constant *VIS*, the direct transmittance mainly varies at the absorption region of water vapour at 720 nm and 940 nm, the deviation to the measured values expressed with the root mean square (RMS) is mainly a function of the atmospheric model and only to a lesser extent dependent on the aerosol model (Fig. 5.14). The lowest RMS and therefore the best fit were obtained for the midlatitude summer model with rural aerosols.



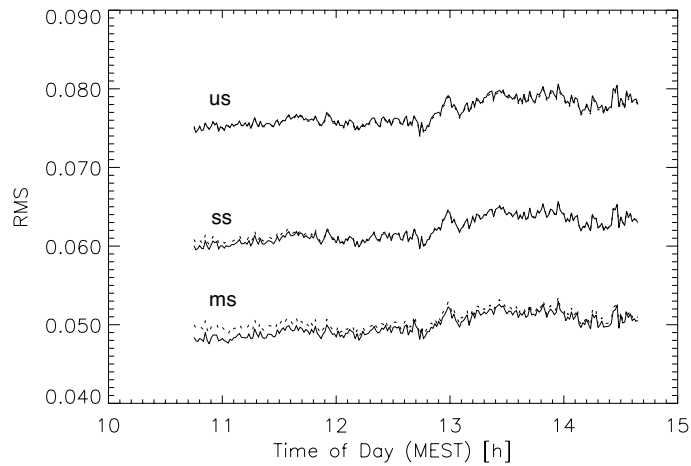
## 5.4 Atmospheric Correction

Fig. 5.15 shows the determined *VIS*. Long time trends and short time changes in the order of minutes are observable. The latter indicated that within a scene, *VIS* is not constant. Unfortunately, the flight was performed before the first acquisition of the sun photometer data. However, *VIS* during the flight at 10:38 a.m. MEST<sup>1)</sup> could be guessed with linear extrapolation to a value of 41 km. The values of the image-based meteorological range of the pixel adjacent to the sun photometer are summarized in Tab. 5.3. For all case studies, the sun photometer values were lower than those obtained with the image-based method. This could be caused by a wrong extrapolation of the sun photometer values due to their high temporal changes. The best agreement is obtained with rural aerosols and large filter sizes (i.e.,  $n_s \geq 500$  pixels). However, in order to have an impression on the real horizontal variations, more than one sun photometer should have to be placed in the campaign area.

**Table 5.3** Meteorological range *VIS* near the sun photometer for different aerosol models and filter sizes  $n_s$ . The sun photometer method led to *VIS* = 41 km.

Aerosol Model	Filter size $n_s$	<i>VIS</i>
rural	50 Pixels	26 km
rural	500 Pixels	31 km
rural	1000 Pixels	32 km
rural	whole scene	34 km
urban	50 Pixels	17 km
urban	whole scene	24 km

<sup>1)</sup> MEST = middle european summer time



**Figure 5.14** Root mean square (RMS) for all models compared with sun photometer measurements (us = US-Standard, ms = midlatitude summer, ss = subarctic summer; dotted = urban, solid = rural). The best values are obtained for the lowest RMS. During the CASI campaign at 10:38 am MEST, this is the midlatitude summer model with rural aerosols.

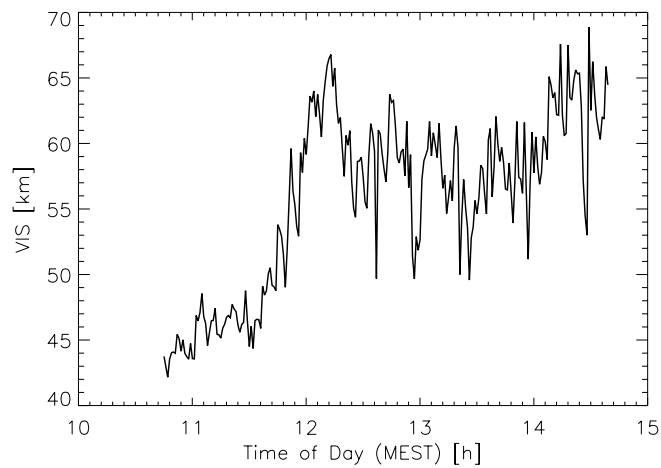


**Figure 5.15** Meteorological range determined using the sun photometer channel at 501 nm as a function of time.

## 5.5 Air-Water Interface Correction

The reflectance above and below the air-water interface is determined by re-arranging Eq. 4.20:

$$\frac{R(w)}{Q(w, \xi')} = \frac{R_{RS}(a, \xi)}{t(a \rightarrow w)t(w \rightarrow a, \xi' \rightarrow \xi)/n_w^2 + Q(w, \xi')r(w \rightarrow a)R_{RS}(a, \xi)} \quad (5.7)$$

where the remote-sensing reflectance  $R_{RS}$  is given by (Eq. 2.7):

$$R_{RS}(a, \xi) = \rho(a, \xi) - r(a \rightarrow w, \xi) \text{ [sr}^{-1}\text{]}, \quad (5.8)$$

with  $\rho(a, \xi)$  defined by (see Eq. 4.4):

$$\rho(a, \xi) \equiv L_u(a, \xi)/E_d(a) \text{ [sr}^{-1}\text{]}. \quad (5.9)$$

All terms are a function of the wavelength. In this study,  $Q(w, \xi')$  (Eq. 2.5) was always set equal to 4.5. All transfer equations were calculated based on the formulae given in Chapter 4.6, with the meteorological range determined as described in Chapter 5.4.

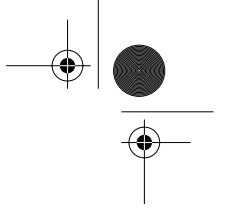
## 5.6 Evaluation of the Inversion Method

Sensitivity analyses allow the investigation of the performance of inversion methods with respect to uncertainties of model parameters. There are two different approaches:

- the *forward models* are calculated and then inverted by changing model parameters or the model itself, or
- *measured* spectra are inverted by changing model parameters or the model itself.

The first approach has the advantage that the environment and consequently the theoretical results are known. The advantage of the second approach is, that real data are used and therefore all uncertainties (even the unknown) are included. In this chapter the first approach was used and in the next chapter, the second approach was applied on real image data.

In this chapter, the main goal was to evaluate the inversion method, which should be applied to the CASI data of Lake Zug for the determination of chlorophyll. The performances of the two inversion methods based on the single scattering approximation were tested: matrix inversion, and curve



fitting. The uncertainty of the calibration coefficients, and the uncertainty of the meteorological range ( $VIS$ ) were introduced. The sensitivity analysis was performed as follows:

- *Adding noise.* First, the forward problem was solved using the single scattering approximation (Eq. 2.21) and then artificial white noise was added to each band of the spectrum:

$$\left(\frac{R(\lambda)}{Q(\lambda)}\right)_{Noise} = \left(\frac{R(\lambda)}{Q(\lambda)}\right)_{Model} (1 + s_{Noise}(\lambda)), \quad (5.10)$$

where  $s_{Noise}$  is the relative error with a mean value of 0 and a variation given by the normal distribution. This approach corresponds to an incorrectly calibrated instrument where errors in the bands do not correlate with each other. The calculations were made for relative errors of 0, 5, 10, 20, and 30%. Each modelled set contained 500 spectra.

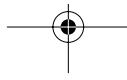
- *Changing the meteorological range  $VIS$ .* For this analysis, the at-sensor radiance had to be determined. First, the forward problem was solved using Eq. 2.21, then the air-water interface transfer functions and the radiative transfer to the sensor were calculated using the ATCOR/MODTRAN model. The meteorological range is one of the most sensitive parameters of this model, and it is expected that it strongly influence the determination of water quality parameters. The errors introduced to the bands are correlated with each other, in contrast to the first analysis. The inversion were performed for visibilities ranging from 15 to 50 km.

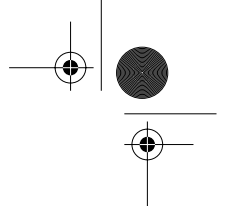
The following bio-optical model was used (see Eq. 2.46 and Eq. 2.45):

$$b_b(\lambda) = b_{b,w}(\lambda) + b_{b,0} \cdot b_{b,inorg}^*(\lambda) + CHL \cdot b_{b,org}^*(\lambda), \quad (5.11)$$

$$a(\lambda) = a_w(\lambda) + a_g(\lambda) + CHL \cdot a_p^*(\lambda). \quad (5.12)$$

Note that the detritus absorption is not included in the analysis as only the wavelength range above 500 nm is covered by the CASI. The phytoplankton absorption spectrum was given by Lee's equation (Eq. 2.38) with  $a_p^*(440\text{nm}) = 0.03 \text{ m}^{-1} / (\mu\text{g l}^{-1})$ . The gelbstoff absorption was calculated with Eq. 2.35 with  $S = 0.0171$ ,  $a_g^*(\lambda_0) = 0.048 \text{ l mg}^{-1} \text{ m}^{-1}$  and  $DOC = 2.6 \text{ mg l}^{-1}$ . And finally, the specific backscattering coefficients determined with the *in situ* radiometric measurements were taken (Chapter 3.4). For the forward modelling, the following parameter set was chosen: viewing zenith angle =  $0^\circ$  (nadir),  $VIS = 30 \text{ km}$ ,  $CHL = 3 \mu\text{g l}^{-1}$ ,  $b_{b,0} = 0.03 \text{ m}^{-1}$ . The inversions were performed with bands 1 to 12 (499 nm to 705 nm) of the CASI. The other bands





## 5.6 Evaluation of the Inversion Method

127

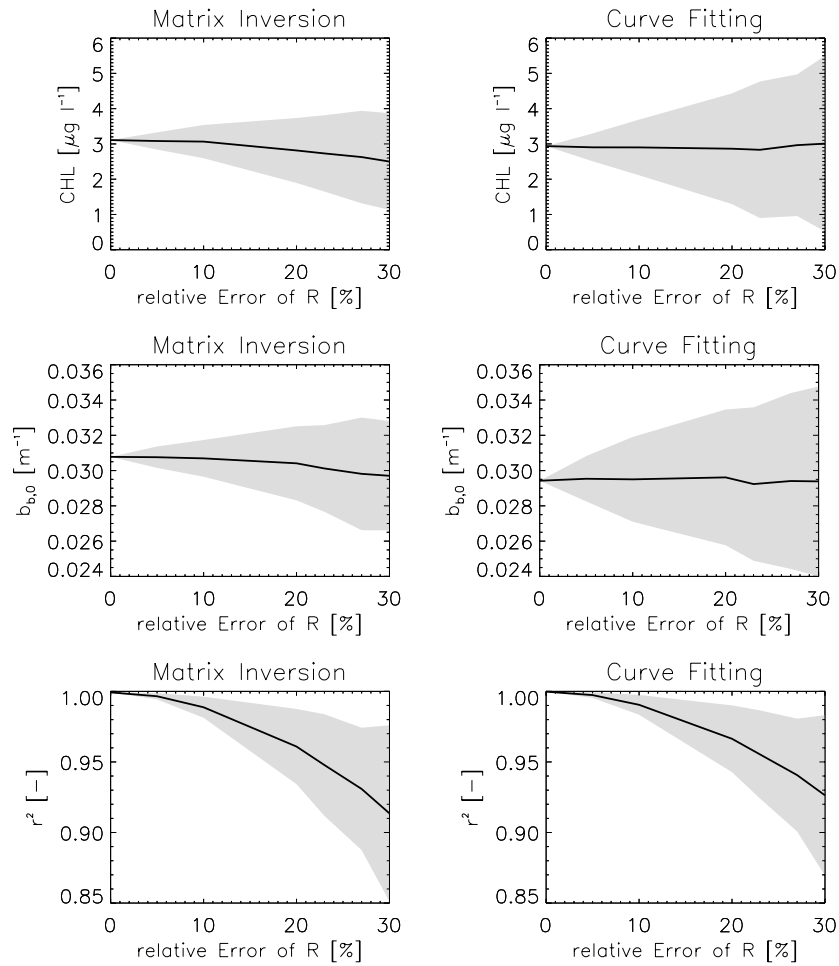
in the near-infrared were not used because they are disturbed by the absorption of atmospheric water vapour. The analysis follows Keller (2001), but uses a different bio-optical model and is based on the more recent MODTRAN 4 (Beta) and ATCOR 4 versions, rendering slightly different results.

Fig. 5.16 shows the result of adding white noise to the spectra. The average and the standard deviation of the retrieved parameters, and the correlation coefficient between forward modelled and inverted reflectance spectrum were calculated for each relative error. The correlation coefficient was almost identical for both methods. Even if no noise was added, both methods did not exactly lead to the input concentrations due to interpolation uncertainties, and since not all bands were used for inversion. Additionally uncertainties occurred for the matrix inversion due the convolution of the signal to the sensor characteristics (Chapter 2.11).

Compared with the other method, the standard deviation of the curve fitting method was higher, but the average was closer to the input chlorophyll *a* concentration. For a relative error of 30%, the chlorophyll *a* concentrations (curve fitting:  $3.0 \mu\text{g l}^{-1}$ ; matrix inversion:  $2.5 \mu\text{g l}^{-1}$ ) and the inorganic backscattering coefficient (curve fitting:  $0.029 \text{ m}^{-1}$ ; matrix inversion:  $0.030 \text{ m}^{-1}$ ) lay close to the input values. However, one reason for the good results for the curve fitting routine was, that the starting value of the fitting procedure was set to the input values of the forward modelling; this was necessary, as no minimum was found when the starting value differed too much from the optimal value.

The effect of inaccurate *VIS* was larger than the difference between the two inversion methods (Fig. 5.17). If the *VIS* is chosen too small, the algorithm resulted into too small chlorophyll concentrations<sup>1)</sup>. Due to numerical uncertainties (i.e., interpolation and convolution), the determination of the meteorological range led to a result differing slightly from the input value, *VIS* = 28 km, even the calculation of the reflectance spectrum above the surface corresponded almost perfectly to the input spectra. For this value, the chlorophyll *a* concentration (curve fitting:  $2.2 \mu\text{g l}^{-1}$ ; matrix inversion:  $1.6 \mu\text{g l}^{-1}$ ) differed considerably from the input value, while the inorganic backscattering coefficient (curve fitting:  $0.027 \text{ m}^{-1}$ ; matrix inversion:  $0.027 \text{ m}^{-1}$ ) was only weakly influenced. This is a result of the weak dependence of the backscattering coefficient on *CHL*; it is expected that if this dependence and consequently also the influence of changing chlorophyll *a* concentration on the reflectance were stronger, more robust results could be expected.

<sup>1)</sup> We will see this phenomenon also at the analysis of the image data.



**Figure 5.16** The influence of white noise added on the reflectance spectrum on the determination of chlorophyll a (CHL) and inorganic scattering ( $b_{b,0}$ ) for the matrix inversion and curve-fitting method.

## 5.6 Evaluation of the Inversion Method

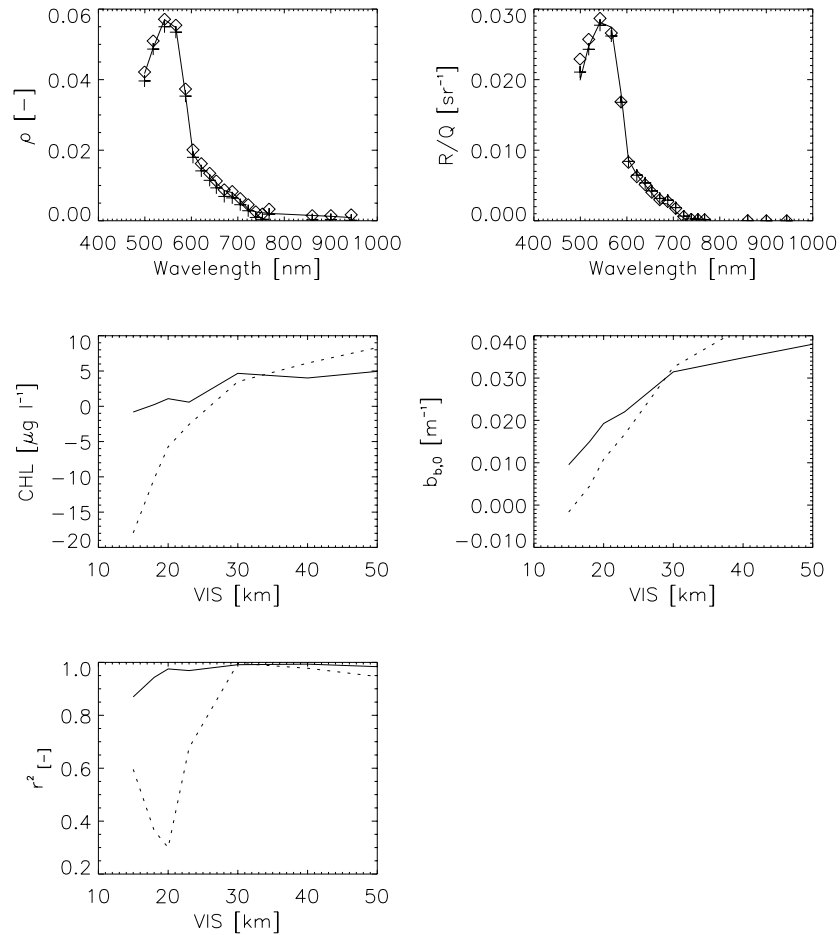
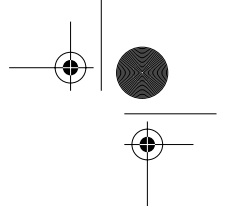


**Figure 5.17** The influence of unknown meteorological range  $VIS$  on the chlorophyll  $a$  and inorganic backscattering determination. Top left: reflectance above the air-water interface  $\rho = \pi L_u/E_d$  (line: forward modelled; plus symbol: backward modelled with determined  $VIS = 28$  km; square symbol: backward modelled with input  $VIS = 30$  km). Top right: reflectance below the air-water interface  $R/Q$  (line: forward modelled for input  $VIS = 30$  km; plus symbol: fit with curve fitting method for determined  $VIS = 28$  km; square symbol: fit with matrix inversion method for determined  $VIS = 28$  km). In the following figures, the dependence of the chlorophyll  $a$  concentration (centre left), the inorganic scattering coefficient (centre right), and the correlation coefficient on  $VIS$  is shown (bottom left; solid: curve fitting; dotted: matrix inversion).



The results of the sensitivity analysis give rise to the question of the superiority of the inversion method. This question cannot be answered universally. One possibility is to compare the correlation coefficients. However, if one parameter may be determined more accurately at the expense of the accuracy of another parameter, the answer to this question depends also on the parameter of interest. In any case, special emphasis should be put on the issue of biased results, because only unbiased methods yield lower uncertainties in a post-process using spatial filtering. Finally, in case that image data be investigated, it is important to analyse the resulting horizontal distribution; if the distribution does not look reasonable, the inversion method may not be reliable.

For the determination of the water quality parameters based on the CASI scene in the next chapter, the matrix inversion method was used due to following reasons:

- it is much faster than the curve-fitting method,
- the results do not depend on a starting value, and
- no convergence tolerance has to be chosen.

## 5.7 Determination of Water Quality Parameters in Lake Zug

The final goal of the analysis is the determination of water quality parameters. This is shown in this chapter based on the CASI scene of Lake Zug. As there are many unknown parameters, different case studies were performed to investigate their individual influence on the resulting maps. The following parameters were varied: the aerosol model, the meteorological range filter size  $n_s$  (Chapter 5.4), and the phytoplankton absorption (Tab. 5.4).

Since the atmospheric models hardly influence the pre-correction (except for the water absorption bands), this parameter is not changed and all calculations are performed with the midlatitude summer model.

**Table 5.4** Case studies applied for testing the performance of the inversion algorithm. The atmospheric and bio-optical parameters were varied.

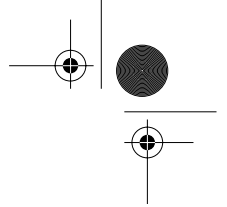
	Aerosol Model	VIS Filter size $n_s$	$a_p^*(440\text{nm})$ [ $\text{m}^{-1}/(\mu\text{g l}^{-1})$ ]
I	rural	whole scene	0.03
II	rural	whole scene	0.05
III	rural	whole scene	0.02
IV	rural	50 pixels	0.03
V	rural	500 pixels	0.03
VI	rural	1000 pixels	0.03
VII	urban	whole scene	0.03

The same bio-optical model used for the sensitivity analysis was applied on the image data (Eq. 5.11 and Eq. 5.12). The specific scattering coefficients  $b_{b,org}^*(\lambda)$  and  $b_{b,inorg}^*(\lambda)$  were determined using Eq. 3.8 as stated in Chapter 3.4. Since the gelbstoff absorption  $a_g$  has not been measured, it had to be parameterized using Eq. 2.35 and Eq. 2.36. The fit parameters were assumed to be equal to the values measured in Lake Zürich:  $S = 0.071 \text{ nm}^{-1}$ ,  $a_g^* = 0.048 \text{ l mg}^{-1}$ . As the first available CASI band is at 499 nm and as the gelbstoff absorption is low above 500 nm (Fig. 2.7), the introduced inaccuracy by this parameterization is negligible. The same reasonings can be made for the detritus absorption which was neglected. The specific phytoplankton absorption coefficient  $a_p^*(\lambda)$  is parameterized using Lee's equation with the parameter determined for Lake Constance (Chapter 2.6).

The first case (I) was presumed to be the most realistic parameter set:

- Rural aerosols are the obvious choice for Lake Zug.
- The least artificial effects were expected by using the darkest pixel of the entire scene for the determination of VIS.
- $a_p^*(440\text{nm}) = 0.03 \text{ m}^{-1}/(\mu\text{g l}^{-1})$  corresponds to an average phytoplankton spectrum in Lake Constance.

Matrix inversion was used for the determination of the parameters (see discussion in the last chapter). Only the first 12 bands (499 nm to 705 nm) of the CASI were included for the inversion of the sub-surface reflectance as the signal amplitude in the other bands were too low due to water absorption. The algorithms for the determination of water quality parameters are merged in the software module DETCONC (Appendix B.3).



Almost all case studies resulted into negative chlorophyll concentrations (Fig. 5.18). Reasonable fits to the measured reflectance spectrum did not automatically imply accurate concentrations (Fig. 5.19), which confirms the results in the last chapter. The variations between the different case studies were in the same order as the inter-scene variations which were only about  $2 \mu\text{g l}^{-1}$  rendering the verification of the inversion very difficult. The aerosol model<sup>1)</sup> and the choice of  $a_p^*(440\text{nm})$  influenced the calculated chlorophyll  $a$  concentration only in the order of  $2\text{-}3 \mu\text{g l}^{-1}$ . The *VIS* map with the lowest spatial filter size  $n_s$  (case IV) led to the worst result (Fig. 5.20). As the sensitivity analysis in Chapter 5.6 led to too low values for *CHL* if *VIS* has been chosen too low, it can be concluded that the image based atmospheric correction algorithm generally yielded too low *VIS*. Note that the sun photometer method led to higher values than the image based method (Tab. 5.3) which also confirms the findings above.

For all cases, the calculated chlorophyll  $a$  concentration and the scattering coefficient  $b_{b,0}$  showed a positive correlation (Fig. 5.21). It could be concluded that the correlation between these two parameters might be stronger than found in *situ* radiometric measurements in Chapter 3.4. However, this correlation could also only be an artefact introduced by the model. The validation of the *CHL* maps (Fig. 5.22) is difficult, as very often negative values occurred (black pixels).

Compared to the *CHL* maps, the  $b_{b,0}$  distribution (Fig. 5.23) seems to be more reliable. However, it was not possible to test the accuracy of scattering coefficient as no *in situ* measurements were available. If the assumption is true that in reality, *CHL* and  $b_{b,0}$  correlate stronger than found in our *in situ* measurements (see above), then the  $b_{b,0}$  distribution could give a hint about the *CHL* distribution. While the influence of the aerosol model was only weak for chlorophyll, the scattering coefficient  $b_{b,0}$  is affected more strongly by this parameter. However, only the absolute quantities differ whereas the relative distribution is similar for all cases.

For regions with high reflectances, noisy patterns are visible in the *CHL* and  $b_{b,0}$  maps. As it was not possible to separate the influence of surface glitter and high particle scattering because of their similar signature, the verification of the result is difficult. Even in regions with high reflectances caused by boats, it could not be decided whether the reflectances were influenced by glitter and whitecaps or by particles which were brought near the air-water surface by upwelling turbulent mixing (Fig. 5.24).

There are various other possibilities for the differences between measured and determined lake quality parameters. In particular the calibration of the

<sup>1)</sup> Of course, this is only true if the proposed image-based atmospheric correction algorithm is used.

## 5.7 Determination of Water Quality Parameters in Lake Zug

imaging spectrometer in the near-infrared region is crucial for an adequate atmosphere and air-water interface correction and therefore also for an accurate determination of water quality parameters.

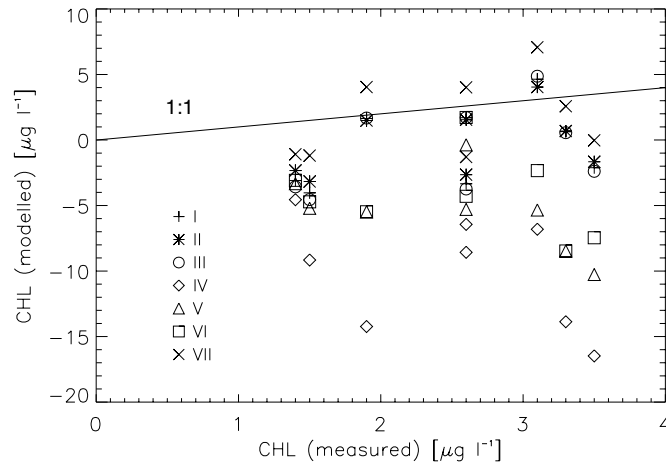


**Figure 5.18** Modelled versus modelled chlorophyll a concentrations for the different case studies. The line indicates where the modelled values would be equal to the measured values.

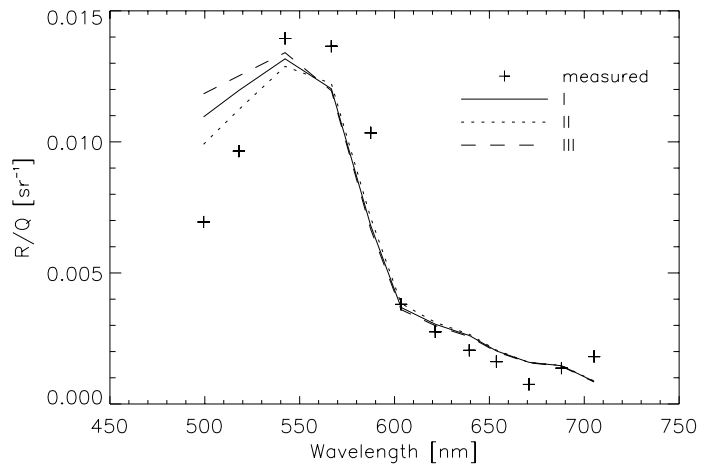


**Figure 5.19** Fits to the measured reflectance (+) for the first three case studies.

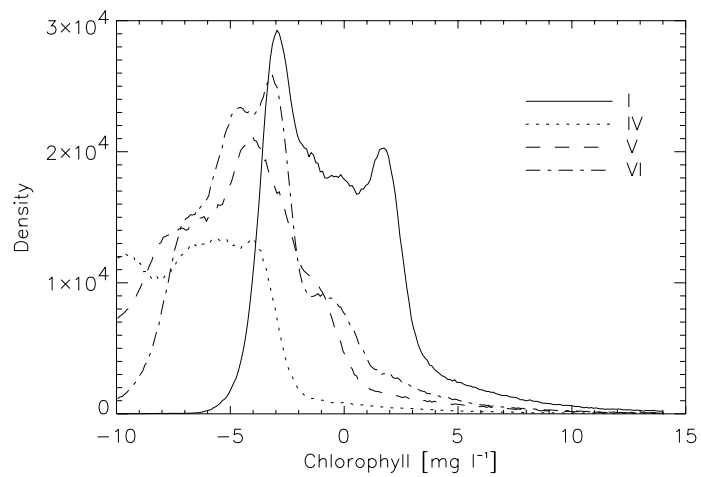


**Figure 5.20** Frequency distribution of the chlorophyll  $a$  concentrations for the different case studies. The inter-lake variations change with the image-based method.



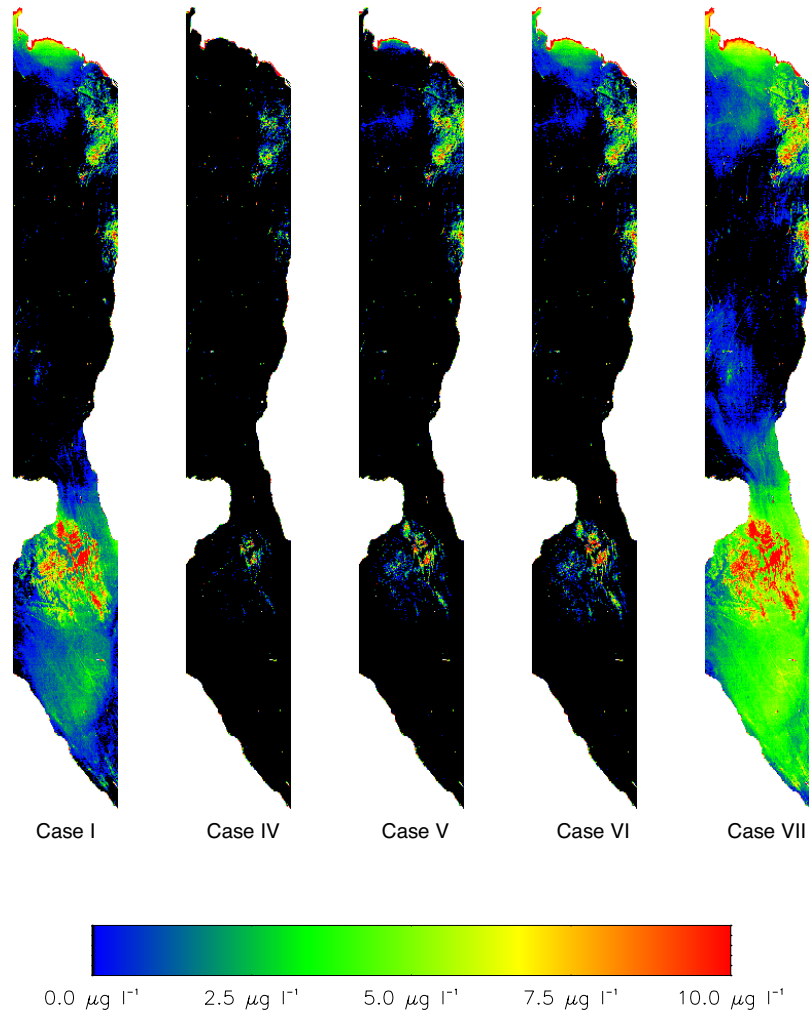


**Figure 5.22** Chlorophyll a maps for different case studies. Values larger lower  $0 \mu\text{g l}^{-1}$  are masked (black).

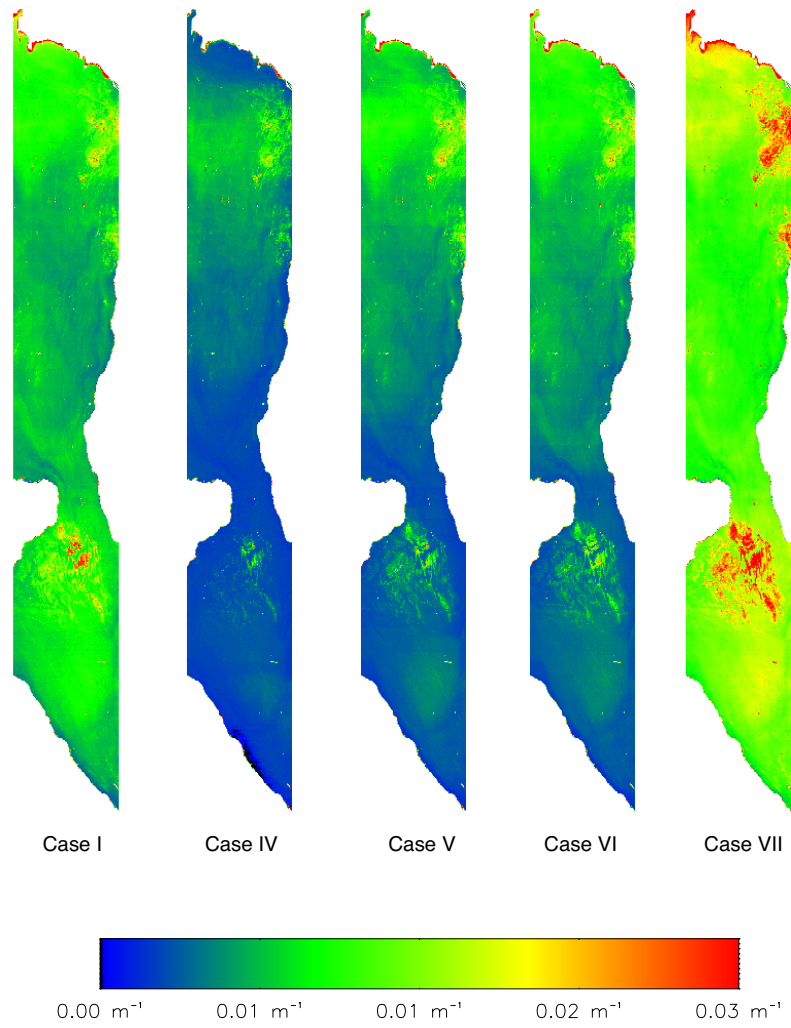


**Figure 5.23** Backscattering coefficient  $b_{b,0}$  for different case studies.

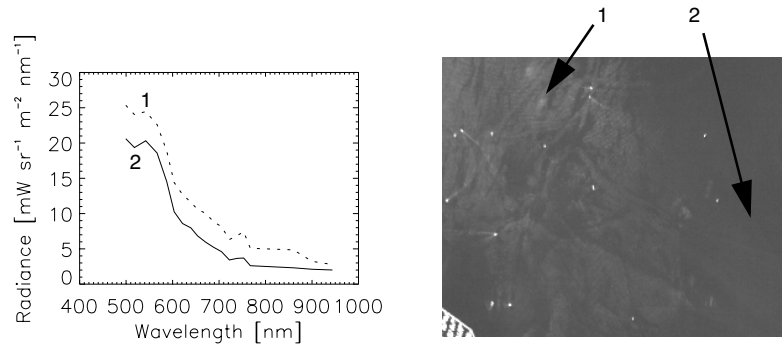
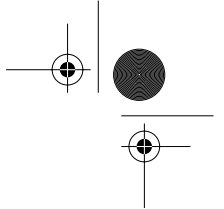


**Figure 5.24** Patterns with low and high reflectance indicated by the two arrows (587 nm). Since the signature of surface glitter and high particle scattering are similar, a separation of these effects is almost impossible.

## 5.8 Conclusions

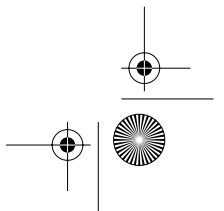
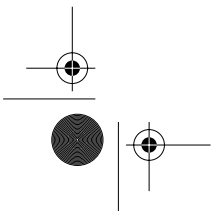
In this chapter, water quality parameters were determined based on image data. The results can be summarized as follows:

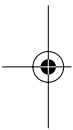
- An image-based determination of the signal-to-noise ratio was developed which allows a fast investigation of the quality of the data. It could be shown that in the CASI scene of Lake Zug, the variation of the signal is only three to four times the variation of the noise. The information content is best determined with a principal component analysis. The calculations showed that based on the investigated data set, three components are sufficient to explain 93% of the variations.
- The image-based determination of the meteorological range *VIS* allows the investigation of the horizontal variation of atmospheric parameters. Adjacency effects became visible due to the dependence of the determined meteorological range on the near-infrared band and had therefore to be corrected.
- Sensitivity analyses can be used to test the performance of inversion methods and to investigate model uncertainties.
- The results of the chlorophyll *a* determination, based on image data, were ambiguous. One problem was, that only small gradients occurred and that therefore the requirements on the inversion algorithms and especially on the pre-corrections (i.e., atmosphere and air-water interface correc-

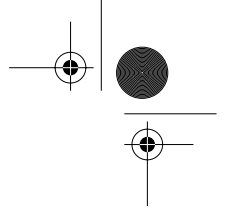


## 5.8 Conclusions

tion) increased. Another problem was that the influence of glitter effects, high particulate matter concentration and changing atmospheric conditions could hardly be separated due to their similar signatures.







## Chapter 6

# Conclusions and Outlook

The benefit of remote-sensing methods is determined mainly by the accuracy of the calculated values, but also by their operability and performance. This is the subject of this chapter where a discussion of the presented methodology and the sensor requirements, as well as a comparison between classical limnology and remote-sensing methods is given.

### 6.1 Methodology

---

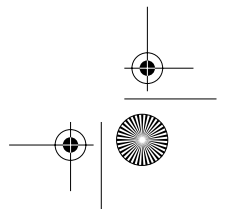
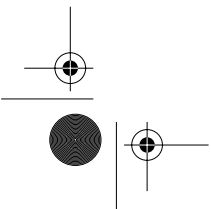
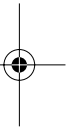
The main goal of this study was to present a methodology for the determination of water quality parameters based on imaging spectroscopy data. In this chapter the results are summarized and discussed.

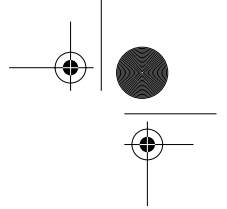
In this study, radiometric *in situ* measurements were used for the characterisation of inland water. Only weak correlation between particulate matter and chlorophyll *a* were found, what shows that lakes have highly variable constituents that are strongly influenced by non-living organic and inorganic material. The analysis of such waters is a demanding task since a change in the chlorophyll concentration only yields little variation in the reflectance, and since therefore, the quality required of the sensor, as well as of the atmospheric and air-water interface correction is high.

Thus, great care was taken for the pre-correction. Under the assumption that the radiance leaving the water is zero in the near infrared, it was possible to derive the meteorological range which determines the aerosol concentration in the radiative transfer models. This image-based approach allowed a pixel-wise correction of atmospheric and air-water interface effects and the calculation of the sub-surface reflectance.

Chlorophyll *a* concentration and inorganic scattering were determined with matrix inversion. This method is based on the single scattering approximation which relates absorption and scattering coefficients to the sub-surface reflectance. The advantage of this method is that it is possible to determine simultaneously various parameters. However, this implies also, that the error of one determined parameter has also impacts on the errors of the others.

The analyses showed that the influence of glitter effects, high particulate matter concentration and changing atmospheric conditions could hardly be





separated due to their similar signatures. A solution for this problem would be the use of methods for the characterisation of the atmosphere and air-water interface that do not rely on water characteristics, especially the assumption that the water-leaving radiance in the near-infrared is zero. For example, the satellite system MOS (Tab. 1.1) allows the determination of the aerosol characteristics with four narrow bands in the oxygen absorption region. In addition, the use of other sensor systems could improve the results. Thus, radar sensors could be flown simultaneously to the optical system for the description of the roughness of the water surface (e.g., synthetic aperture radar SAR, see Fig. 6.1).

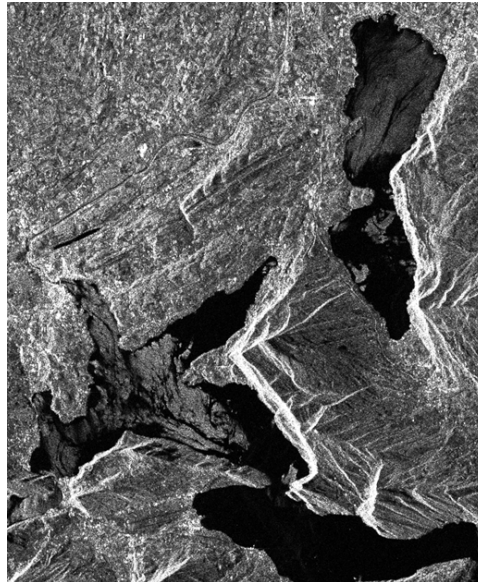
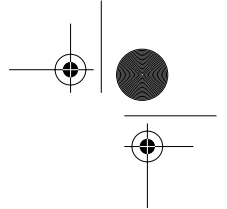


**Figure 6.1** ERS-2 SAR C-band image of central Switzerland covering Lake Zug and Lake Lucerne on May 23, 1999 (© ESA/EARTHNET).

The determination of water quality parameters implies some other critical aspects which should be investigated in further studies:

- *Inherent parameters.* The accuracy of inherent parameters determines the performance of the inversion methods. Consequently, additional measurements are necessary for a comprehensive understanding of the bio-optical conditions in a lake. Especially the dependence of the scatter-



ing coefficient on the chlorophyll concentration should be investigated in more detail.

- *Detection of gelbstoff.*<sup>1)</sup> From the remote-sensing perspective, this parameter is interesting, as it can influence the determinability of other water quality parameters, and as it was hardly successfully determined by remote-sensing means yet.
- *Band characteristics.* The minimal number and the best position of the bands were important for the definition of new sensors.
- *New inversion approaches.* Methods such as neural networks, may improve the results (better accuracy, faster inversion).

Various supplementing products are possible when water quality parameters are determined on an operational basis:

- The usefulness of the determined chlorophyll *a*, gelbstoff and particulate matter concentrations is improved by providing secondary products, such as primary production, phosphate or nitrogen concentration.
- Optical (visible and thermal) together with radar data could be used to implement a biophysical model which would yield more information about the vertical distribution of the water quality parameters. For lakes, this is desirable for two reasons: (i) the results of the determination of water quality parameters improve, and (ii) for judging the state of the lake ecosystem, vertical information (e.g., oxygen or temperature profiles) is often more important than horizontal information.

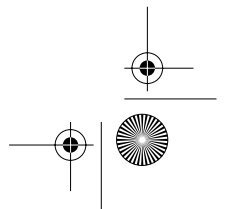
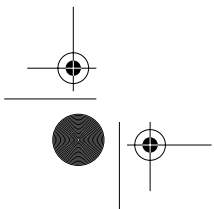
The goal of remote sensing of lakes should be the long-term monitoring of this ecosystem. Of course, this is a demanding task, and only little experience has been acquired in this field yet. Furthermore, it is questionable, if it will be possible sometime to monitor quality parameters without any *in situ* measurements at all for the (re-)calibration of the models, since inherent parameters may vary over time,

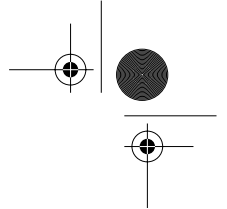
## 6.2 Sensor Requirements

The requirements for characterising inland waters are often different than for coastal or open ocean waters. Following sensor characteristics can be defined for operational investigations of lakes:

- The *ground sampling distance* should account for the spatial scale where

<sup>1)</sup> Note that the Casi configuration flown over Lake Zug was not suitable for the detection of gelbstoff because no spectral information below 480 nm was available.





changes occur in freshwater environment ( $10^1 - 10^3$  m) as well as for the extension of lakes ( $10^2 - 10^4$  m).

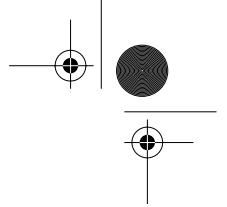
- A *repetition rate* of several days is appropriate, due to the fast revolving nature of freshwater environments. Furthermore, this high frequency allows compensating recordings, where clouds cover up the water body. This could be accomplished with a series of polar orbiting, closely spaced spaceborne sensors or a pointing sensor on a polar orbit. However, this may only be met, if a less expensive technology is available.
- In order to investigate long-term trends, time series covering  $10^0$ - $10^1$  years are required.
- The *number of bands* should be about 15 to 20 bands, ranging from 400 to 1000 nm with a *spectral resolution* of about 5-15 nm, and the possibility to program the position and the width of the bands allowing a flexible investigation of different limnological systems.
- *Thermal bands* could be added for the determination of the temperature of skin surface temperature (SST).
- The *radiometric resolution* and the signal-to-noise ratio should be high enough to allow the detection of little variations.

Of course, the specifications depend on the method used for the inversion; empirical methods require looser specifications, whereas analytical methods have to meet higher requirements. On the other hand, the choice of the method depends on the lake of investigation and on the needed generalizations (temporal or spatial).

Unfortunately, most of today's sensors in space do not meet the desired spatial, temporal, radiometric or spectral requirements needed for the investigation of optical complex lakes (Tab. 1.1). On the other hand, airborne systems are in general expensive or even not available and can therefore not be used on an operational basis yet. However, looking at the rapid development of sensor hardware, it appears only a question of time until suitable sensors are available.

### 6.3 Classical Limnology versus Remote-Sensing

It is important to acknowledge, that remote-sensing methods are always less accurate than direct *in situ* determination of water quality parameters and that perhaps always *in situ* measurements will be needed for the (re-) calibration of inversion methods. The relative standard deviations of the results are often less accurate than desired by end users, which is in the order of 10% for chlorophyll and 20% for particulate matter (Dekker et al., 1998).



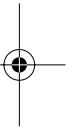
### 6.3 Classical Limnology versus Remote-Sensing

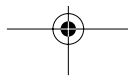
145

However, remote-sensing methods have properties that allow a supplementing of classical limnological monitoring programs (Tab. 6.1).

**Table 6.1** Comparison between limnological and remote-sensing techniques (modified from EC, 1999).

	Limnology	Remote-Sensing
Measure of ecological state	good	medium
Discrimination (type of constituent)	good	poor
Precision of the parameter determination	high	poor/good depending on the parameter
Realization costs	medium	high
Operational costs	high	relatively low for large areas and long-time periods
Frequency	limited	relatively high if several satellites can be used
Spatial information	limited	very high
Data publication	fair	appealing





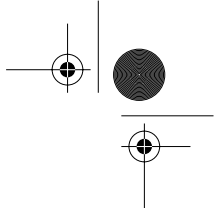
# Appendix A

## Instrument Specifications

Tab. A.1 summarizes the specifications of the spectroradiometers used in this study.

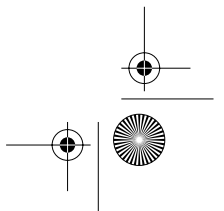
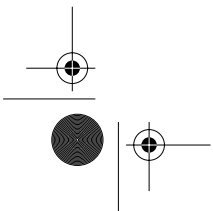
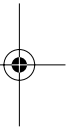
**Table A.1** Radiometer specifications (n.d.: no data available).

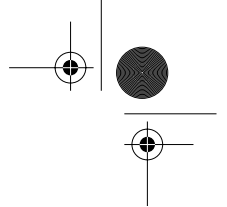
	LI-COR 1800 UW	GER1500 DFOV	GER3700	Reagan Sun Photometer
Manufacturer	LI-COR	Geophysical and Environmental Research Corp.	Geophysical and Environmental Research Corp.	Department for Electrical Engineering, University of Tuscon.
System	One field spectroradio- meter in a watertight housing. Scanning, 7 filters.	Two field spectroradio- meter in a watertight housing. Silicon CCD array.	One Silicon and two PbS CCD arrays.	Separate filters for each channel.
Range of Use	Underwater and field measurements	Underwater and field measurements	Field mea- surements	Sun-looking ground based instrument
Optic	irradiance collector	5°-10° and irradiance collector	2°, 10° or 23°	3.2°
Wavelength Range	350-1100 nm	350-1050 nm	350-1100/980- 1900/1900- 2500 nm	382, 410, 501, 611, 669, 7721, 780, 872, 940, 1033 nm
Number of Channels	80 - 800	512	704	10
FWHM	6 nm	3 nm	3/10-18/16-22 nm	8-12 nm



**Table A.1** Radiometer specifications (n.d.: no data available). (Continued)

	LI-COR 1800 UW	GER1500 DFOV	GER3700	Reagan Sun Photometer
Spectral Sampling Interval	1, 2, 5, 10 nm	1.5 nm	1.5/ 5-9/8-11 nm	(not continuous)
Spectral Accuracy	± 1.5 nm	n.d.	± 1.0 nm	n.d.
Reference	Manufacturer	Manufacturer	Manufacturer; Schaepman (1998)	Ehsani and Reagan (1992); Schläpfer (1998)





## Appendix B

# Computer Hardware and Software

### B.1 Hardware

---

All calculations were performed on a Sun Ultra 60 workstation (360 MHz processor speed, 512 MB RAM) or a Sun Ultra 2 workstation (2 x 200 MHz, 400 MB RAM) running under the Sun Solaris 5.7 operating system. The writing-up was done on an Apple Macintosh G3 computer (300 MHz, 64 MB RAM).

### B.2 Software

---

The software was developed under RSI Interactive Data Language IDL 5.3 (<http://www.rsinc.com>) and C using the Sun Workshop Professional C 5.0 compiler.

MODTRAN 4.0 (Beta) was provided by AFGL (<http://www.plh.af.mil/VSBM/gpoc/modtran.html>) and ATCOR 4 by Rolf Richter, DLR Oberpfaffenhofen, Germany.

Typesetting was done using Adobe FrameMaker 5.5 (<http://www.adobe.com>) with Times and Helvetica family typefaces.

### B.3 Modules

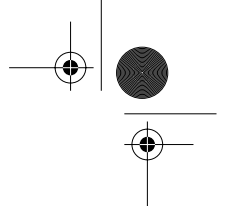
---

One goal of the study was to implement a complete processing chain for the analysis of image data. For this purpose, software was written for the determination of inherent parameters based on Mie calculations (PAR) and *in situ* radiometric measurements (RADIO), a combined atmospheric and air-water interface package (ATAQ), and a module for the inversion of sub-surface reflectance determining water quality parameters (DETCONC).

#### *PAR*

The FORTRAN code given in Bohren and Huffman (1983) for Mie calculation was rewritten and extended in C in order to smoothly include the code into the program package. The corresponding theory can be found in Chapter 2.10). The module includes following tasks:





- reading of particulate size distribution measurement data,
- calculation of the scattering matrix and the efficiency coefficients using the code given by Bohren and Huffman (1983), and
- determination of bulk parameters.

#### *RADIO*

In this IDL module, radiometric *in situ* measurements were compared with concentration determinations. See Chapter 3.4 for details about the theory. The module performs following tasks:

- reading of GER1500 DFOV data,
- calculation of depth dependent diffuse attenuation coefficient  $K_D$  and remote sensing reflectance  $R/Q$ ,
- calculation of inherent parameters  $a$  and  $b_b$ ,
- looking for corresponding concentration measurements, and
- calculation of specific inherent parameters.

#### *ATAQ*

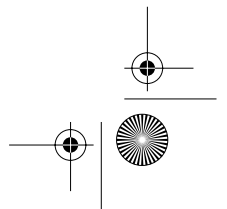
The module for atmospheric and air-water interface correction of aquatic environments ATAQ contains modified parts of ATCOR 4 written in IDL. Information about the theory can be found in Chapter 4. The module includes various tasks:

- reading of an ASCII input file containing the campaign parameters,
- running MODTRAN 4 (Beta) in batch mode for the determination of all atmospheric correction parameters, and writing the results into ASCII files (\*.sp7) using modified ATCOR 4 modules,
- reading \*.sp7 files and convoluting to sensor of interest (\*.atm) using modified ATCOR 4 modules,
- determination of the visibility map using the image-based approach,
- calculation of the remote sensing reflectance over the air-water interface, and
- determination of the sub-surface remote sensing reflectance  $R/Q$ .

#### *DETCONC*

The module DETCONC determines water constituents based on sub-surface reflectance spectra using different inversion algorithms. First, this code was written in IDL, but since the semi-analytical algorithms have to be performed pixel-wise, it has been rewritten in C for better performance. The following inversion methods have been integrated (Chapter 2.11):

- curve fitting and

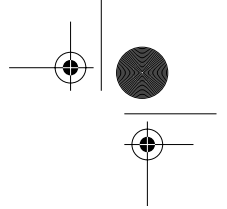




- matrix inversion.







## References

Aas E., 1994. A simple method for radiance calibration. In: Wernand M.R. (Ed.), *European workshop on optical ground truth instrumentation for the validation of space-borne optical remote sensing data of the marine environment.*, Netherlands Institute for Sea Research report NIOZ-Rapport, **1994-3**: 39-44.

Anger C. D., Babey S. K., and Adamson R. J., 1990. A new approach to imaging spectroscopy. *Proceedings of SPIE's international conference on imaging spectrometry of terrestrial environment, Orlando, Florida*, **1298**: 72-86.

Arrigo K. R. and Brown C. W., 1996. Impact of chromophoric dissolved organic matter on UV inhibition of primary productivity in the sea. *Mar. Ecol. Prog. Ser.*, **140**: 207-216.

Baker E. T. and Lavelle J. W., 1984. The effect of particle size on the light attenuation coefficient of natural suspensions. *J. Geophys. Res.*, **89**(C5): 8197-8203.

Berk A., Bernstein L. S., and Robertson D. C., 1989. MODTRAN: a moderate resolution model for LOWTRAN 7. *U.S. Air Force Geophysics Laboratory, Hanscom Air Force Base, Mass., GL-TR.89-0122*.

Bochter K. and Wallhäuser C., 1996. New instrument for simultaneous measurement of the daylight field's optical properties above and under water. *Proc. SPIE, Ocean Optics XIII (1996)*, 2963.

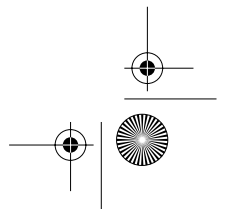
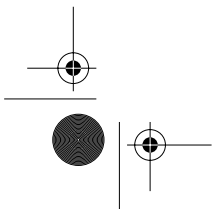
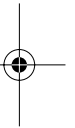
Bohren C. F. and Huffman D. R., 1983. Absorption and scattering of light by small particles. *John Wiley & Sons, New York*, 530 pp.

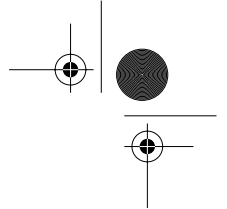
Börner A., Wiest L., Keller P., Reulke R., Richter R., Schaeppman M., and Schläpfer D., 2001. SENSOR: a tool for the simulation of hyperspectral remote sensing systems. *ISPRS J. of Photogrammetry & Remote Sensing*, **55**: 299-312.

Bricaud A., Morel A., and Prieur L., 1981. Absorption by dissolved organic matter of the sea (yellow substance) in the UV and visible domains. *Limnol. Ocean.*, **26**(1): 43-53.

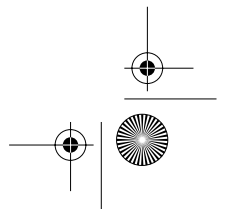
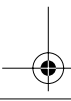
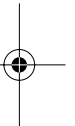
Bricaud A. and Morel A., 1986. Light attenuation and scattering by phytoplanktonic cells: a theoretical modelling. *Appl. Opt.*, **25**: 571-580.

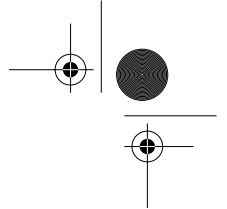
Bricaud A., Bédhomme A.-L., and Morel A., 1988. Optical properties of diverse phytoplanktonic species: experimental results and theoretical



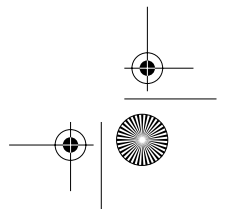
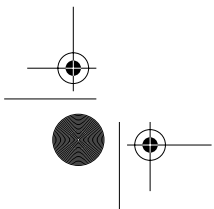
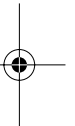


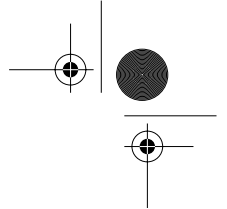
- interpretation. *J. Plankton Res.*, **10**(5): 851-873.
- Bricaud A. and Stramsky D., 1990. Spectral absorption coefficients of living phytoplankton and nonalgal biogenous matter: A comparison between the Peru upwelling area and the Sargasso Sea. *Limnol. Ocean.*, **35**(3): 562-582.
- Bruegge C. J., Conel J. E., Margolis J. S., Green R. O., Toon G., Carrere V., Holm R. G., and Hoover G., 1990. In situ atmospheric water-vapor retrieval in support of AVIRIS validation. *Proceedings of SPIE's international conference on imaging spectrometry of terrestrial environment, Orlando, Florida*, **1298**: 150-163.
- Buckton D., O'Mongain E., and Danaher S., 1999. The use of neural networks for the estimation of oceanic constituents based on the MERIS instrument. *Int. J. Remote Sensing*, **20**(9): 1841-1851.
- Bukata R. P., Jerome J. H., Kondratyev K. Y., and Pozdnyakov D. V., 1995. Optical Properties and Remote Sensing of Inland and Coastal Waters. *CRC Press, Boca Raton*, 362 pp.
- Bulgarelli B., Kisselev V.B., and Roberti L., 1999. Radiative transfer in the atmosphere-ocean system: the finite-element method. *Appl. Opt.*, **38**(9): 1530-1542.
- BUWAL, 1994. Der Zustand der Seen in der Schweiz. *Bundesamt für Umwelt, Wald und Landschaft, Gewässerschutz, Schriftenreihe Umwelt Nr. 237*, 159 pp.
- Cathomen C., 1997. Nachbarschaftseffekte und Bildspektrometrie. *Master Thesis Department of Geography, University of Zürich*, 122 pp.
- Chen Z., Curran P. J. and Hansom J. D., 1992. Derivative reflectance spectroscopy to estimate suspended sediment concentration. *Remote Sens. Environ.*, **40**: 67-77
- Cocks T., Janssen R., Stewart A., Wilson I., Shields T., 1998. The HyMap airborne hyperspectral sensor: the system, calibration and performance. *Proceedings of the first EARSeL Workshop on Imaging Spectroscopy, 6-8 October 1998, Zürich, Switzerland, EARSEL, Paris*, pp. 37-42.
- Cox C. and Munk W. H., 1954. The measurement of the roughness of the sea surface from photographs of the sun's glitter. *J. Opt. Soc. Am.*, **44**: 838-850.
- Cox C. and Munk W. H., 1955. Some problems in optical oceanography. *J. of Mar. Res.*, **14**(1): 63-78.
- Curran P.J. and Dungan J.L., 1988. Estimating the signal-to-noise ratio of



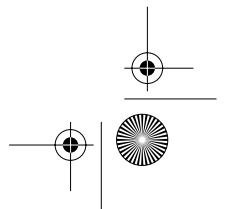
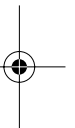


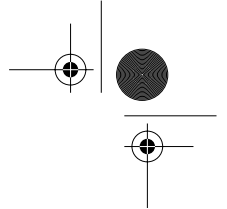
- AVIRIS data. *NASA Tech. Mem. 101035*, 22 pp.
- Davies-Colley R. J. and Vant W. N., 1987. Absorption of light by yellow substance in freshwater lakes. *Limnol. Ocean.*, **32**(2): 416-425.
- Deschamps P. Y., Herman M., Lenoble J., Tanré D., and Viollier M., 1980. Atmospheric effect in remote sensing of ground and ocean reflectances. In: Remote sensing of atmosphere and oceans, Ed. Deepak A., *Academic Press, New York*, pp. 115-147.
- Dekker A., 1993. Detection of optical water quality parameters for eutrophic waters by high resolution remote sensing. *PhD Thesis Vrije Universiteit Amsterdam*, 222 pp.
- Dekker A., Malthus T. J., and Hoogenboom H. J., 1995. The remote sensing of inland water quality. In: Advances in Environmental Remote Sensing. Eds. Danson F. M. and Plumer S. E., *Wiley & Sons, New York*, pp. 123-142.
- Dekker A., de Haan J., Keller P., Kokke J., Ruddick K., and van der Woerd H., 1998. *POWERS - User Requirements Document, W-98/16, Institute for Environmental Studies, Vrije Universiteit, Amsterdam*, 86 pp.
- Doerffer R. and Fischer J., 1994. Concentrations of chlorophyll, suspended matter, gelbstoff in case II waters derived from satellite coastal zone color scanner with inverse modelling methods. *J. Geophys. Res.*, **99**(C4): 7457-7466.
- Duysens L. N. M., 1956. The flattening of the absorption spectrum of suspensions, as compared to that of solutions. *Biochemica et biophysica acta*, **19**: 1-12.
- Ehsani A. R. and Reagan J. A., 1992. A Microprocessor Based Auto Sun-Tracking Multi-Channel Solar Radiometer System. In *Proceedings of IGARSS'92*, Houston, TX, pp. 1696-1698.
- EC, 1999. European Commission. Manual for monitoring european lakes using remote sensing techniques. Eds.: T. Lindell, D. Pierson, G. Premazzi, and E. Zilioli. *EUR 18665, Luxembourg: Office for official publications of the European Communities*, 164 pp.
- Exton R. J., Houghton W. M., Esaias W., Haas L. W., and Hayward D., 1983. Spectral differences and temporal stability of phycoerythrin fluorescence in estuarine and coastal waters due to the domination of labile cryptophytes and stable cyanobacteria. *Limnol. Ocean.*, **28**: 1225-1231.
- Gaedke U., 1992. The size distribution of plankton biomass in a large lake and its seasonal variability. *Limnol. Ocean.*, **37**(6): 1202-1220.



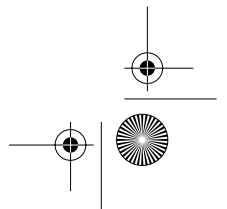
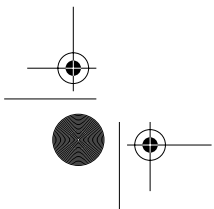
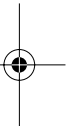


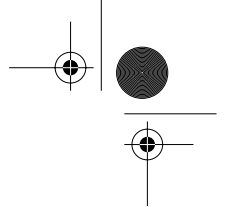
- Gege P., 1994. Gewässeranalyse mit passiver Fernerkundung: Ein Modell zur Interpretation optischer Spektralmessungen. *Ph.D. Thesis University of Hamburg. DLR Forschungsbericht 94-15*, 171pp.
- Gege P., 1999. Lake Constance: Yellow substance measurements in 1998. *DLR IP 552-9/99*, 17 pp.
- Goetz A. F. H., 1992. Principles of narrow band spectrometry in the visible and IR: instruments and data analysis. F. Toselli and Bodechtel (eds.), *Imaging Spectroscopy: Fundamentals and prospective Applications*. Kluwer Academic Publishers, pp. 21-32.
- Goodin D.G., Han L., Fraser R.N., Rundquist D.C., Stebbins W.A. and Schalles J.F., 1993. Analysis of suspended solids in water using remotely sensed high resolution derivative spectra. *Photogrammetric Engineering and Remote Sensing*, **59**(4): 505-510.
- Gordon H. R. and McCluney W. R., 1975. Estimation of the depth of sunlight penetration in the sea for remote sensing. *Appl. Opt.*, **14**(2): 413-416.
- Gordon H. R., Brown O. B., and Jacobs M. M., 1975. Computed relationships between the inherent and apparent optical properties of a flat homogenous ocean. *Appl. Opt.*, **14**(2): 417-427.
- Gordon H. R. and Clark D. K., 1980. Remote sensing optical properties of a stratified ocean: an improved interpretation. *Appl. Opt.*, **19**(20): 3428-3430.
- Gordon H. R., and Morel A., 1983. Remote assessment of ocean color for interpretation of satellite visible imagery, a review. *Springer-Verlag, New York*, 114 pp.
- Gordon H. R., Austin R. W., Clark D. K., Brown J. W., Brown O. B., Evans R. H., and Broenkow W. W., 1985. Ocean color measurements. *Chapter 8 in Satellite Oceanic Remote Sensing*, B. Saltzman, Editor, Academic Press, San Diego, pp. 297-333.
- Gordon H. R., 1985. Ship perturbations of irradiance measurements at sea, 1: Monte Carlo simulations. *Appl. Opt.*, **24**(4): 172-182.
- Gordon H. R., Brown O. B., Evans R. H., Brown J. W., Smith R. C., Baker K. S., and Clark D. K., 1988. A semianalytic radiance model of ocean color. *J. Geophys. Res.*, Vol., **93**: 10,909-10,924.
- Gordon H. R., 1989. Can the Lambert-Beer law be applied to the diffuse attenuation coefficient of ocean water? *Limnol. Ocean.*, **34**(8): 1389-1409.
- Gordon H. R., 1991. Absorption and scattering estimates from irradiance



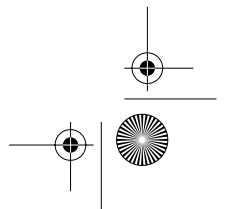
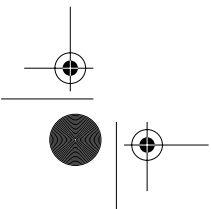
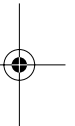


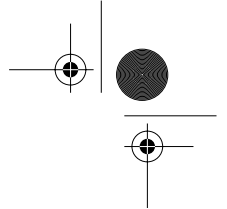
- measurements: Monte Carlo simulations. *Limnol. Ocean.*, **36**(4): 769-777.
- Green A. A., Berman M., Switzer P., and Craig M. D., 1988. A transformation for ordering multispectral data in terms of image quality with implications for noise removal. *IEEE Transactions on Geoscience and Remote Sensing*, **26**(1): 65-74.
- Heege T. and Appenzeller A. R., 1998. Correlations of large-scale patterns of turbidity and pelagic fish biomass using satellite and acoustic methods. *Arch. Hydrobiol. Spec. Issues Advanc. Limnol.*, **53**: 489-503.
- Helliwell W. S., 1985. Finite-difference solution to the radiative-transfer equation for in-water radiance. *Appl. Opt.*, **2**(8): 1325-1330.
- Hoge F. E. and Lyon P. E., 1996. Satellite retrieval of inherent optical properties by linear matrix inversion of oceanic radiance models: an analysis of model and radiance measurement errors. *J. Geophys. Res.*, **101**: 16,631 – 16,648.
- Jerlov N., 1976. *Marine Optics. Elsevier Oceanography Series 14, Elsevier Publishing Co., Amsterdam*, 231 pp.
- Kaufman Y. J., and Sendra C., 1988. Algorithm for automatic atmospheric corrections to visible and near-IR satellite imagery. *Int. J. Remote Sensing*, **9**: 1357-1381.
- Kaufman Y. J., 1989. The Atmospheric Effect on Remote Sensing and its Correction. *In Theory and Applications of Optical Remote Sensing, Ed. G. Asrar, John Wiley & Sons, New York, Chap. 9*, 336 pp.
- Keller P. A., Keller I., and Itten K., 1998. Combined Hyperspectral Data Analysis of an Alpine Lake Using CASI and DAIS 7915 Imagery. *Proceedings of the first EARSeL Workshop on Imaging Spectroscopy, 6-8 October 1998, Zürich, Switzerland, EARSEL, Paris*, pp. 237-243.
- Keller P. A., 2001. Comparison of two inversion techniques of a semi-analytical model for the determination of lake water constituents using imaging spectrometry data. *The Science of the total Env.*, **268**: 189-196.
- Keller P. A. and Itten K., 2001. Combined atmospheric and air-water interface correction for waterquality estimations. *Proceedings of the second EARSeL Workshop on Imaging Spectroscopy, 10-13 July 2000, Enschede, The Netherlands, EARSEL, Paris*, in print.
- Kerker M., 1969. *The scattering of light and other electromagnetic radiation. Academic Press, New York*, 66 pp.





- Kirk J. T. O., 1975a. A theoretical analysis of the contribution of algal cells to the attenuation of light within natural waters. I. General treatment of suspensions of pigmented cells. *The New Phytologist*, **75**: 11-20.
- Kirk J. T. O., 1975b. A theoretical analysis of the contribution of algal cells to the attenuation of light within natural waters. II. Spherical cells. *The New Phytologist*, **75**: 21-36.
- Kirk J. T. O., 1976. A theoretical analysis of the contribution of algal cells to the attenuation of light within natural waters. III. Cylindrical and spheroidal cells. *The New Phytologist*, **77**: 341-358.
- Kirk J. T. O., 1981. Monte Carlo Procedure for Simulating the Penetration of Light into Natural Waters. *CSIRO Aust. Div. Plant Ind. tech. Pap.*, **36**: 1-16.
- Kleiner L. E. and Brown C. W., 1999. Estimating oceanic chlorophyll concentrations with neural networks. *Int. J. Remote Sensing*, **20**(1): 189-194.
- Kostkowski H. JJ., 1997. Reliable spectroradiometry. *Spectroradiometry Consulting, La Plata., MA*, 609 pp.
- Kurer Ursula, 1994. Bestimmung der Chlorophyllkonzentration im Zugersee anhand von AVIRIS-Bildspektrometriedaten. *Master Thesis Department of Geography, University of Zürich*, 121 pp.
- Lathrop R. G., Lillesand T. M., and Yandell B. S., 1991. Testing the utility of simple multi-date thematic mapper calibration algorithms for monitoring turbid inland waters. *Int. J. Remote Sensing*, **12**(10), 2045-2063.
- Lee Z., Carder K. L., Mobley C. D., Steward R. G., and Patch J. S., 1998. Hyperspectral remote sensing for shallow waters. I. A semianalytical model. *Appl. Opt.*, **37**(27): 6329-6338.
- Levenberg K., 1944. A method for the solution of certain non-linear problems in least squares. *Quart. Appl. Math.*, **2**: 164-168.
- Lichtenthaler H. K., 1987. Chlorophylls and carotenoids: Pigments of photosynthetic biomembrans. *Methods in Enzymology*, **148**: 350-382.
- Marquard D. W., 1963. An algorithm for least-squares estimation of nonlinear parameters. *J. Soc. Indust. Appl. Math.*, **11**(2): 431-441.
- Martin A. E., 1957. Difference and derivative spectra. *Nature*, **180**(4579): 231-233.
- Meys S., Illi R., Ribi B., 1994. Comparison of chlorophyll-a analysis by HPLC and spectrophotometry: Where do the differences come from? *Archiv für Hydrologie*, **132**: 129-139.





Middleton E. M. and Marcell R. R., 1983. Literature relevant to remote sensing of water quality. *NASA Tech. Mem.*, 85077, 98 pp.

Mie G., 1908. Beiträge zur Optik trüber Medien, speziell kolloidaler Metallösungen. *Ann. Phys.*, **25**: 377-442.

Mobley C. D., Gentili B., Gordon H. R., Jin Z., Kattawar G. W., Morel A., Reinersmann P., Stamnes K., and Stavn R. H., 1993. Comparison of numerical models for computing underwater light fields. *Appl. Opt.*, **32**(36): 7484-7504.

Mobley C. D., 1994. Light and Water. *Academic Press Inc., San Diego*, 592 pp.

Morel A., 1974. Optical properties of pure water and pure sea water. In: N.G. Jerlov and E.S. Nielsen, editors. *Optical Aspects of Oceanography. Academic Press Inc., New York*, pp. 1-24.

Morel A. and Gentili B., 1993. Diffuse reflectance of oceanic waters. II. bi-directional aspects. *Appl. Opt.*, **32**(33): 6864-6879.

Mueller J. L. and Austin R. W., 1995. Ocean Optics Protocols for SeaWiFS Validation, Revision 1, SeaWiFS Technical Report Series. *NASA Tech. Mem. 104566(25)*, 67 pp.

O'Melia C. R. and Bowman K. S., 1984. Origins and effects of coagulation in lakes. *Schweiz. Z. Hydrol.*, **46**(1): 64-85.

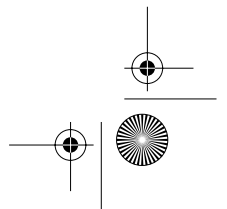
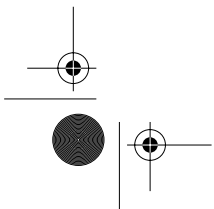
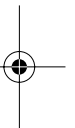
O'Reilly, J. E., Maritorena, S., Mitchell, B. G., Siegel, D. A., Carder, K. L., Garver, S. A., Kahru, M., and McClain, C., 1998. Ocean color chlorophyll algorithms for SeaWiFS. *J. Geophys. Res.*, **103**(C11): 24,937 – 24,953.

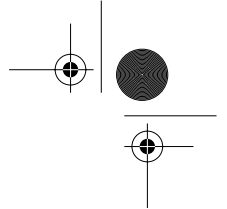
Palmer K. F. and Williams D. J., 1974. Optical properties of water in the near infrared. *Appl. Opt.*, **64**(2): 1107-1110.

Pegau W. S., Cleveland J. S., Doss W., Kennedy C. D., Maffione R. A., Mueller J. L., Stone R., Trees C. C., Weidemann A. D., Wells W. H. and Zaneveld J.R.V., 1995. A comparison of methods for the measurement of the absorption coefficient in natural waters. *J. Geophys. Res.*, **100**(C7): 13,201-13,220.

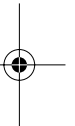
Petzold T. J., 1972. Volume scattering functions for selected ocean waters. *SIO Ref. 72-78, Scripps Inst. Oceanogr., La Jolla*, 79 pp. Condensed as Chapter 12 in *Light in the Sea*, Edited by J. E. Tyler, Dowden, Hutchinson & Ross, Stroudsburg, 1977, pp. 150-174.

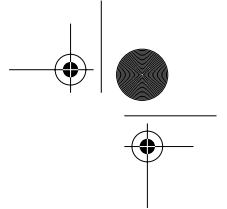
Pope R. M. and Fry E. S., 1997. Absorption spectrum (380-700 nm) of pure water. II. Integrating cavity measurements. *Appl. Opt.*, **36**(33): 8710-8723.





- Porter W. M. and Enmark H. T., 1987. A system overview of the Airborne Visible/Infrared Imaging Spectrometer (AVIRIS). In *Imaging Spectrometry II* (G. Vane, Ed.), *Society of Photo-Optical Instrumentation Engineers*, **834**: 22-31.
- Press W. H., Teukolsky S. A., Vetterling W. T., Flannery B. P., 1988. Numerical Recipes in C. *Cambridge University Press, Cambridge*, 994 pp.
- Proy C., Tanré D., and Deschamps P. Y., 1989. Evaluation of Topographic Effects in Remotely Sensed Data. *Remote Sens. Environ.*, **30**: 21-32.
- Quan X. and Fry E. S., 1995. Empirical equation for the index of refraction of seawater. *Appl. Opt.*, **34**(18): 3477-3480.
- Richards J. A., 1993. Remote Sensing digital image analysis. *Springer Verlag, New York*, 2nd edition, 340 pp.
- Richter R., 1990. A fast atmospheric correction algorithm to Landsat TM images. *Int. J. Remote Sensing*, **11**(1): 159-166.
- Richter R., 1996. Atmospheric correction of DAIS hyperspectral image data. *Computers & Geosciences*, **22**(7): 785-793.
- Richter R., 1999. Atmospheric/Topographic correction for wide FOV airborne imagery: model ATCOR 4, Version 2.0, DLR Report DLR-IB 552-05/99, German Aerospace Center, Institute for Optoelectronics.
- Roesler C. S., Perry M. J., and Carder K. L., 1989. Modelling in situ phytoplankton absorption spectra from total absorption spectra in productive inland marine waters. *Limnol. Ocean.*, **34**(8): 1510-1523.
- Sathyendranath S., Prieur L, and Morel A., 1989. A three-component model of ocean colour and its application to remote sensing of phytoplankton pigments in coastal waters. *Int. J. Remote Sensing*, **10**(8): 1373-1394.
- Schaepman M., Keller P., Schläpfer D., Cathomen C., and Itten K.I., 1997. Experimental Determination of adjacency effects over an eutrophic lake using a helicopter mounted spectroradiometer for the correction of imaging spectrometer data. *Proceedings of the Third International Airborne Remote Sensing Conference and Exhibition*, **1997**: II-497-II-504.
- Schaepman M. E., 1998. Calibration of a field spectroradiometer. Remote Sensing Series, Vol. 31. *PhD Thesis University of Zürich*, 145 pp.
- Schiller H. and Doerffer R., 1999. Neural network for emulation of an inverse model - operational derivation of Case II water properties form MERIS data. *Int. J. Remote Sensing*, **20**(9): 1735-1746.





Schläpfer D., 1998. Differential absorption methodology for imaging spectroscopy of atmospheric water vapor. Remote Sensing Series, Vol. 32. *PhD Thesis University of Zürich*, 131 pp.

Schowengerdt R. A., 1997. Remote Sensing. Models and methods for image processing. *Academic Press, 2nd Ed.*, 522 pp.

Smith R. C., 1969. An underwater spectral irradiance collector. *J. of Marine Res.*, **27**(3): 341-351.

Smith R. C and Baker K. S., 1984. Analysis of ocean optical data. *Proceedings of the Ocean Optics VII Conference, M. Blizard, Ed., SPIE*, **478**: 119-126.

Sturm B., 1993. CZCS processing algorithms. In *Ocean colour: theory and applications in a decade of CZCS experience. Netherlands: ESA Publ.*, pp. 95-116.

Tanré D., Deschamps P. Y., Duhaut P., and Herman M., 1987. Adjacency effect produced by the atmospheric scattering in Thematic Mapper data. *J. Geophys. Res.*, **92**(D10): 12000-12006.

Vasilkov A. P., 1997. A retrieval of coastal water constituent concentration by least-squares inversion of a radiance model. *Proceedings of the Fourth International Conference on Remote Sensing for Marine and Coastal Environments, Orlando, Florida, 17-19 March, 1997*, pp. II-107-III115.

van de Hulst H. C., 1957. Light scattering by small particles. *John Wiley*, 470 pp.

van den Hoek C., Jahns H. M., and Mann D. G., 1993. Algen. *Thieme*, 3rd edition, 411 pp.

Van der Piepen H., 1995. Nutzung und Anwendung des abbildenden Spektrometers ROSIS. *DLR-Nachrichten*, **77**: 11-14.

Vermote E., Tanré D., Deuzé J. L., Herman M., and Morcette J. J., 1994. Second simulation of the satellite signal in the solar spectrum. *6S User Guide, NASA-Goddard Space Flight Center, Greenbelt (MD)*, 182 pp.

Walker R. E., 1994. Marine light field statistics. *John Wiley*, 675 pp.

Westlake D. F., 1965. Some problems in the measurement of radiation under water: A review. *Photochemistry and Photobiology*, **4**: 849-868.

Wüest A., Wehrli B., and Imboden D., 1994. Grundlagen für die Sanierung des Zugersees, Untersuchungen des Stoffhaushaltes von Tiefenwasser und Sediment. *EAWAG-Auftrag 37-4840*, pp. 103.

